UNIVERSITY OF CALIFORNIA,
IRVINE

Nanoparticle Growth Studies on Highly Oriented Pyrolytic Graphite (HOPG) And Photocatalytic studies on bimetallic system supported on HOPG

DISSERTATION

submitted in partial satisfaction of the requirements
for the degree of

DOCTOR OF PHILOSOPHY

in Physical Chemistry

by

Jayde Yonjoo Kwon

Dissertation Committee:
Professor John C. Hemminger, Chair
Professor Reginald M. Penner
Assistant Professor Matthew D. Law

2014

DEDICATION

To

my dear parents and my only brother,

Soon-to-be my husband, and my new family

and all of my dearest friends.

Without their endless support and encouragement,

I could not have done this.

I would like to also express my sincere appreciation to

Professor John C. Hemminger

for his support and teachings.

TABLE OF CONTENTS

Page

LIST OF FIGURES

ACKNOWLEDGMENTS

I would like to express my sincere appreciation to many people who have contributed to the work presented in this dissertation. I would like to thank my Ph.D. thesis advisor Professor John C. Hemminger. Without his support, guidance, patience, ideas, and trust, this study would never have matured. Appreciation is extended to Professor Matthew D. Law for his guidance and contribution to pyrite nanoparticle growth. He has taught me how to think and write like a scientist. Appreciation is also extended to Professor Reginald M. Penner, who has been my committee member since my qualification exam. Without his encouragement I would have not continued my Ph.D. career.

I would like to thank Dr. James Taing who trained me on the evaporator which is the foundation of my thesis work. Dr. Nicholas Berry helped me on using his chemical vapor deposition chamber for my pyrite growth studies. Dr. Alexandria M. Margarella for teaching me on XPS and be a sincere friend. I would like to thank Dr. Jian-Guo Zheng for SEM and TEM training. He was always there for me when I needed help. Without his magic hand I would not have gotten those beautiful TEM images.

I would like to thank my past and present Hemminger group members: Safa Khan, Dr. Nicole Barrentine, Dr. Alexandria M. Margarella, Dr. Guofeng Sun, Dr. Theresa McIntire, Dr. Yu Liu, Dr. Marijke Van Spyk, Dr. Kathryn A. Perrine, Dr. Ming Cheng, Dr. Tanza Lewis, Paolo Reyes, Michael Makowski, Anthony Babore, Joel M. Langford, Fabian Rosner.

Special thanks to my dearest friend Safa Khan and Wenbo Yan. I still remember how we first met - something clicked us to bond so fast and strong. Your continuous encouragements and friendship allowed me to succeed in this graduate career. Although we are physically far apart from each other now, I know our friendship will last forever.

My deepest expression of appreciation goes to my parents and my only brother Danny. Words cannot describe how thankful and grateful I am to be their child and his sister. Without their support, encouragement, love, sacrifice, believing-in-me, and prayer, I could have not come this far. I also appreciate my grandparents for their spiritual support. I really appreciate their continuous love and prayer for me.

Last but not least, my sincere appreciation goes to my soon-to-be husband, Solomon. His love, support, motivational talks, editing this thesis, made everything possible. And I am looking forward to our endless days together.

CURRICULUM VITAE

Jayde Yonjoo Kwon

EDUCATION

University of California, Irvine, Irvine, California *Dec 2014*
Ph.D in Chemistry

University of California, Irvine, Irvine, California *Dec 2009*
M.S in Chemistry

University of Hawaii at Manoa, Honolulu, Hawaii *May 2008*
B.S in Chemistry
B.A in French
Minor in Korean

PUBLICATIONS

- Kwon, J. Y.; Berry, N.; Law, M.; Hemminger, J. Seed-mediated growth of pyrite structures, *in preparation.*
- Kwon, J. Y.; Hemminger, J.C. Photocatalytic properties of transition metals nanoparticles on linearly ordered Fe_2O_3 nanoparticle arrays, *in preparation.*
- Seefeld, S.; Limpinsel, M.; Liu, Y.; Farhi, N.; Weber, A.; Zhang, Y.; Berry, N.; Kwon, Y.; Perkins, C.; Hemminger, J.; Wu, R.; Law, M. Iron Pyrite Thin Films Synthesized from an Fe(acac)3 Ink *J. Am. Chem. Soc.* **2013**, *135*, 4412-4424.

ORAL PRESENTATIONS

- "Photocatalytic Properties of Photodeposited Pt Nanoparticles on Fe_2O_3 Nanoparticles Supported on Highly Oriented Pyrolytic Graphite (HOPG)" Jayde Yonjoo Kwon, John C. Hemminger. American Vacuum Society in Baltimore, MD. November 11, 2014
- "Growth of Iron Pyrite on Surface Treated Highly Oriented Pyrolytic Graphite (HOPG)" Yon Joo Kwon and John C. Hemminger. Southern California Society for Microscopy & Microanalysis Symposium in Irvine, CA. February 8, 2014. (Best Platform talk)
- "Nucleation growth of pyrite nanocrystal arrays by chemical vapor deposition on highly oriented pyrolytic graphite (HOPG)" Yon Joo Kwon, Nicholas Berry, Matt Law and John C. Hemminger. American Chemical Society in New Orleans, LA. April 7, 2013

- "Seed-mediated growth of 1D pyrite (FeS_2) Structures" Yon Joo Kwon, Nicholas Berry, Matt Law, and John C. Hemminger. 59th American Vacuum Society Conference in Tampa, FL. October 31, 2012

- "Fabrication of linearly-ordered pyrite (FeS_2) nano-arrays by sulfurization of vapor deposited iron oxide nanoparticles on highly oriented pyrolytic graphite (HOPG)" Yon Joo Kwon and John C. Hemminger. US-Korea Conference in Anaheim, CA. August 9, 2012.

POSTER PRESENTATIONS

- "Nucleated growth of Iron pyrite on highly oriented pyrolytic graphite by chemical vapor deposition" Jayde Yonjoo Kwon, Nicholas Berry, Matt Law, John C. Hemminger, Microscopy & Microanalysis, Hartford, CT. August 7, 2014

- "Nucleation growth of pyrite nanocrystal arrays by chemical vapor deposition on highly oriented pyrolytic graphite (HOPG)" Yon Joo Kwon, Nicholas Berry, Matt Law and John C. Hemminger. American Chemical Society in New Orleans, LA. April 8, 2013

- "Seed-mediated growth of 1D pyrite (FeS_2) Structures" Yon Joo Kwon, Nicholas Berry, Matt Law, and John C. Hemminger. Southern California Chapter of American Vacuum Society at UCLA, CA. October 3, 2012

AWARDS

- Best platform talk at Southern California Society for Microscopy & Microanalysis Symposium (Travel Award), Feb 8, 2014 for "Growth of Iron Pyrite on Surface Treated Highly Oriented Pyrolytic Graphite (HOPG)"

PROFESSIONAL MEMBERSHIPS

The American Chemistry Society	2012-present
American Vacuum Society	2010-present
Microscopy Society of America	2014-present

ABSTRACT OF THE DISSERTATION

Nanoparticle Growth Studies on Highly Oriented Pyrolytic Graphite (HOPG)
And
Photocatalytic studies on bimetallic system supported on HOPG

By

Jayde Yonjoo Kwon

Doctor of Philosophy in Physical Chemistry

University of California, Irvine, 2014

Professor John C. Hemminger, Chair

Nanoparticle (NP) growth mechanisms have received attention due to the many potential applications such as biomedicine, catalysts, fuel cell, and solar cells. Here in this dissertation, I focus on developing a new tool to study the fundamental growth mechanisms of NP growth. This system relies on the use of highly oriented pyrolytic graphite (HOPG) as a substrate for deposition of metal NPs.

HOPG is layers of graphene stacked in a parallel arrangement. It is a useful substrate to study the growth of metal NPs due to its inert nature of surface. This system provides many advantages of fundamental studies of metal NP growth (discussed in chapter 1 introduction) the most critical point, for the purpose of this dissertation, being the separation of NP growth mechanism from substrate effects.

In the subsequent chapters, I focus on three major studies: 1) fabrication of linearly ordered Fe NP growth along the step edges of HOPG to study fundamental mechanisms of seed-mediated growth of pyrite, 2) photocatalytic properties of a bimetallic system composed of

photodeposited Pt onto the fabricated Fe NP arrays, and 3) the improvement of the detection limit of this Fe NP system to better theoretical research on NP growth.

The first three chapters focus on the studies of NP growth on HOPG. Chapter 1 shows the successful and selective deposition of linearly ordered Fe NPs on the step edges of HOPG. Using these Fe NP arrays, the study of using different precursors to convert Fe oxide to FeS_2 (pyrite) is discussed in chapter 2. Despite the interest in pyrite due to its promising properties for solar cell applications, pyrite devices suffer from low efficiency. This is partly due to a lack of understanding of which parameters are required for preferential growth of a pure pyrite phase. Therefore, using the Fe NP system on HOPG provides a toolkit for studying the fundamental properties of particle growth at very early stages. Seed-mediated growth of pyrite NPs by atmospheric-pressure chemical vapor deposition in the context of different precursors is discussed in chapter 3. The results are promising yet many discussions can be raised as to using my system to improve pure pyrite phase growth in the future.

In chapter 4, I focus on generating a bimetallic system using the Fe NPs on HOPG to study photocatalytic properties. Photodeposition of Pt NPs on Fe oxide NP arrays is demonstrated for the first time. I show that generation of this Pt-Fe oxide bimetallic system actually improves the photocatalytic activity as assessed by methylene blue degradation studies under UV exposure.

Lastly, in chapter 5, an attempt was made to improve the HOPG NP system to improve the surface characterization detection limit. This was done by studying Fe NP growth on oxygen plasma treated modified surfaces of HOPG. The plasma treatment creates more defect sites on the surface of HOPG leading to higher-density deposition of Fe oxide NPs that significantly improves the low detection limit of the original HOPG NP system.

CHAPTER 1

Fabrication of Linearly Ordered Iron (Fe) Oxide Nanoparticle Arrays on Highly Oriented Pyrolytic Graphite (HOPG) Substrate

INTRODUCTION

Highly oriented pyrolytic graphite (HOPG) is layers of graphene – two dimensional and single-atom thick form of carbon – stacked in a parallel arrangement. It is a useful substrate to study the growth of metal nanoparticles (NPs) due to its inert nature of surface, conductivity, abundance, relative non-toxicity.[1,2,3] HOPG is composed of a basal plane with strong covalent carbon-carbon bonds where the interlayer forces are relatively weak.[4] Carbon atoms within a layer interact much stronger than adjacent planes in that each layer can be manually cleaved by an adhesive tape. Due to this characteristic, the interaction between metal deposits and the HOPG terrace is relatively weak. In addition, the strong covalent carbon-carbon bonds on the plane make the diffusion mobility of deposited metals high at the HOPG terrace. On a freshly cleaved HOPG surface, micron-sized flat terraces are found along with some defect sites. There are two types of defect sites: step edges due to a stacking fault and small localized defects due to atom vacancies at the surface. It has been shown that metals have a stronger interaction with HOPG at the step edges allowing metal adatoms to nucleate and create linearly ordered metal NP arrays.[5]

Graphite exists in many different grades and sources. X-ray and neutron optics were used to judge the grade of HOPG by examining their mosaic spread. ZYA, ZYB and ZYH are the grades of HOPG where its mosaic spread is (0.4° ± 0.1°), (0.8° ± 0.2°), and (3.5° ± 1.5°), respectively. The grain sizes of these grades are 10 μm, 1μm, and 30-40 nm, respectively. In

this particular experiment, we are using ZYB grade of HOPG because its mosaic spread gives sufficient number of step edges.

Using HOPG as a substrate to study the growth of metal NPs has three advantages. First, the inert properties of HOPG results in approximately no background oxygen signal on clean HOPG surface by X-ray photoelectron spectroscopy (XPS) and other surface analysis techniques. Second, charging effect is diminished due to the metallic properties of HOPG. Third, deposited metal NPs can be organized in a linear fashion on the naturally occurring step edges. Ordered metal NPs are crucial and useful because it can facilitate theoretical calculations. This makes HOPG an ideal substrate to study the basic growth mechanism of a variety of metals independent from substrate effects.

Step-edge decoration of HOPG with metal nano-clusters has been reported using several different metals, including Ti,[5] Au,[6] Ag,[7,8,9] Co,[10] and Ni.[11] Here we show the specific generation of well-separated Fe oxide NPs on HOPG step edges that provide the basis for further fundamental studies of other metal growth at the single nanocrystal level, presented in subsequent chapters.

EXPERIMENTAL

Highly Oriented Pyrolytic Graphite (HOPG). 12 mm × 12 mm × 2 mm pieces of HOPG with a mosaic spread of 0.8 ° ± 0.2 ° (Grade ZYB, Momentive Performance) were used. Surface of HOPG was cleaved using Scotch tape in air to expose fresh surface and immediately transferred to vacuum evaporator chamber.

Physical Vapor Deposition. Physical Vapor Deposition (PVD) in an Edwards 306A thermal evaporation coating was used to fabricate linearly ordered iron oxide nanoparticle arrays on HOPG. The sample was placed in a tungsten holder that is place at an angle of ~ 50 ° from the ceramic crucible holding iron shots (Alfa Aesar). Prior to metal deposition, HOPG was annealed at above 500 °C with base pressure below $5 \times 10^{-6-}$ torr for 3 hours to desorb water and remove any organic residues on the surface. The ceramic crucible holding iron shots were resistively heated at ~12 amps. Deposition thickness was measured by a quartz crystal microbalance, INFICON front load single crystal sensor. The sample was annealed for 3 hours after deposition.

Characterization. Scanning Electron Microscopy (SEM) of FEI Quanta 3D FEG and FEI Magellan 400 XHR at 10 kV were used to image each samples after iron oxide deposition. EDS (Oxford Instruments) analysis was done by using a silicon drift detector at an accelerating voltage of 15 kV. Transmitted Electron Microscope (FEI/Phillips CM-20) was used. TEM samples were prepared by cleaving sample surface with an adhesive tape. Only optically transparent areas were mounted on a carbon-free copper TEM grid. X-ray Photoelectron Spectroscopy (XPS) measurements were performed with Molecular Environmental Sciences Beamline (Beamline 11.0.2) at the Advanced Light Source synchrotron facility at Lawrence Berkeley National Laboratory. X-rays were produced from the ALS storage ring by a bending magnet. The hemispherical analyzer uses a three stage differentially pumped electrostatic lens

system to maintain the UHV environment. The sample was mounted on a sample holder that can be heated and measures accurate temperature by the thermocouple that is mounted on it. The spectra were obtained at a base pressure of 1×10^{-9} Torr. The pass energy of 100 eV and 20 eV were used for survey scans and narrow scans, respectively. Binding energy was calibrated by C1s of HOPG set at 284.6 eV as a reference. XPSPeak 4.1 and CasaXPS were used to deconvolute background. Adobe Photoshop was used to measure the iron oxide NP size and its spacing.

RESULTS AND DISCUSSION

1.1 Fabrication of Iron (Fe) oxide NPs on HOPG by varying substrate temperature upon deposition.

Due to the fact that HOPG sample preparation is performed in air and then transferred to the evaporator, an annealing process is required as a 'cleaning process' prior to Fe metal deposition. Métois *et al.* reported different surface cleaning procedures by thermal annealing.[12] Of interest, Appy *et al.* reported that annealing ZYH and ZYA grade of HOPG to 800 K for several tens of minutes in ultra-high vacuum (UHV) is sufficient enough to remove any impurities and absorbates on the surface of HOPG. Because our system is not in UHV, but rather at a base pressure of 5×10^{-7} Torr, longer annealing at higher temperature was used. Our pre-annealing condition was 3 hours at above 400 °C and post-annealing condition was 3 hours at deposition temperature. At this temperature, organic absorbates or water molecules were expected to be removed.

The naturally occurring step edges on a freshly cleaved HOPG allows individual adatoms to nucleate and form NPs at these step edges where the mobility of the metal adatoms depend on substrate temperature. Here we monitored Fe oxide NP nucleation at various substrate temperatures. Figure 1.1 shows a SEM image of a sample with a uniform thickness of 2 nm Fe deposited on HOPG that was held at 150 °C followed by 3 hours of post-annealing at the same temperature. This condition resulted in the deposition of Fe oxide NP all over the HOPG surface resembling a thin film. These particles were not crystalline in morphology. The low-magnification SEM image (Figure 1.1 top), shows some areas where particles form a line. This suggested that Fe adatoms that happened to deposit at the step edges nucleated along the step edges creating nanowire-like structures. The formation of these linear arrays is more likely due

to the randomness of Fe adatom deposition on the surface rather than its mobility. A high-magnification SEM image (Figure 1.1 bottom) shows a detailed morphology of the nano-clusters. These nucleated nano-clusters show a dendritic morphology with no discrete or crystalline structure likely due to a kinetic product caused by slow diffusion of Fe adatoms at this temperature. The dendritic-type shapes are not due to contamination but due to diffusion-limited growth, which is well understood in metal-on-metal growth systems.[3] Perhaps Fe adatoms were deposited at the edges of other adatoms but due to low mobility at a given temperature resulted in the creation of dendrites. This suggested that at elevated temperatures, growth of three-dimensional crystallites would be expected.

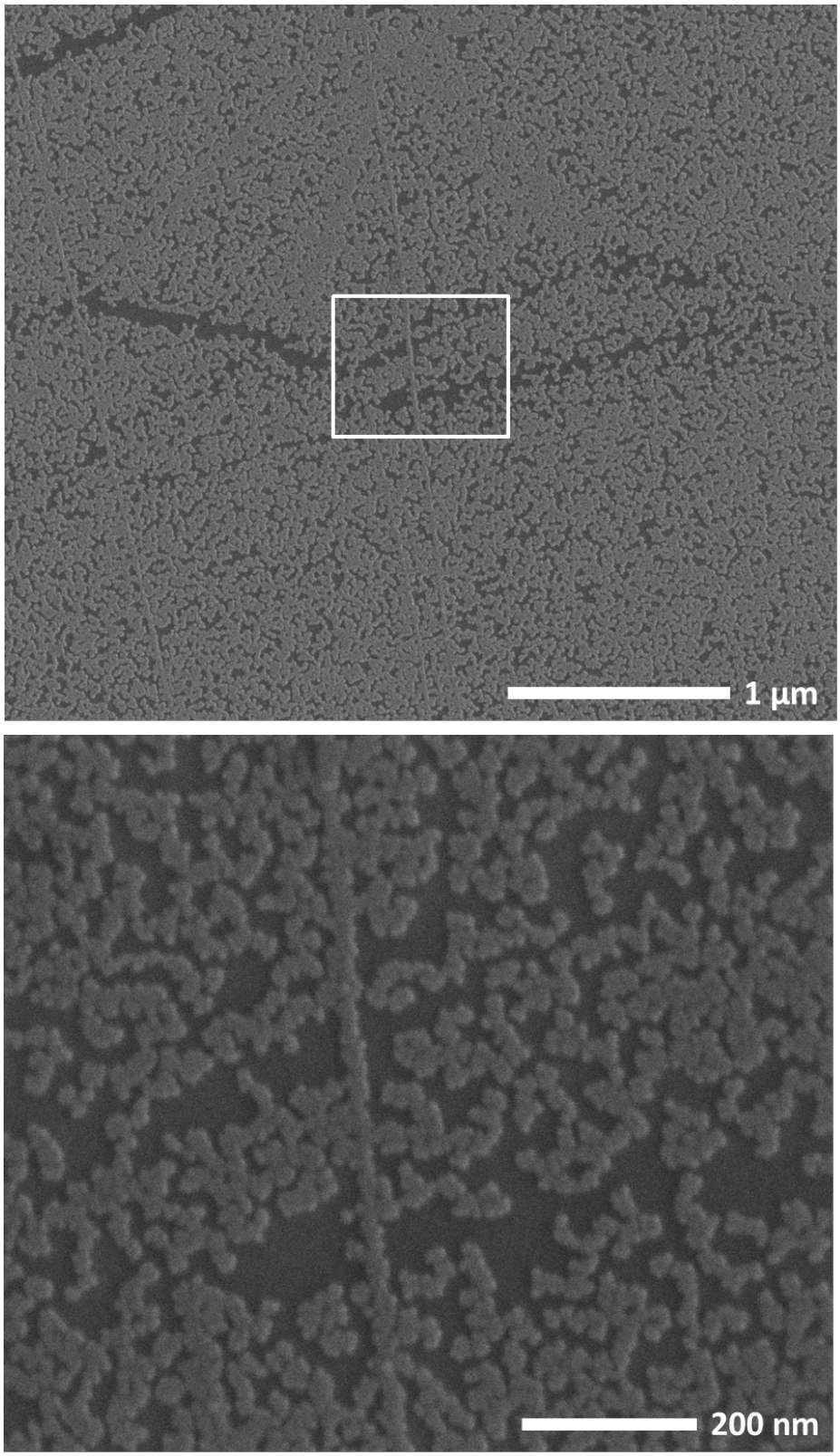

Figure 1.1. SEM images of Fe (uniform thickness of 2 nm measured by quartz microbalance) deposited when HOPG was held 150 °C (top) and a magnified region (bottom).

To our expectation, when HOPG substrate was held at 300 °C upon Fe deposition, different NP nucleation growth was observed (Figure 1.2). Unlike the dendritic growth shown in Figure 1.1, there was a preference towards nanowire formation. A low-magnification SEM image (Figure 1.2 top) shows that there were small NP deposited all over the HOPG terrace, similar to Figure 1.1; however, the distance between the clusters was fairly larger than that of Figure 1.1. Also, there was definitely more formation of step edge decorations. The step edge decorations are in random direction partly due to different planes of graphene sheets oriented in different directions after exfoliation by adhesive tape. Of interest, under these conditions, the step edge decorations are no longer in forms of connected nanowires. Rather, they appeared to be discrete NPs closely aligned along the step edges. A high-resolution image shows that these nucleated nano-clusters were more discrete and were in a spherical form (Figure 1.2 bottom). Although there was an increase in linearly ordered NP array formation at 300 °C, it was clear that at this temperature not all the Fe adatoms moved to the step edges before it nucleated.

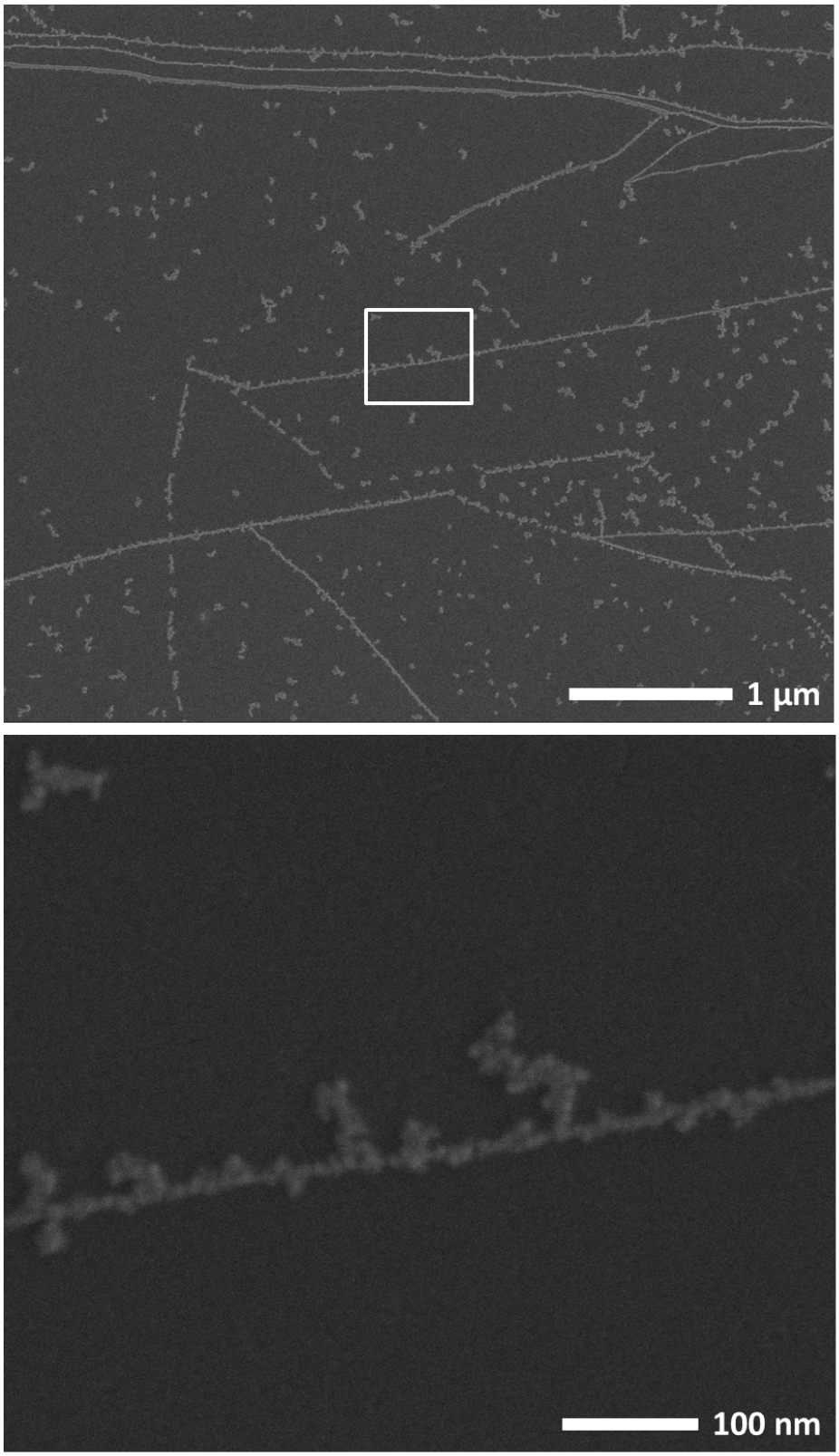

Figure 1.2. SEM image of Fe (uniform thickness of 2 nm measured by QCM) deposited when HOPG was held at 300 °C (top) and a magnified region (bottom).

When the substrate was heated to 400 °C upon Fe deposition, different morphological changes were observed (Figure 1.3). We observed nano-cluster assembly mostly along the step edges of the HOPG, yet significant dendrites of nano-clusters remain on the terraces. Similar results have been reported previously.[2, 13] In contrast to Figure 1.2, different particle morphology is seen in that all the NPs are more discrete and crystalline (Figure 1.3). A high-magnification SEM image (Figure 1.3 bottom), emphasizes this observation. Instead of nanowire-like formation along the step edges, discrete linearly ordered Fe oxide NP arrays are formed at the step edges. Interestingly, even NPs on the terraces are in spherical morphology. It is of note that although individually separated spherical Fe NPs are formed under this condition, the substrate temperature may not be high enough to move all the NPs only at the step edges.

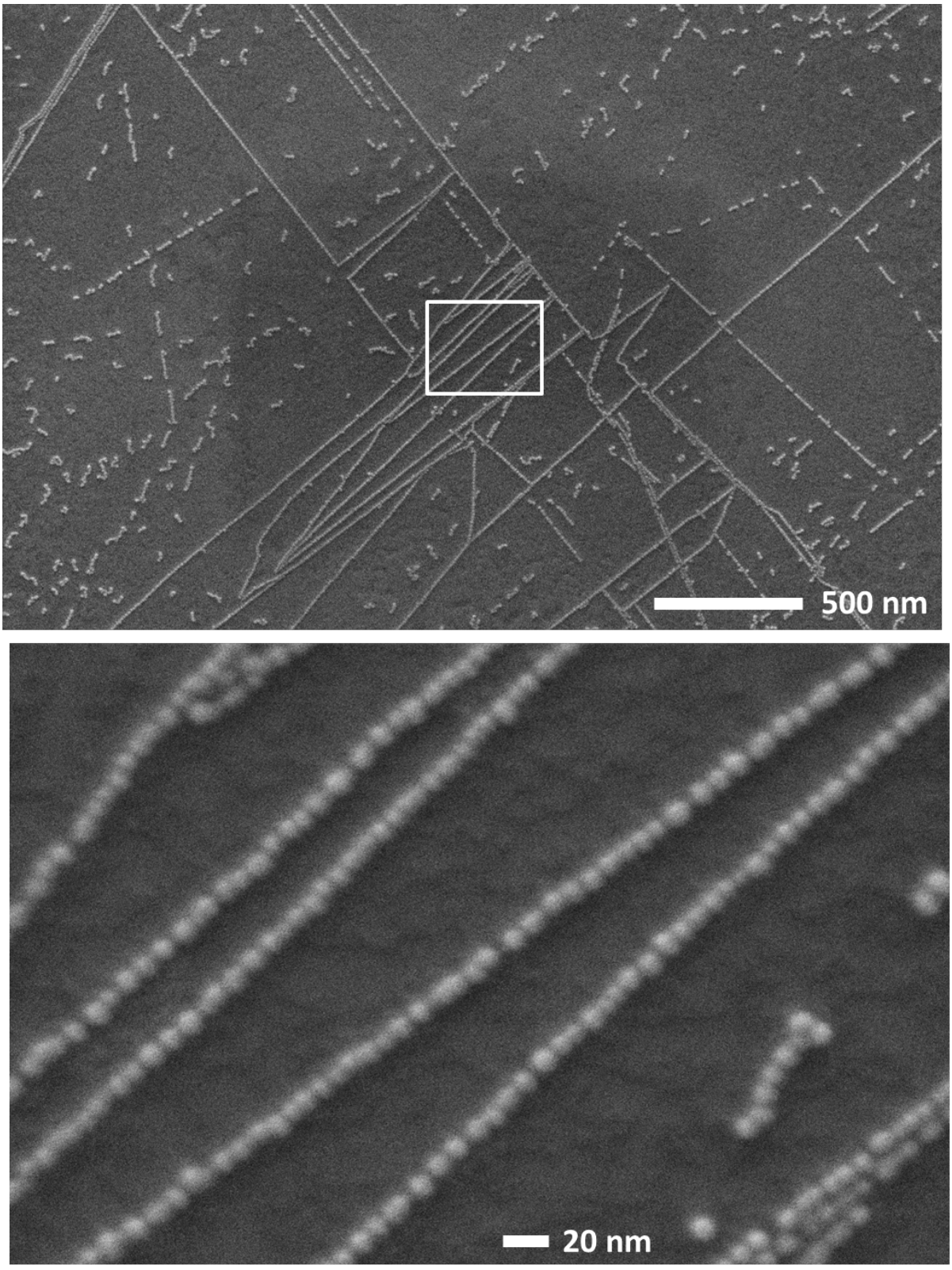

Figure 1.3. SEM image of Fe (uniform thickness of 2 nm measured by QCM) deposited when HOPG was held at 400 °C (top) and a magnified region (bottom).

When the substrate temperature upon deposition reaches above 475 °C, all the adatoms of Fe diffused into step edges and nucleate forming only linearly ordered Fe oxide NP arrays (Figure 1.4). A low-magnification SEM image (Figure 1.4 top) of a 20 μm × 20 μm window shows that there is no nucleation at terrace observed. A high-magnification SEM image (Figure 1.4 bottom), shows discrete spherical Fe oxide NPs decorated along the step edges. The step-edge decoration is due to the fast diffusion of metal atoms on the terrace and low binding energy. The growth of NPs is favored on HOPG because the adatom-adatom interaction is much stronger than the adatom-substrate interaction, resulting in Volmer-Weber growth of 3D islands.

We measured the gap between the NPs and their individual sizes shown in Figure 1.4 (Figure 1.5; Photoshop software was used). The average NP size was around 7-8 nm in diameter and we could see NPs as big as 18 nm. Most of the edge-to-edge spacing of the NPs was 1-2 nm where some NPs were 9 nm apart from each other. It is not known how to control the gaps of the NPs. However, it has been known that the size of the NPs can be varied by deposition amount.

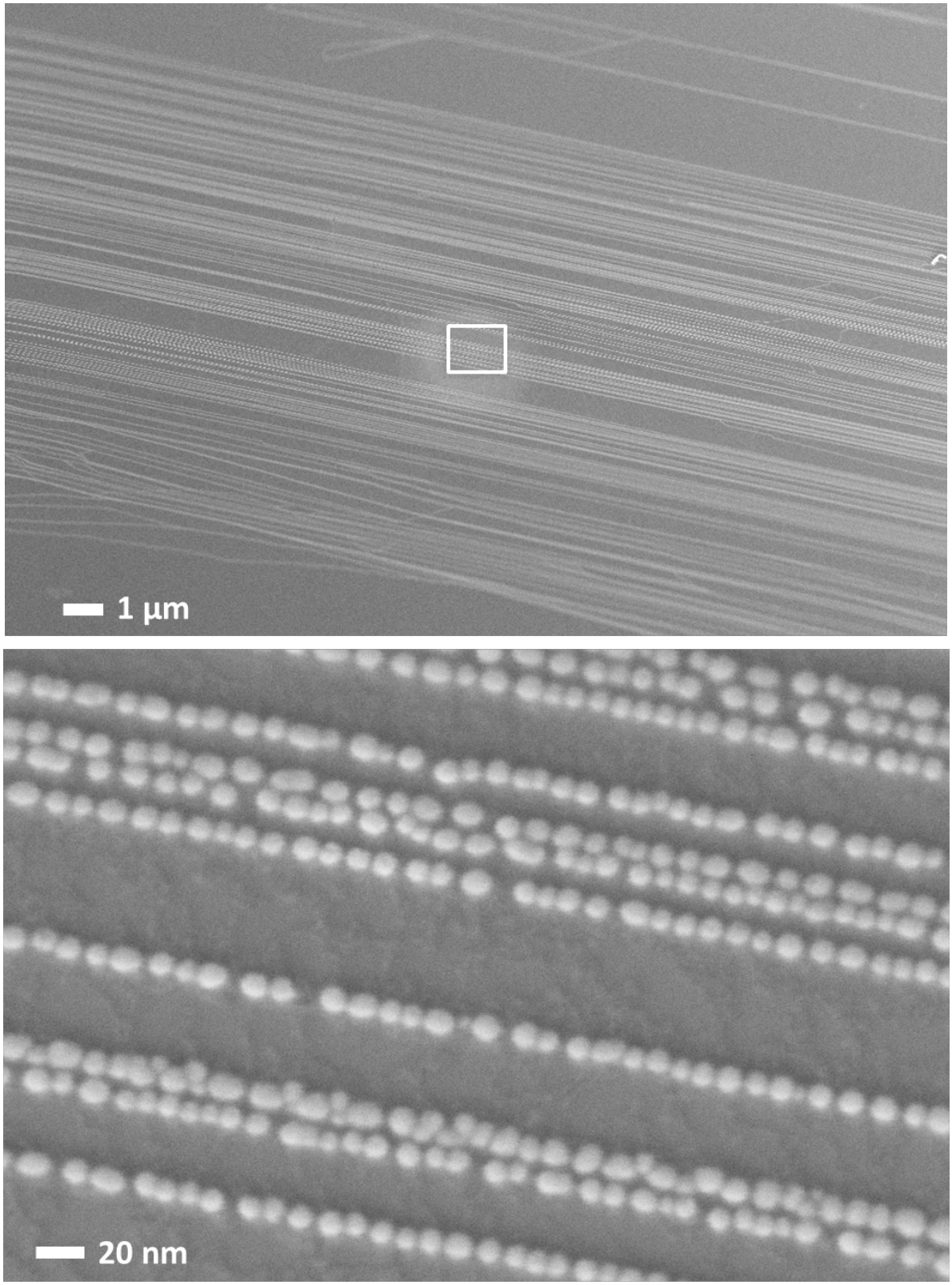

Figure 1.4. SEM image of Fe (uniform thickness of 2 nm measured by QCM) deposited when HOPG was held at above 475 °C (top) and a magnified region (bottom).

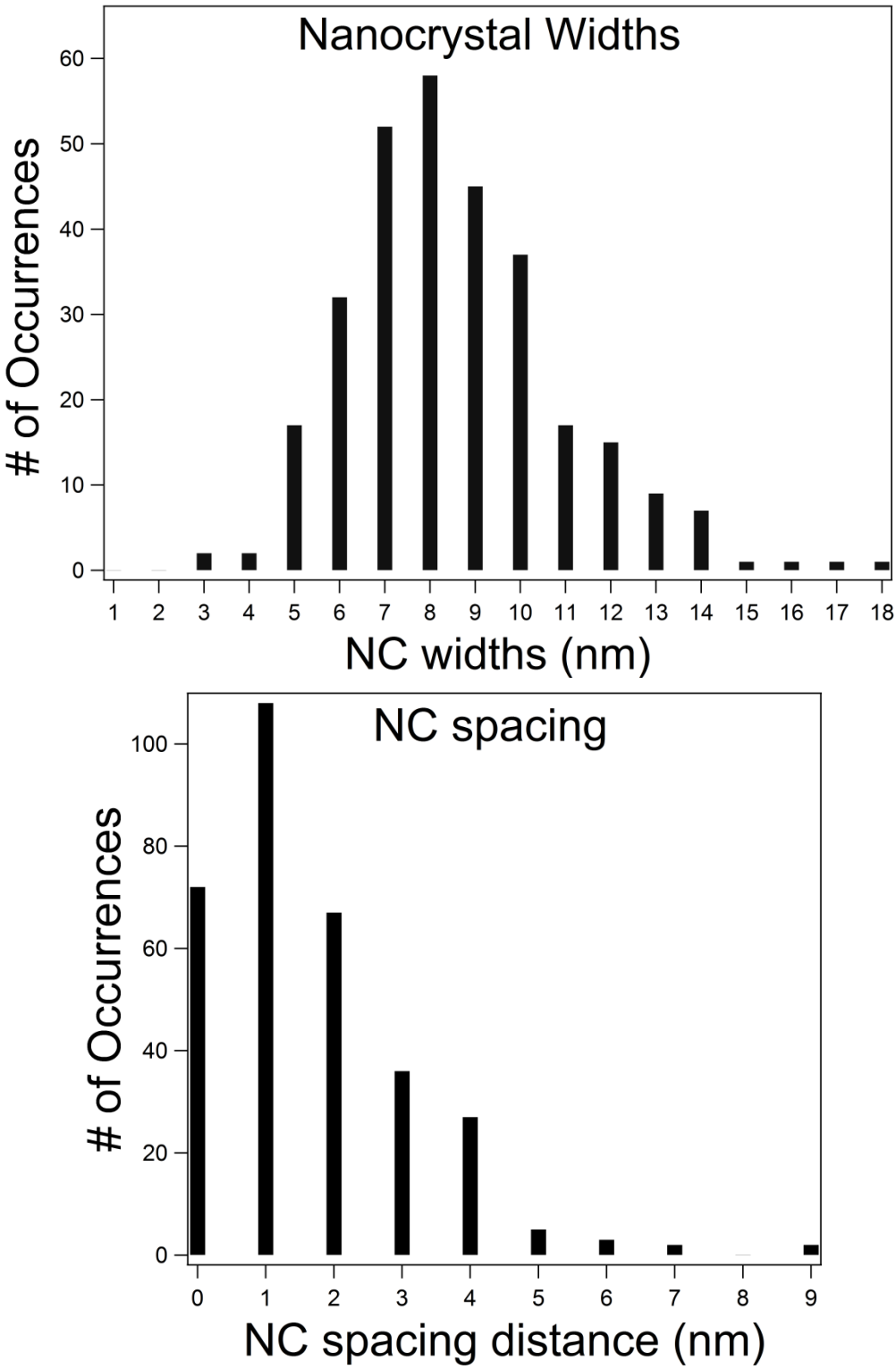

Figure 1.5. NP size distribution and NP spacing measurements from Figure 1.4 (bottom).

1.2 Fe nanoparticle size variation based on deposition amount

Figure 1.6 and Figure 1.7 represents two different samples with different amount of Fe deposited at above 475 °C. Figure 1.6 represents a SEM image of a sample where uniform thickness of 10 nm of Fe measured by Quartz microbalance was deposited. A low-magnification image (Figure 1.6 top), shows that with 10 nm deposition of Fe, there was no terrace decorations. All the particles were aligned along the step edges (similar to Figure 1.4). A High-magnification SEM image (Figure 1.6 bottom), shows size differences of the Fe oxide NPs to the 2 nm deposition of Fe sample (Compare to Figure 1.4 bottom). The average NP size was around 22 nm. When uniform thickness of 25 nm of Fe deposited onto HOPG that was held at 475 °C, particle decorations was different (Figure 1.7). Due to the increase in Fe deposition, particles not only decorated along the step edges but also started to decorate the HOPG terraces. The morphology of particles along the step edges was different as well. The gaps between the particles diminished with increase in Fe deposition amount. It could also be seen that smaller NPs in 5-20nm in size were deposited on top of larger nano-clusters. Due to loss of gaps between NPs, nanowire-like features were formed along the step edges. Fe particles could have nucleated on the terraces of HOPG due to the heavily occupied step edges with Fe. The NPs on the terraces were in 50-70nm in size and were crystalline in structure.

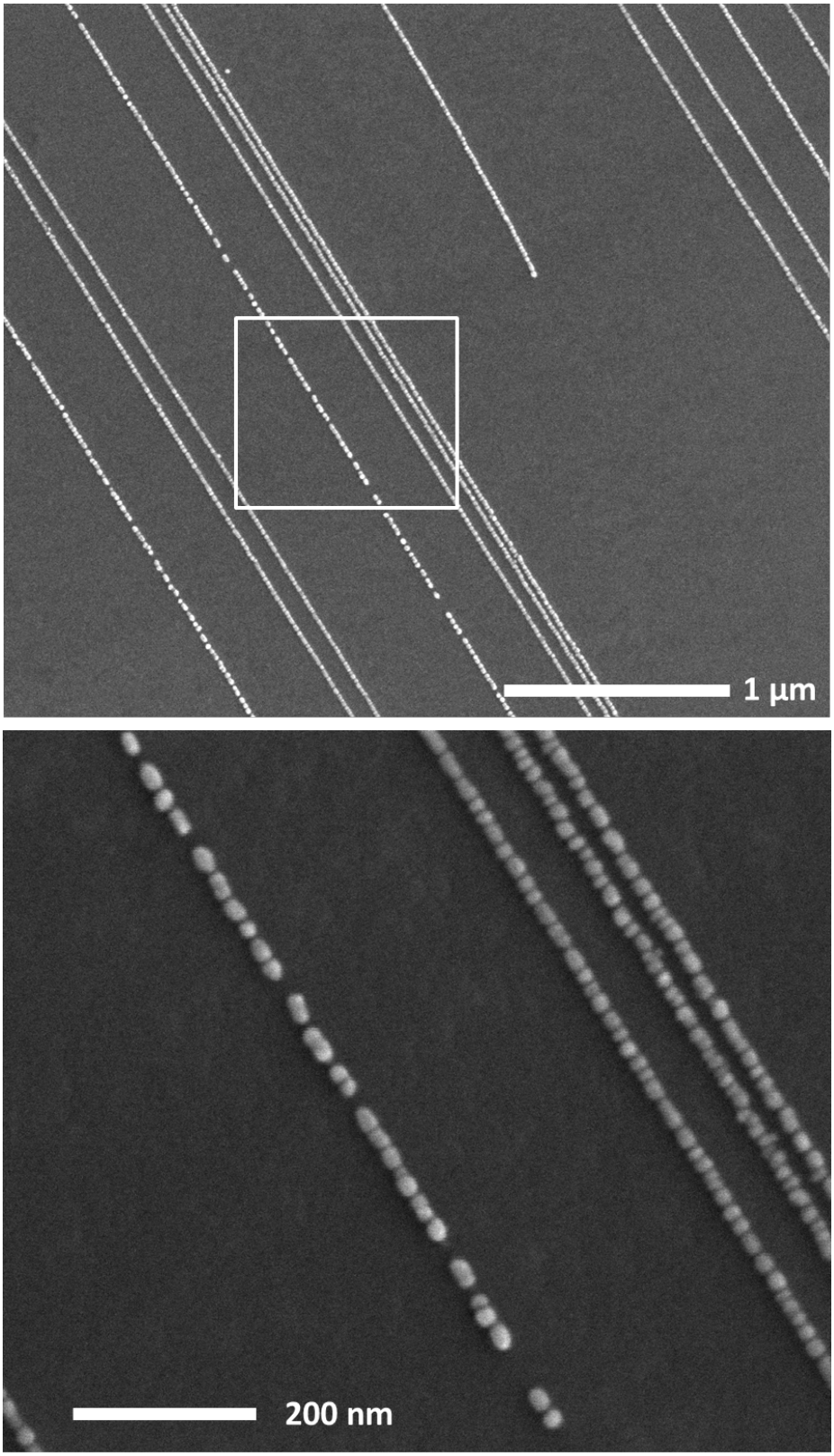

Figure 1.6. SEM image of Fe (uniform thickness of 10 nm measured by QCM) deposited when HOPG was held at above 475 °C (top) and a magnified region (bottom).

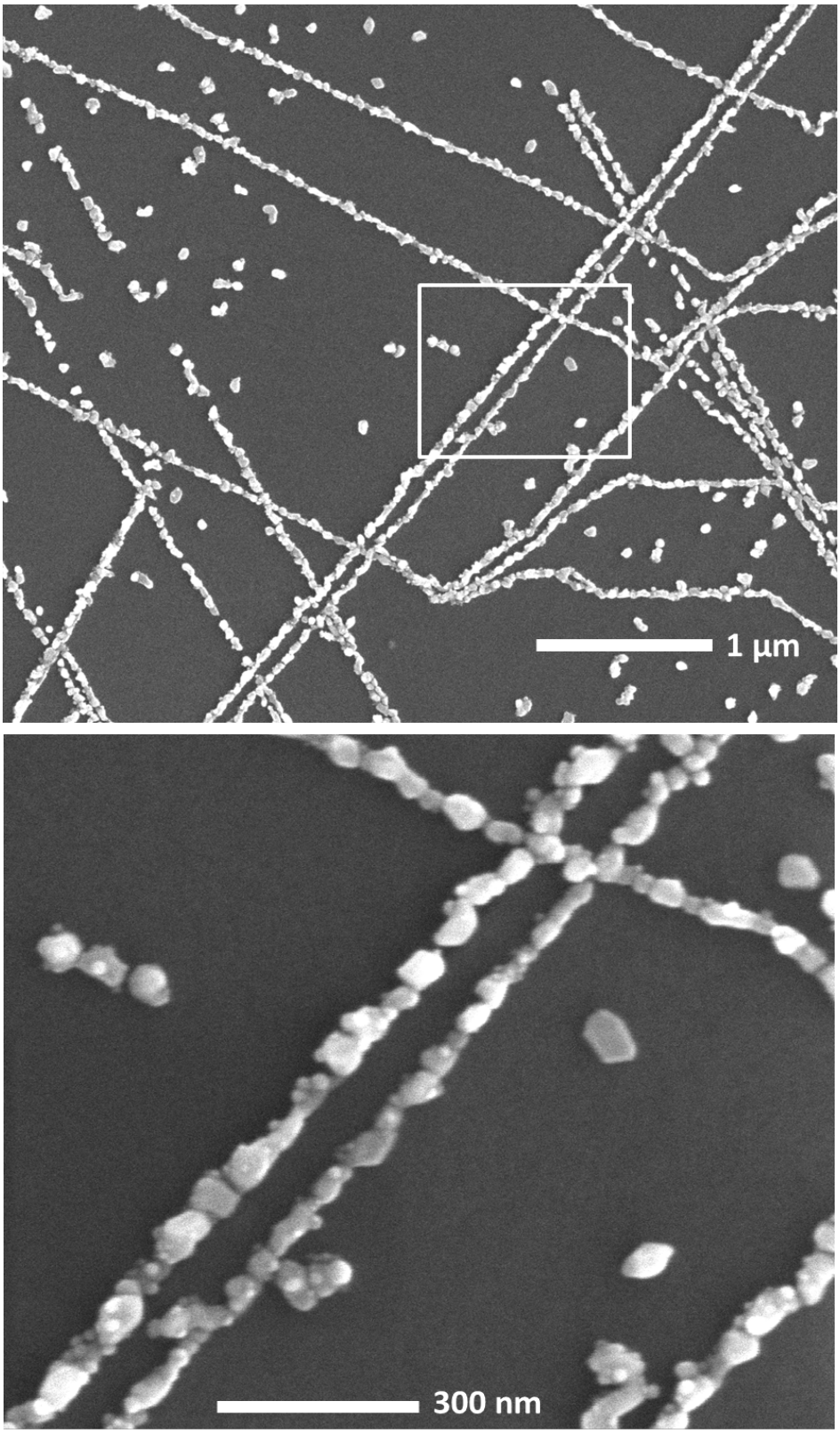

Figure 1.7. SEM image of Fe (uniform thickness of 25 nm measured by QCM) deposited when HOPG was held at above 475 °C (top) and a magnified region (bottom).

1.3 Characterization of Fe oxide nanoparticle arrays

We characterized the NPs by atomic force microscope (AFM), transmission electron microscopy (TEM) and X-ray photoelectron spectroscopy (XPS) to characterize their heights, microstructure, phase and elemental composition. A sample that was prepared the same way as in Figure 1.4 was used. AFM was used to determine the heights of these nanoparticle arrays. Figure 1.8 shows an AFM image with the red line representing where the heights were measured. The blue cursor at the bottom of the AFM image is the beginning of histogram of particle heights. The average heights for these NPs were in the range of 10 ± 2 nm.

For TEM studies, samples were prepared by dry transfer of exfoliated HOPG layer with an adhesive tape where the thin tethered area was placed in a carbon free 3 mm × 3 mm copper grid (100/50 mash). Figure 1.9 shows a representative TEM image. Similar to the SEM images (shown above), TEM images also show individually separated spherical Fe oxide NPs. A low-magnification image (Figure 1.9A), shows that the NPs are inhomogeneous in shape and size. Several NPs showed differing contrast where the small dark contrast region represented the presence of metallic Fe domains and the light contrast regions represented Fe oxide NPs. High-magnification TEM images shown in Figure 1.9B and C reveal that most of the NPs had well-developed lattice fringes. The lattice fringe spacing measured in Figure 1.9B corresponds to (220) orientation of Fe_3O_4.

XPS spectra were analyzed by using CasaXPS and XPSpeak4.1 software. All spectra were calibrated by fixing C 1s peak to 284.6 eV, which represents graphite. Background subtraction was made by subtraction of Shirley-type background from each spectrum.[14] All the survey scans were collected to determine the presence of contaminants. High-resolution Fe 2p spectrum was collected for the as-prepared sample (Figure 1.10A). The spectra suggested that

the Fe 2p spectrum is dominated by the oxide phase of Fe and at lower binding energy there is a small peak representing metallic Fe. In Figure 1.10B, the Fe 2p spectra shows three spin-orbit doublets. Fe^{2+} and Fe^{3+} components were fitted by asymmetric lineshapes that mimic the multiplet splitting effect. The fitted spectra with the binding energies of 709.16 eV, 711.6 eV, and 706.5 eV are characteristic of Fe^{2+}, Fe^{3+} and Fe^{0}, respectively.[15] There is also shake-up satellites in the higher binding energy to Fe $2p_{3/2}$ is characteristic of Fe^{3+}. The presence of metallic Fe species on the sample validates the TEM data (Figure 1.9). However, most of the NPs were in Fe oxide forms with the presence of core-shell type of Fe oxide-Fe as shown in Figure 1.9.

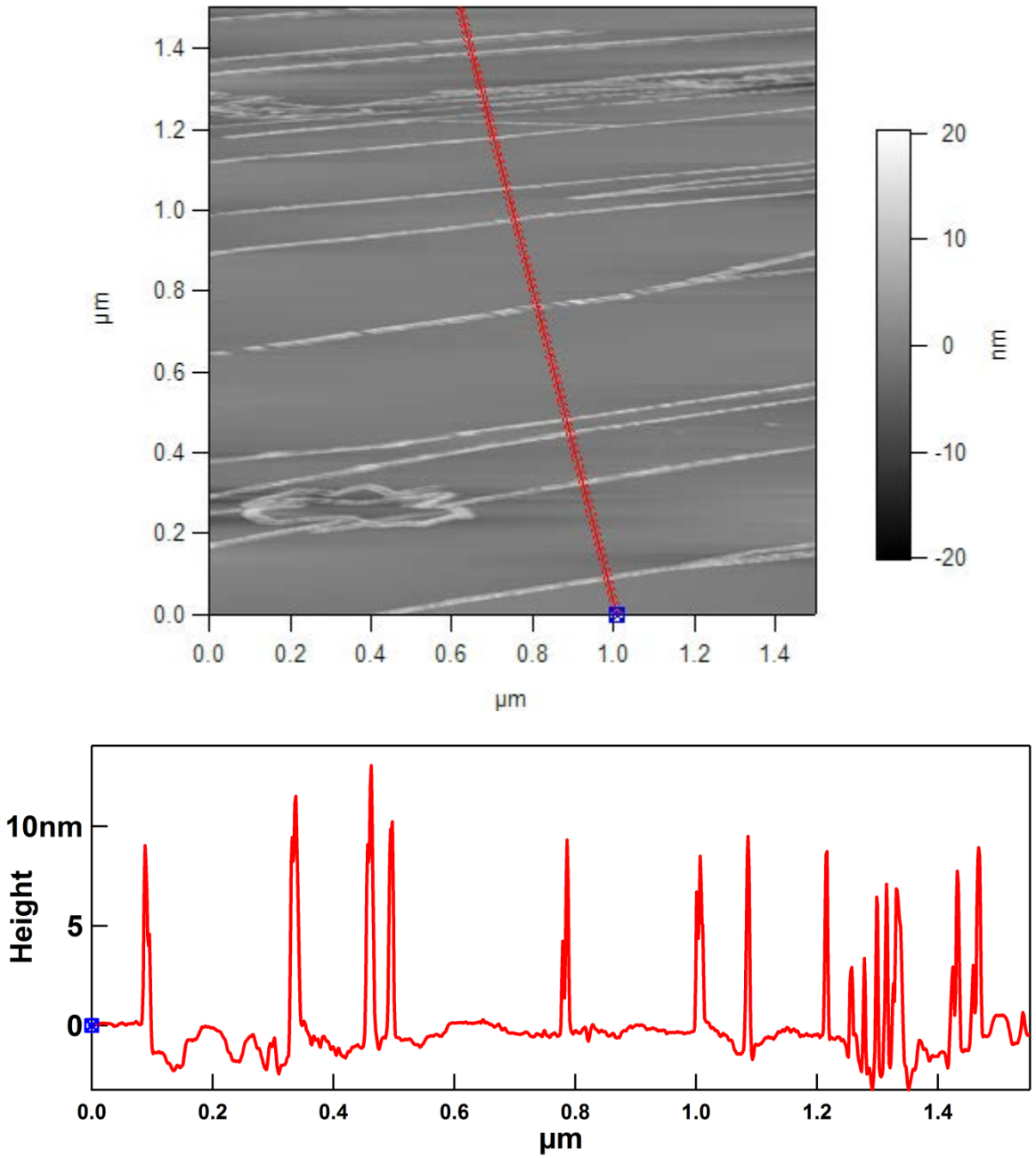

Figure 1.8. Atomic Force Microscope of 2 nm Fe oxide on HOPG and its height information.

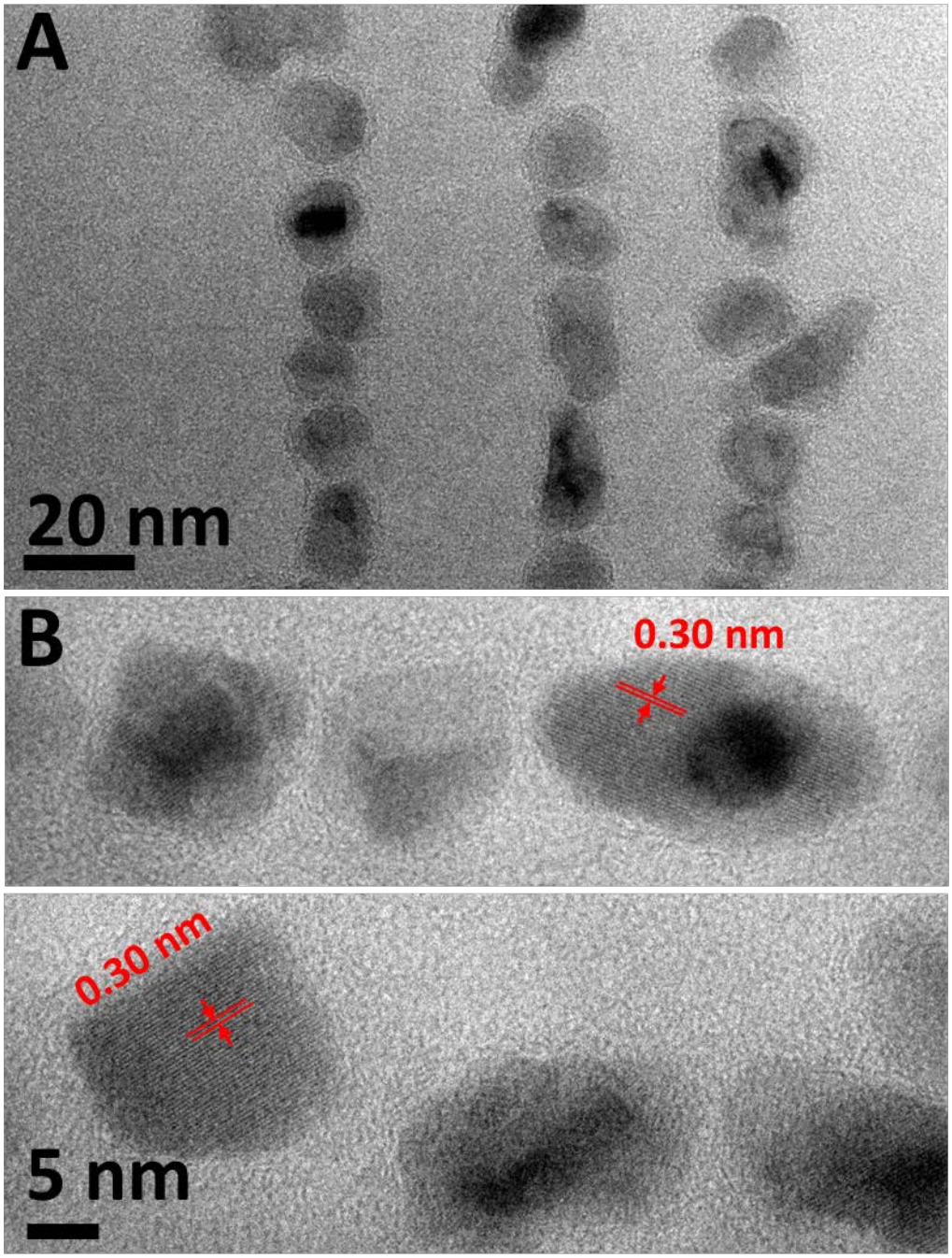

Figure 1.9. TEM and XPS characterization of NC chains prepared on HOPG at 475°C. (a) Low-magnification TEM image of segments of three NC chains. The NC size/shape is somewhat different from the data in Figure 1 and the SI because two different sample holders were used to heat the HOPG. (b) Lattice-resolved images of several NCs. The measured fringe spacing of 3.0 Å corresponds to Fe_3O_4 (220).

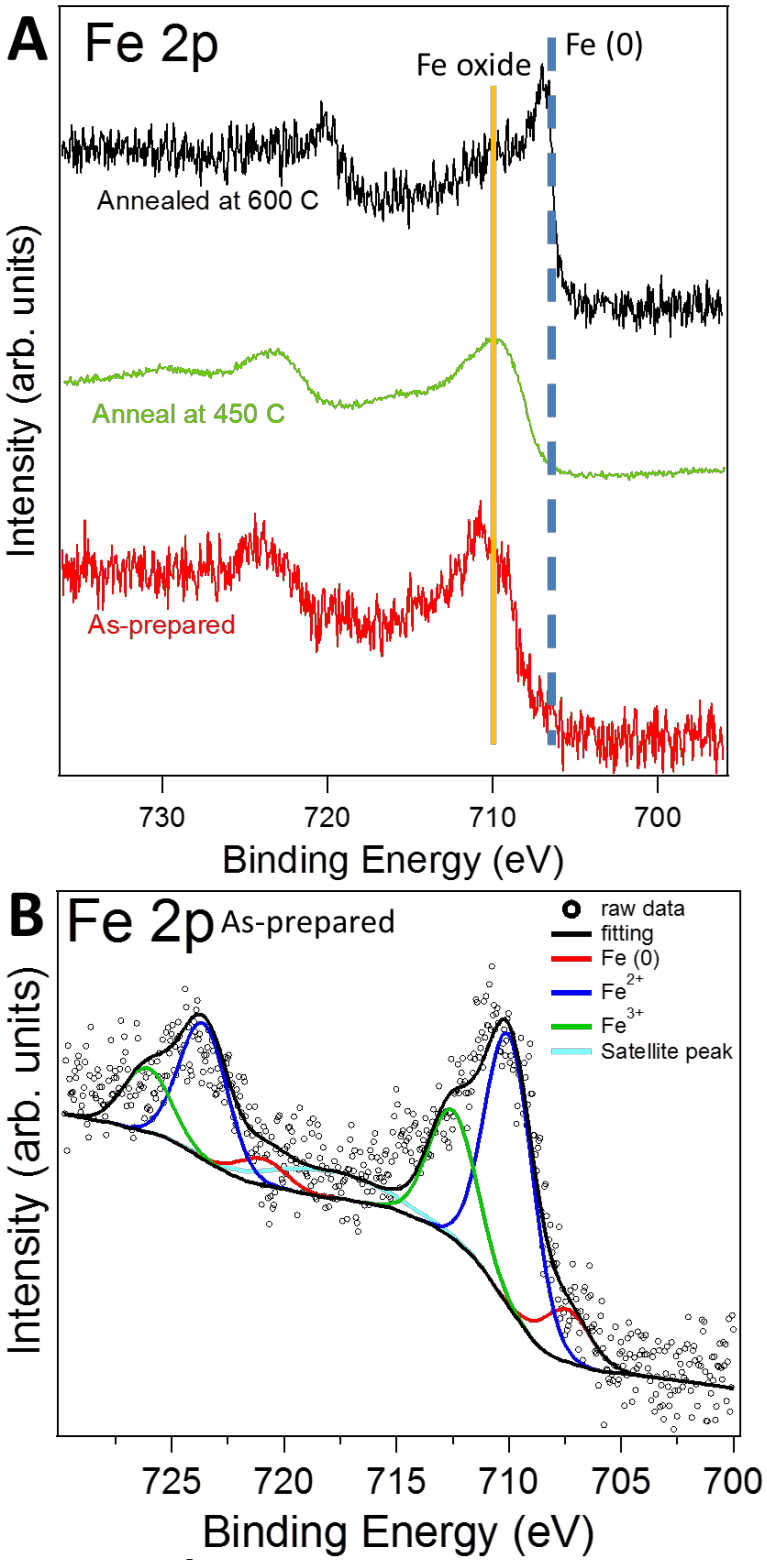

Figure 1.10. XPS Fe2p of a 3 mm^2 area of NC chains. (a) Fe 2p XP spectrum of as-prepared and annealed at 450 °C and 600 °C. (b) deconvoluted Fe 2p XP spectrum showing the presence of Fe(0), Fe(II), and Fe(III), consistent with a phase mixture of Fe_3O_4 and metallic Fe.

CONCLUSION

In this chapter, we have investigated Fe NP growth on HOPG by varying substrate temperature upon deposition. We have successfully found a condition where above 475 °C in temperature, all NPs could be specifically decorated along the step edges of HOPG suggesting that Fe NP growth on HOPG is temperature-dependent. The generated Fe NPs on HOPG provide the basis for subsequent studies in this dissertation.

REFERENCES

1. Lin, W.-C.; Lo, F.-Y.; Huang, Y.-Y.; Wang, C.-H.; Chern, M.-Y., Cantd Magnetization in Fe Thin Films on Highly Oriented Pyrolytic Graphite. *J. Appl. Phys.* **2011,** *110*, 083911.
2. Chen, L.; Yelon, A.; Sacher, E., The Effect of Deposition Rate on the Morphology of Fe Nanoparticles on Highly Oriented Pyrolytic Graphite, As Studied by X-ray Photoelectron Spectrosocopy and Atomic Force Microscopy. *J. Phys. Chem. C* **2011,** *115*, 1524-1534.
3. Appy, D.; Lei, H.; Wang, C.-Z.; Tringides, M. C.; Liu, D.-J.; Evans, J. W.; Thiel, P. A., Transition metals on the (0001) surface of graphite: Fundamental aspects of adsorption, diffusion, and morphology. *Progress in Surface Science* **2014,** *89*, 219-238.
4. Paredes, J. I.; Martinez-Alonso, A.; Tascon, J. M. D., Comparative study of the air and oxygen plasma oxidation of highly oriented pyrolytic graphite: a scanning tunneling and atomic force microscopy investigation. *Carbon* **2000,** *38*, 1183-1197.
5. Taing, J.; Cheng, M. H.; Hemminger, J. C., Photodepositon of Ag or Pt onto TiO_2 Nanoparticles Decorated on Step Edges of HOPG. *ACS Nano* **2011,** *5* (8), 6325-6333.
6. Cross, C. E.; Hemminger, J. C.; Penner, R. M., *Langmuir* **2007,** *23*, 10372-10379.
7. Luo, W.; Veer, W. V. d.; Chu, P.; Mills, D. L.; Penner, R. M.; Hemminger, J. C., Polarization-Dependent Surface Enhanced Raman Scattering from Silver 1D Nanoparticle Arrays. *J. Phys. Chem. C* **2008,** *112* (31), 11609-11613.
8. Francis, G. M.; Kuipers, L.; Cleaver, J. R. A.; Palmer, R. E., Diffusion Controlled Growth of Metallic Nanoclusters at Selected Surface Sites. *J. Appl. Phys.* **1996,** *79*, 2942-2947.
9. Stabel, A.; Eichhorst-Gerner, K.; Rabe, J. P.; Gonzalez-Elipe, A. R., Surface Defects and Homogeneous Distribution of Silver Particles on Highly Oriented Pyrolytic Graphite. *Langmuir* **1998,** *14*, 7324-7326.
10. Diaz-Fernandez, D.; Mendez, J.; Bomati-Miguel, O.; Yubero, F.; Mossanek, R. J. O.; Abbate, M.; Dominguez-Canizares, G.; Gutierrez, A.; Tougaard, S.; Soriano, L., The Growth of Cobalt Oxides on HOPG and SiO_2 Surfaces: A Comparative Study. *Surf. Sci.* **2014,** *624*, 145-153.
11. Yang, D. Q.; Sacher, E., Interaction of Evaporated Nickel Nanoparticles with Highly Oriented Pyrolytic Graphite: Back-bonding to Surface Defetcs, as Studied by X-ray Photoelectron Spectroscopy. *J. Phys. Chem. B* **2005,** *109*, 19329-19334.
12. Metois, J. J.; Heyraud, J. C.; Takeda, Y., Experimental conditions to obtain clean graphite surfaces. *Thin Solid Films* **1978,** *51*, 105.
13. Kholmanov, I. N.; Gavioli, L.; Fanetti, M.; Casella, M.; Cepek, C.; Mattevi, C.; Sancrotti, M., Effect of Substrate Surface Defects on the Morphology of Fe Film Deposited on Graphite. *Surf. Sci.* **2007,** *601*, 188-192.
14. Norgren, B.; Somers, M.; de Wit, J., *Surf. Interface Anal.* **1994,** *21*, 378.
15. Garcia, M.; Marco, J. F.; Ganecedo, J. R.; Exel, W.; Meisel, W., Surface spectroscopic study of the corrosion of ultrathin ^{57}Fe-evaporated and Langmuir-Blodgett films in humid SO_2 environments. *Surf. Interface Anal.* **2000,** *29*, 82-91.

CHAPTER 2

Conversion of Fe oxide to Fe disulfide using H_2S (g) and/or Elemental Sulfur

INTRODUCTION

Seeded Iron Pyrite (FeS_2) nanoparticles (NPs) can be prepared by converting Fe oxide to Fe disulfide (FeS_2) in gaseous sulfur atmosphere. Two different sulfur precursors can be used to convert Fe oxide to FeS_2. It is known that chemical reaction between Fe oxide and H_2S results in formation of FeS_2, Eq. 1. And the reverse reaction can be done by exposing FeS_2 to oxygen or air which then results in formation of Fe oxide and elemental sulfur.

$$Fe_2O_3\ (s) + 4\ H_2S\ (g) \rightarrow 2\ FeS_2\ (s) + 3\ H_2O\ (g) + H_2\ (g) \quad (1)$$

Elemental sulfur as a sulfur precursor is known to react with Fe oxide.[1] It is known that Fe_2O_3 or Fe_3O_4 heated under gaseous sulfur atmosphere, results in the conversion of FeS_2 as shown in Eq. 2 and 3.

$$2\ Fe_2O_3\ (s) + 11\ S \rightarrow 4\ FeS_2\ (s) + 3\ SO_2\ (g) \quad (2)$$

$$Fe_3O_4\ (s) + 8\ S \rightarrow 3\ FeS_2\ (s) + 2\ SO_2\ (g) \quad (3)$$

The phase diagram shown below (taken from Smestad *et al.*) was calculated for equilibrium condition of ternary system where Gibbs free energy and heat capacity at 350 °C is used.[1,2]

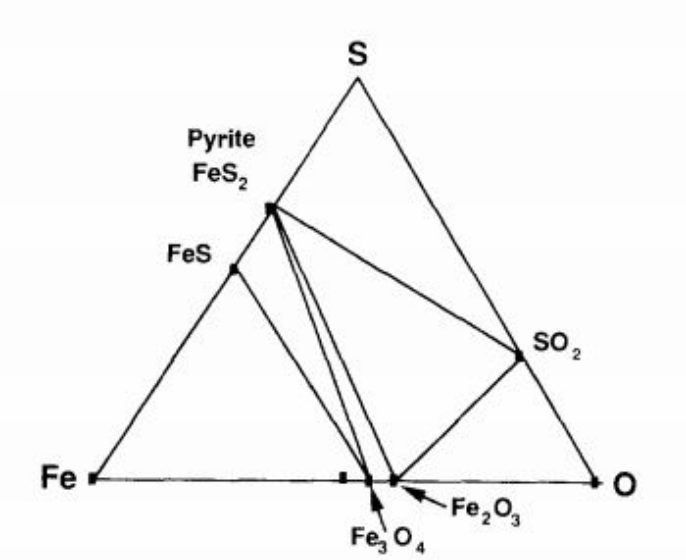

Figure 2.1. Fe-O-S phase diagram. Taken from Reference 1.

In order to prepare pyrite from metallic Fe in the absence of oxygen, it must to go through FeS phase. However, if pyrite is prepared by Fe_2O_3 or Fe_3O_4, then it would not be necessary to go through FeS phase field. Rather, as shown in Eq. 2 and 3, Fe oxide reacted with elemental sulfur, pyrite and SO_2 gas is produced. Since the equilibrium phase diagram was constructed at a condition of 350 °C, we are required to use the same or slightly higher temperature condition.

Here in this chapter, we explored two different ways convert Fe oxide to FeS_2: (1) Linearly ordered Fe oxide nanoparticles was placed in a chamber where pure H_2S gas was flown at 390 °C for 12 hours. (2) Elemental sulfur was placed along with Fe oxide nanoparticle array sample on HOPG in a quartz ampoule which were sealed then annealed at 500 °C for 0.5-2 hours.

EXPERIMENTAL

Conversion of Fe_3O_4 NCs to FeS_2 NCs by H_2S annealing. Samples were heated in pure quasi-static H_2S gas in a tube furnace at 390 °C for up to 12 hours.

Conversion of Fe_3O_4 and marcasite NCs to pyrite NCs by elemental sulfur annealing. Samples were annealed in evacuated (< 100 mTorr) and sealed 14 mm ID quartz ampoules containing ~20 mg of elemental sulfur (99.999%, Alfa Aesar) in a box furnace at 500-550 °C for up to 2 hours.

Characterization. Scanning Electron Microscopy (SEM) of FEI Magellan 400 XHR at 10 kV were used to image each samples after sulfur annealing. Transmitted Electron Microscope (FEI/Phillips CM-20) was used. TEM samples were prepared by cleaving sample surface with an adhesive tape. Only optically transparent areas were mounted on a carbon-free copper TEM grid (50/100 mesh double folding copper grids, Ted Pella). Raman measurements utilized a Renishaw inVia confocal Raman microscope with 532 nm excitation and a 50× objective lens.

RESULTS AND DISCUSSION

It has been reported that thin films of iron oxides can be converted to FeS_2 thin films by annealing in pure H_2S gas.[3] The same conditions (annealing Fe_3O_4 NCs in H_2S at 390 °C for 12 hours) were chosen for H_2S annealing. The particle size of iron oxides measured by SEM before H_2S annealing showed an average diameter of 40 nm. The H_2S annealing condition led to the formation of aligned polycrystalline FeS_2 nanowires that were 50 ± 15 nm wide and microns to millimeters long (Figure 2.2). These nanowires were around 100 nm in height (Figure 2.3). After the annealing process, individually separated particles coalesced together and formed nanowires (Figure 2.2 and 2.3). The slight expansion of particle size is due to the increase in unit cell volume from Fe_2O_3 to FeS_2.

The composition and crystallinity of these nanowires were determined by Raman and TEM. Raman spectra acquired over large areas of the samples (spot size of around 1 μm) showed the presence of both pyrite FeS_2 (peaks at 343, 379, and 430 cm^{-1}) and marcasite FeS_2 (peaks at 323 and 391 cm^{-1}; Figure 2.4).[4]

It was unclear how to exactly locate the presence of each phase in the nanowires due to the relatively large spot size in Raman. XRD data on these samples were negligible due to the low S/N ratio caused by a strong substrate signal. Thus, lattice-resolved TEM images of exfoliated HOPG samples were used to better understand the nanoscale structure of the nanowires. As shown in Figure 2.5, the wires consisted of crystalline grains with an average size of 50 nm, surrounded by a discontinuous shell of smaller crystallites and amorphous material. A *d* spacing of 2.7 Å was measured from the lattice fringes and fast Fourier transform (FFT) in the blue box region corresponded to either (200) lattice planes of pyrite or the (020) planes of marcasite. The FFT of the red box region showed (020) planes of marcasite and (120) plane of

marcasite (indicated by red arrows). This result indicates that the initial conversion of Fe_2O_3/Fe_3O_4 to FeS_2 is independent in NPs.

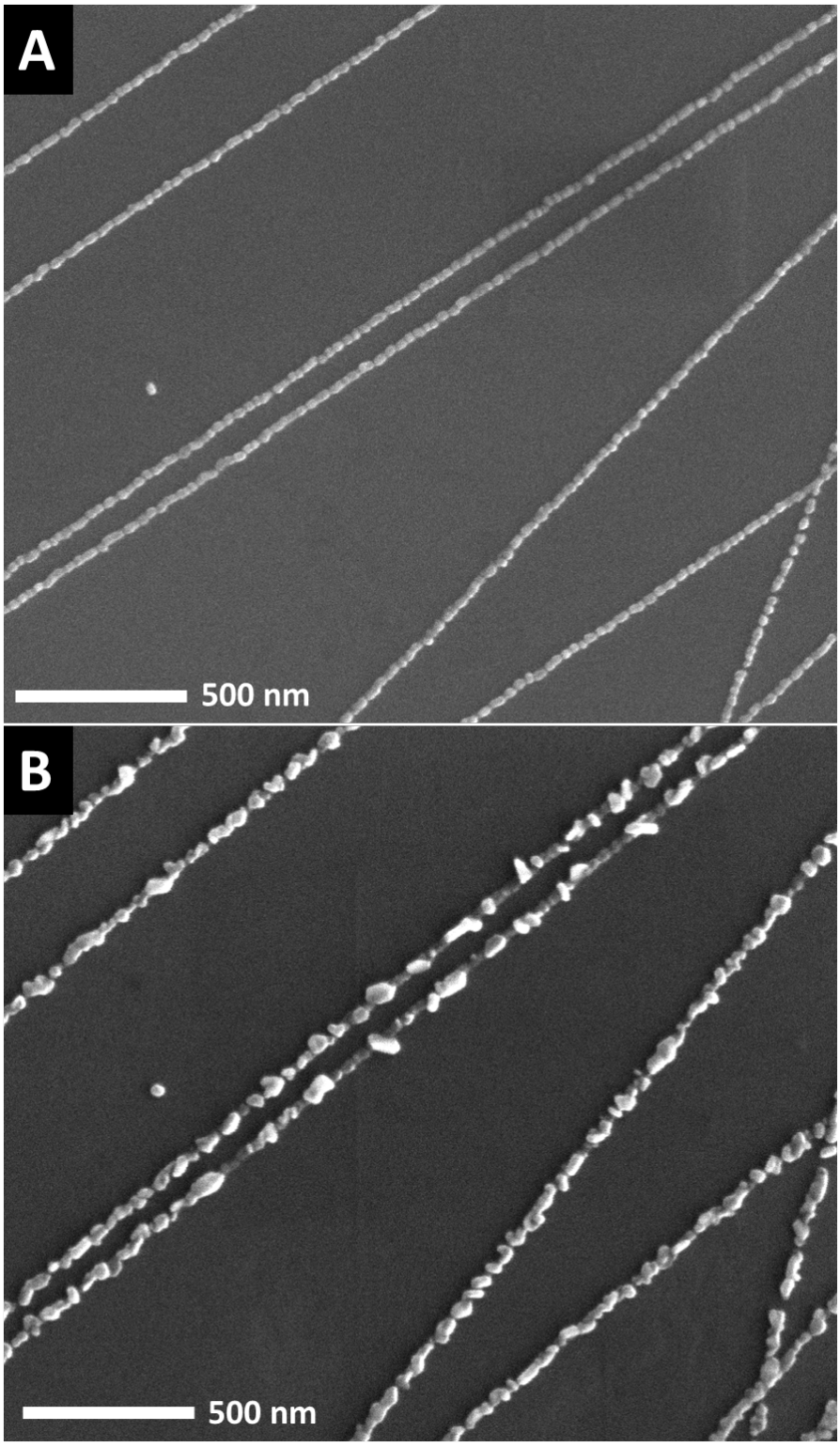

Figure 2.2. SEM images of Fe oxide NP arrays annealed in H_2S gas. (A) before H_2S annealing (B) after H_2S annealing.

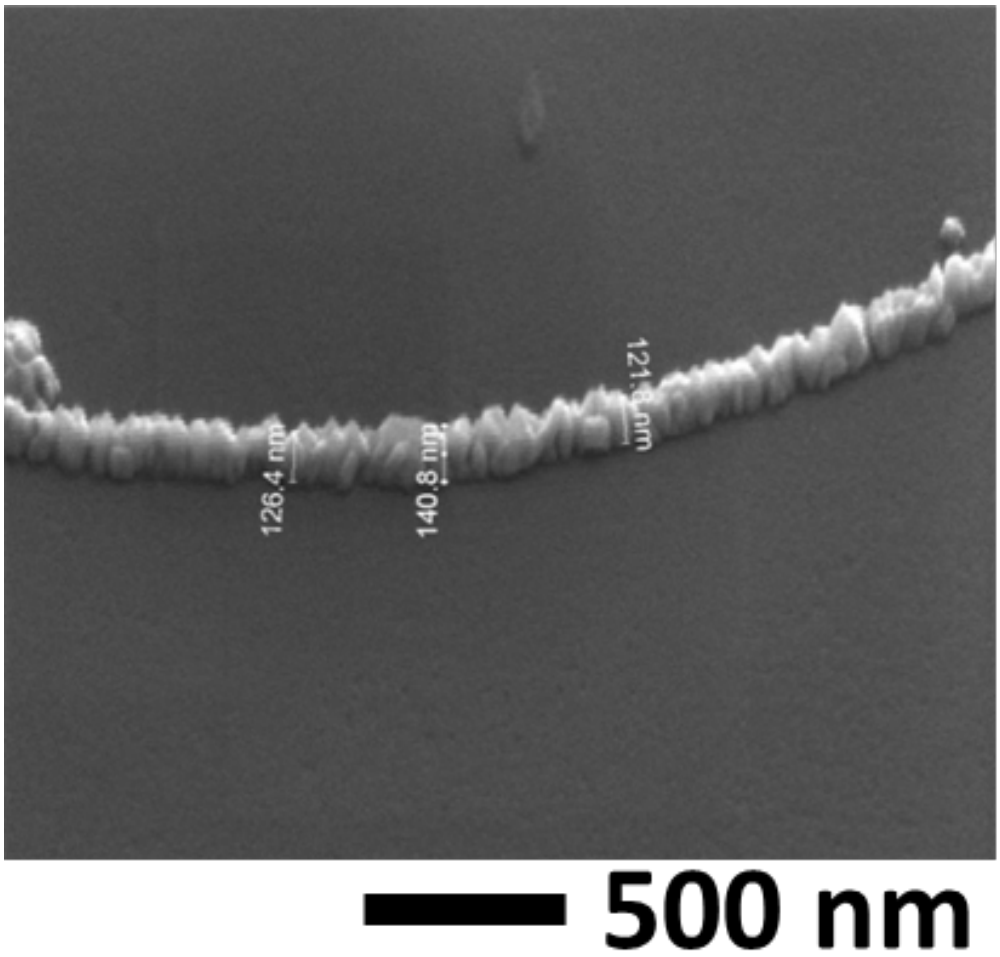

Figure 2.3. A 52 °-tilted SEM image of FeS_2 (pyrite and marcasite) nanowires after the H_2S annealing process.

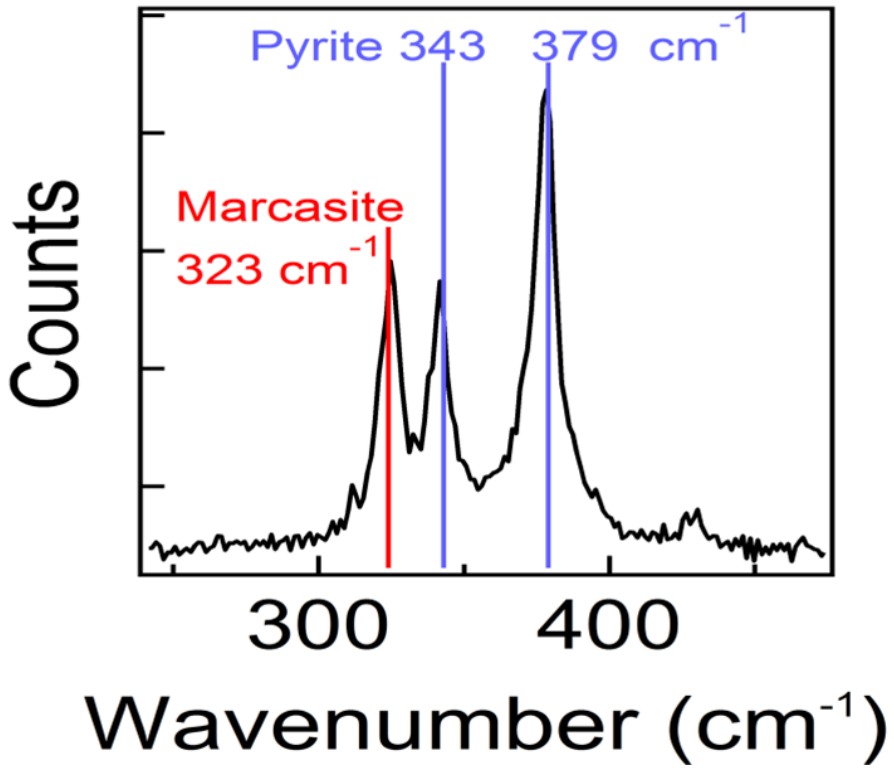

Figure 2.4. Raman spectrum of H_2S annealed Fe oxide NP arrays. Both pyrite (blue line) and marcasite (red line) phases of FeS_2 are present.

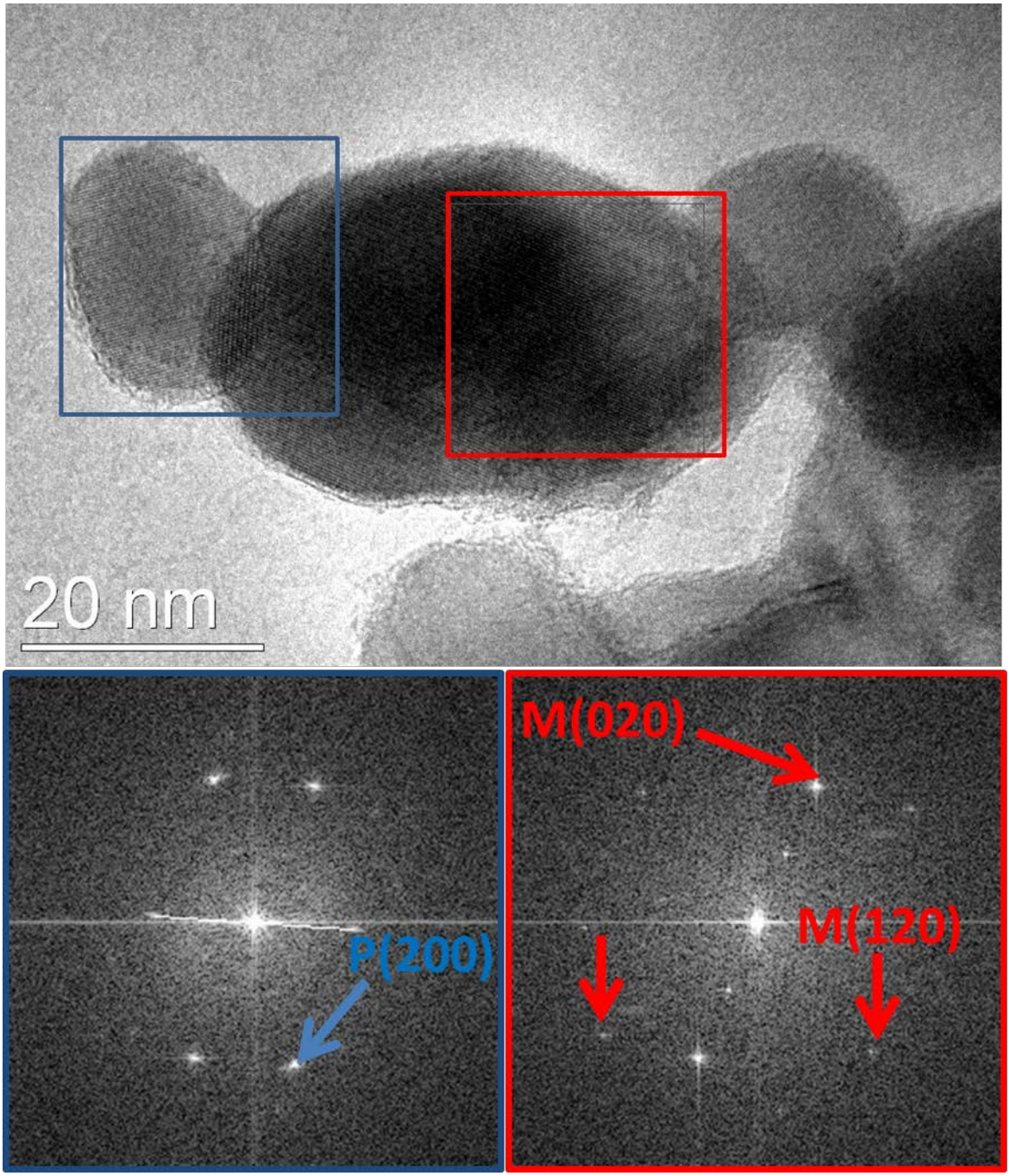

Figure 2.5. TEM images of after H_2S annealing process. Lattice resolved TEM image of a segment of a nanowires with fast Fourier transform (FFT) images of selected regions of the nanowire indicating (200) orientation of pyrite (blue arrows) and both (200) pyrite and (120) orientation of marcasite (red arrows).

Despite the mixed phases of FeS_2, we found that the H_2S annealing process on Fe_2O_3 linear NPs can maintain uniformity of the nanowire morphology, enabling us to study the seed-mediated growth of pyrite by CVD (chapter 3). However, our interest in synthesizing a pure pyrite phase led us to use other sulfur sources in the annealing process. Although we could not identify exactly the presence of Fe_3O_4 in nanoparticles, we could not neglect its presence. It is known that hematite (Fe_2O_3) and magnetite (Fe_3O_4) can be converted to FeS_2 by annealing in sulfur vapor.[1] When Fe_3O_4 reacts with sulfur it produces pyrite and Fe_2O_3. This is the intermediate step to convert Fe oxide to pyrite. Thus, with excess sulfur, all oxide phases can be converted to pyrite. We annealed the Fe_2O_3 nanoparticle arrays in sulfur at 550 °C for 2 hours in sealed quartz ampoules, mimicking our recent work with FeS_2 thin films.[3,4] The Fe_2O_3 NP chains were morphologically stable when heated to 550 °C in vacuum or argon (Figure 2.6) enabling us to interpret any morphological changes during sulfur annealing to the action of sulfur and no other variables.

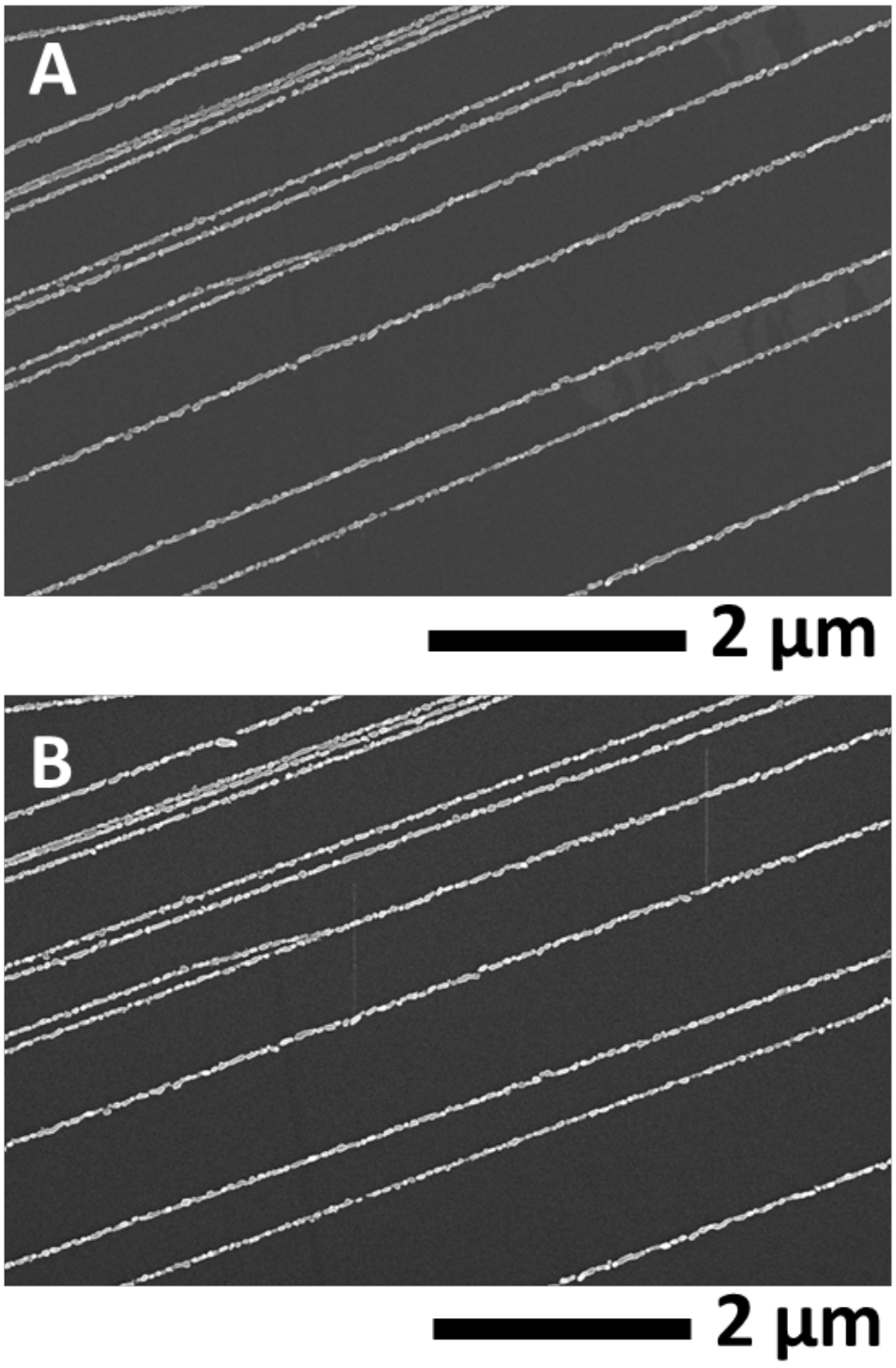

Figure 2.6. SEM images of before and after annealing at 550 °C for 2 hours for stability studies. (A) Before annealing. (B) after annealing of the same location.

Sulfur annealing under these conditions resulted in a loss of NP morphology uniformity and the formation of large (100-1000nm), polydispersed, and faceted crystallites of pyrite organized into branched chains across the HOPG surface (Figure 2.7). Interestingly, these crystallites were formed where the Fe oxide NPs were before the elemental sulfur annealing process. In addition to these micron-sized clusters, the faint trails of NP chains remained in the same size even after the sulfur annealing process. Despite the loss of morphology uniformity, the Raman spectrum in Figure 2.8 indicates the presence of a pure pyrite phase. TEM images in Figure 2.9 confirmed that the elemental sulfur annealing process produced crystallites with some particles remaining in NP size. Figure 2.9B represents one of a small NPs on Figure 2.9A. A d-spacing of 3.1 Å and 2.7 Å were measured from the lattice fringes which corresponded to (111) and (200) orientation of pyrite. Figure 2.9C is an image of a facetted region of large crystallites. The fast Fourier transform (FFT) for the black box region at the center (Figure 2.9C) represented (210) orientation of pyrite (d-spacing of 2.4 Å). Although mixed morphology was observed from elemental sulfur annealing process, all the Fe_2O_3 particles were successfully converted to pyrite.

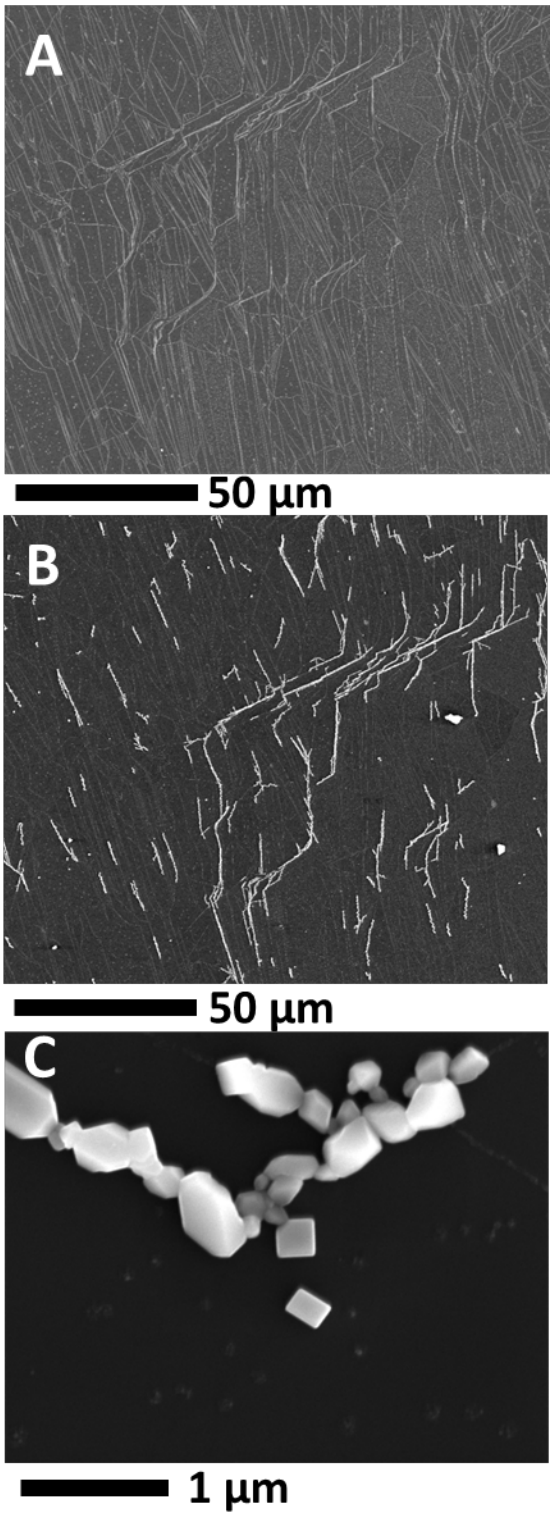

Figure 2.7. SEM images of Fe oxide NP arrays annealed in sulfur vapor. (A) Before sulfur annealing. (B) After sulfur annealing. (C) Higher magnification view of (B).

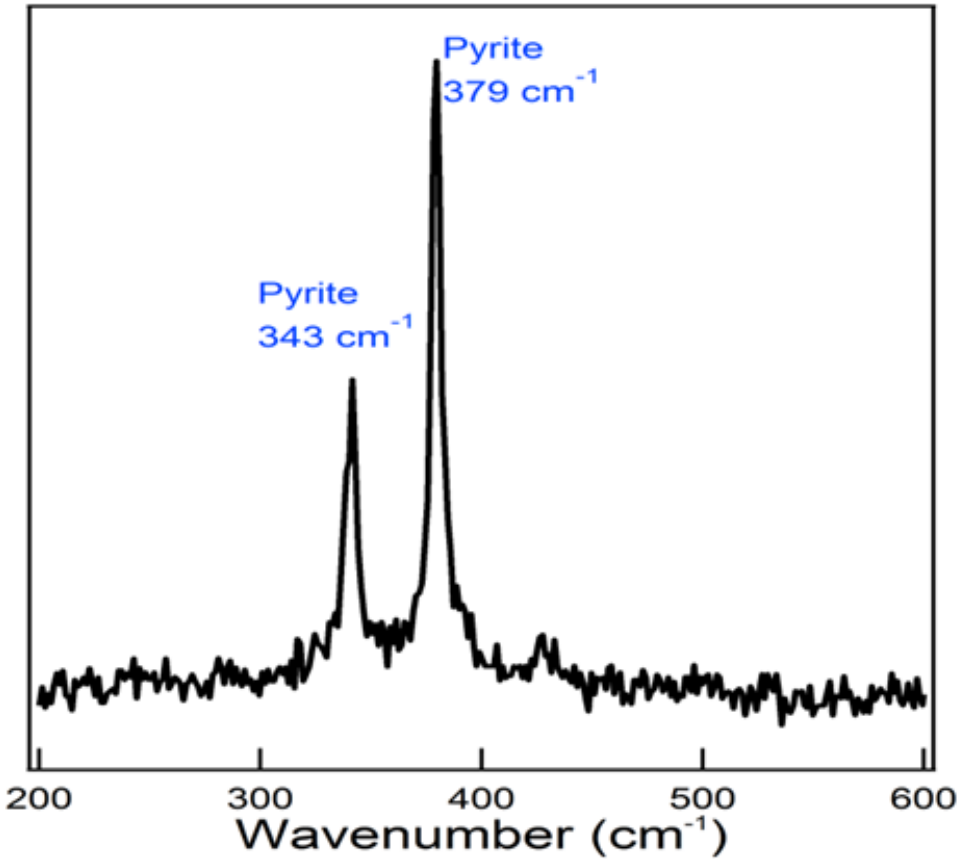

Figure 2.8. Raman spectrum of Fe oxide NP arrays annealed in sulfur vapor. Only pyrite phase of FeS_2 is present.

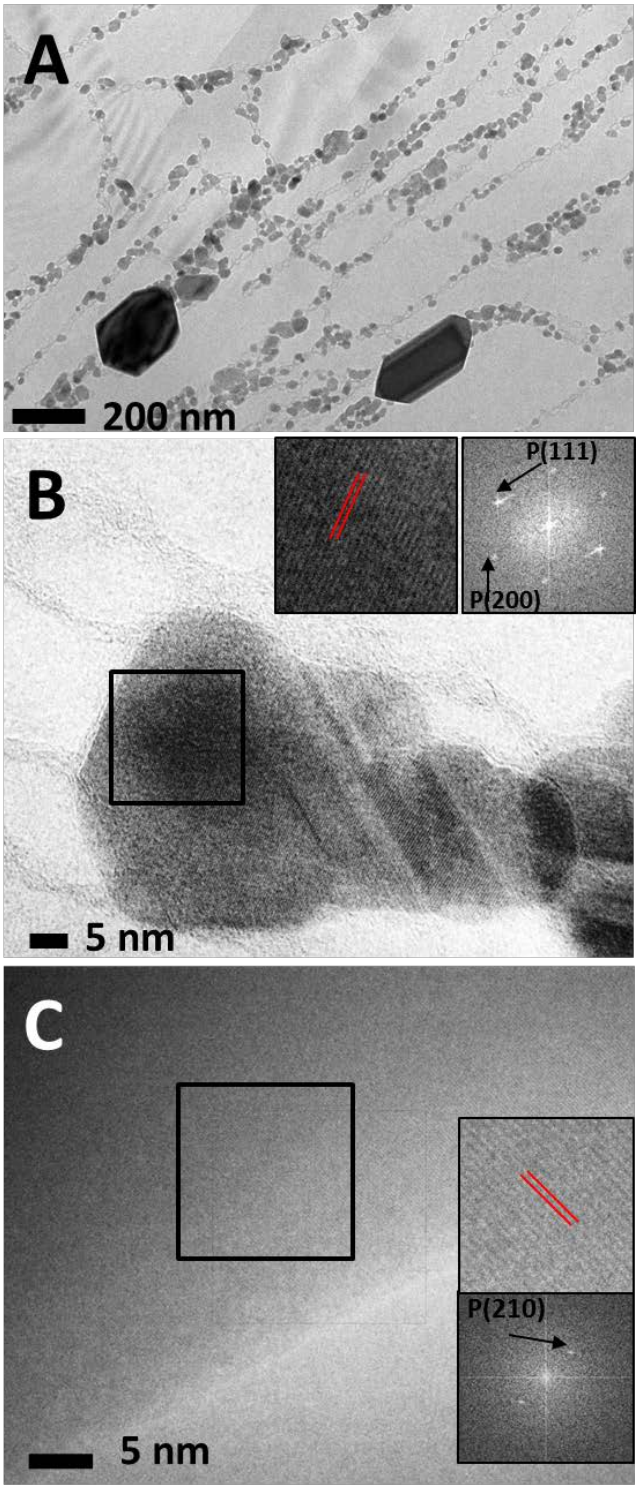

Figure 2.9. TEM images of Fe oxide NP arrays annealed in sulfur vapor. (a) Low-magnification TEM image. (b) TEM image of small nanoparticles on (a) and its FFT corresponds to (200) and (111) orientation of pyrite. (c) TEM image of large crystallite on (a) and its FFT corresponding (210) orientation of pyrite.

CONCLUSION

We show successful fabrication of pyrite nucleation sites on HOPG. This was done by converting linearly ordered arrays of Fe_2O_3 NPs (presented in chapter 1) using two different sulfur annealing processes. The H_2S annealing method converted the NPs to mixed phases of FeS_2 nanowires. The elemental sulfur annealing method converted the NPs to a pure pyrite phase despite a loss in uniformity of the NP or nanowire structures. These studies provide a platform for studying the basic mechanism of seed-mediated growth of pyrite presented in chapter 3.

REFERENCES

1. Smestad, G.; Ennaoui, A.; Fiechter, S.; Tributsch, H.; Hofmann, W. K.; Birkholz, M., Photoactive thin film semiconducting Iron pyrite prepared by sulfurization of Iron oxides. *Sol. ENerg. Mat.* **1990,** *20*, 149-165.
2. Barton, P. B.; Kullerud, G., The Fe-Zn-S system. *Carnegie Inst. Wash. Year Book* **1957,** *57*, 227-229.
3. Seefeld, S.; Limpinsel, M.; Liu, Y.; Farhi, N.; Weber, Z.; Zhang, Y.; Berry, N.; Kwon, Y.; Perkins, Y.; Hemminger, J. C., Iron Pyrite THin Films Synthesized from an $Fe(acac)_3$ Ink. *J. Amer. Chem Soc.* **2013,** *135*, 4412-4424.
4. Berry, N.; Cheng, M.; Perkins, C. L.; Limpinsel, M.; Hemminger, J. C.; Law, M., Atmospheric-Pressure Chemical Vapor Deposition of Iron Pyrite Thin Films. *Adv. Energy. Mater.* **2012,** *2* (9), 1124-1135.

CHAPTER 3

FeS_2 Nanoparticle Growth by Chemical Vapor Deposition

INTRODUCTION

Iron pyrite (cubic FeS_2), one of the phases in the Fe-S system, is a promising material for photovoltaic devices. It has a suitable bandgap (E_g ~ 0.85-0.95 eV), high absorption coefficient ($\alpha > 10^5$ cm^{-1} for hv > 1.3-1.4 eV), adequate minority carrier diffusion length, elemental abundance, and low toxicity.[1,2,3,4,5,6] However, iron disulfide (FeS_2) exists in numerous forms with unique electronic and magnetic properties depending on its stoichiometric ratio between Fe and S and its crystallinity. Fabrication of high quality pyrite film has been studied by numerous methods such as metal organic chemical vapor deposition (MOCVD).[6] Importantly, due to its naturally occurring phases, generation of a pure pyrite phase is still a challenge in the field. In addition, high temperature conditions can change the stoichiometry of Fe and S that can interfere with the generation of a pure pyrite phase. Consequently, despite its potential, the efficiency of pyrite solar cells has not exceeded ~3% due to a low open-circuit voltage (V_{oc} < 0.2 V).[1, 7,8] Therefore, basic studies on controlling pyrite nucleation and growth would potentially be useful in improving the fabrication of pure pyrite phases. This will have direct implication in improving film quality and device efficiency. Several studies have investigated the growth of pyrite nanostructures of controlled size and shape, including nanoparticles (NPs),[9,10,11] nanowires,[12] hexagonal sheets,[13] and nanocubes.[13,14,15] Most of the studies were done by colloidal synthesis, but none of the studies were done using a non-solution method.

It is known from solution chemistry that recrystallization is most effective when a seed particle is added in the solution by initiating crystal growth. In this chapter, we asked the question of whether pre-deposited pyrite seed NPs on HOPG step edges (illustrated in chapter 1 and 2) would provide an advantage in subsequent pyrite growth by CVD.

EXPERIMENTAL

Chemical vapor deposition of FeS_2. FeS_2 was deposited in a homemade atmospheric pressure CVD system described in detail elsewhere[16] using iron(III) acetylacetonate (≥ 99.9%, Aldrich) and *tert*-butyl disulfide (97%, Aldrich) in flowing argon at a substrate temperature of 300 °C.

Structural and elemental characterization. Scanning electron microscopy (SEM) imaging was performed on an FEI Magellan 400 XHR instrument at 10 kV. Raman measurements utilized a Renishaw inVia confocal Raman microscope with 532 nm excitation and a 50× objective lens. X-ray Diffraction was performed on Rigaku Smartlab XRD.

RESULTS AND DISCUSSION

The converted FeS_2 NPs by distinct annealing procedures allowed us to ask two questions about the basic growth mechanism of pyrite: i) Can FeS_2 NPs act as a seed to assist preferential growth of pyrite upon CVD? ii) Is this growth process-dependent? We used CVD of iron(III) acetylacetonate and *tert*-butyl disulfide at 300 °C (see Experimental for details) onto either H_2S-annealed or sulfur-annealed samples.

Striking differences were seen where CVD on H_2S-annealed samples maintained the mixed-phase pyrite/marcasite nanowires (Figure 3.1-3), while CVD on sulfur-annealed samples generated chains of pure-phase pyrite microcrystals and nanocrystals (Figure 3.4-6) suggesting a process-dependent growth of pyrite.

A short time series (10, 15, 20, 30 minutes) of CVD was monitored on H_2S-annealed HOPG sample (Figure 3.1-3.3). Initial 10 minutes of CVD growth resulted in a deposition on to the pre-existing nanowires. Figure 3.1A and B is the same sample at a similar location before and after 10 minutes of CVD. The exact same location could not be compared due to the beam damage that happens during SEM acquisition. It is known that during the CVD process, deposition is favored in the beam-damaged area. During a short CVD exposure, particles only deposited on to pre-existing nanowires. Rather than epitaxial growth, as might be expected, we observed the nucleation of multiple new grains on each seed crystal, with no obvious crystallographic registry between the new grains and the seeds. Upon 15 minutes of CVD, amorphous seed nanowires became more crystalline (Figure 3.2C). The new grains on each seed crystals became more facetted. Importantly, we observed preferential growth of new particles on the pre-exisiting nanowires since no growth was observed on the terraces. As the time increased to 20 minutes, new particles that were deposited on nanowires became crystalline (Figure 3.2D).

At 30 minutes of CVD exposure, pre-exited nanowires became crystalline and amorphous particles started to expand throughout the substrate from the nanowires (Figure 3.3E). As shown above, Raman spectra indicated the presence of both marcasite and pyrite phases after H_2S annealing (Figure 3.3F; blue line). It is clear that the existence of both phases before CVD affected the growth of new particles. After 10 minutes and 30 minutes of CVD exposure, both marcasite and pyrite phases were still present (Figure 3.3F; green and red line).

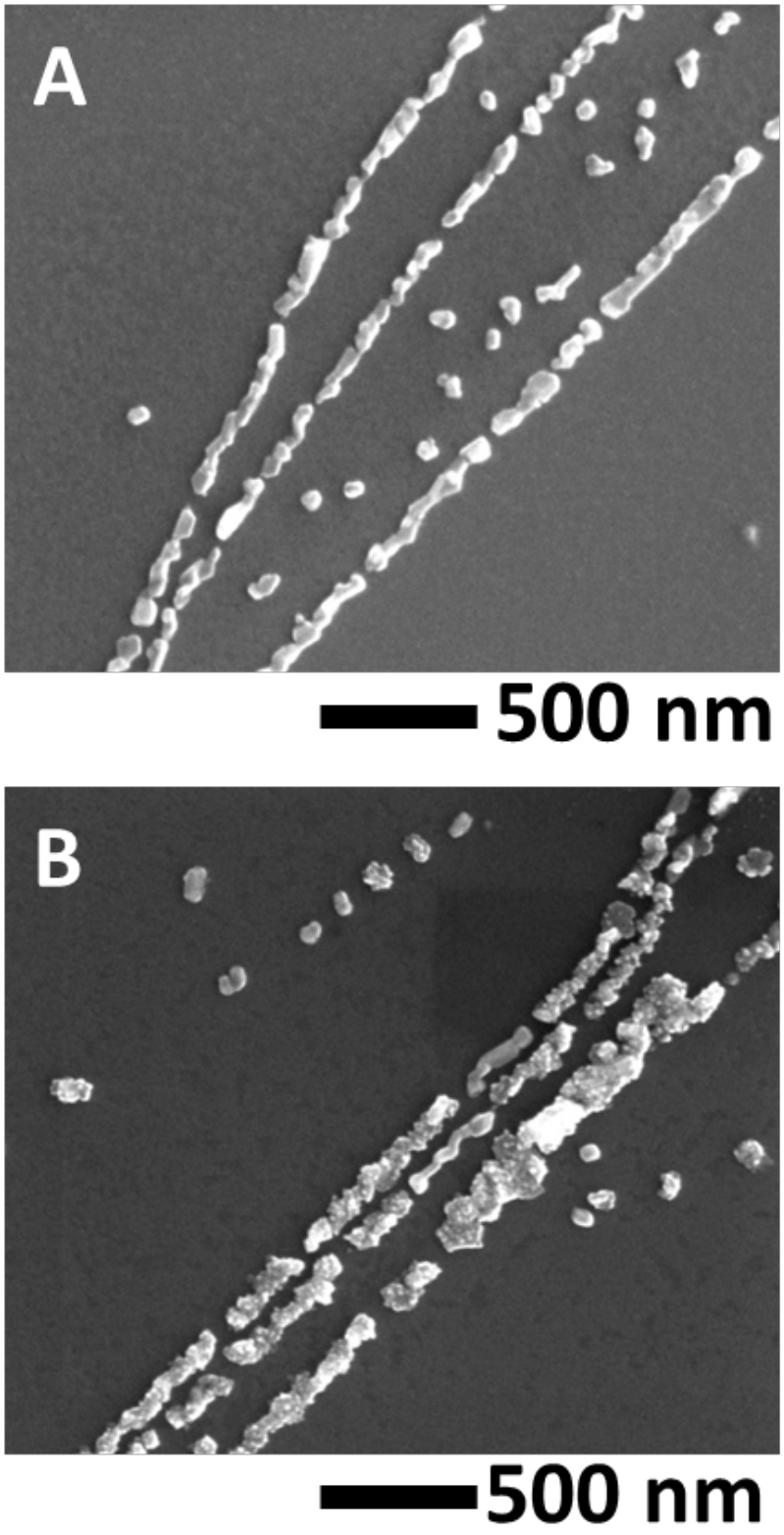

Figure 3.1. SEM images of before and after CVD in different time series on H_2S-annealed sample. (A) Before CVD. (B) 10 minutes of CVD exposure.

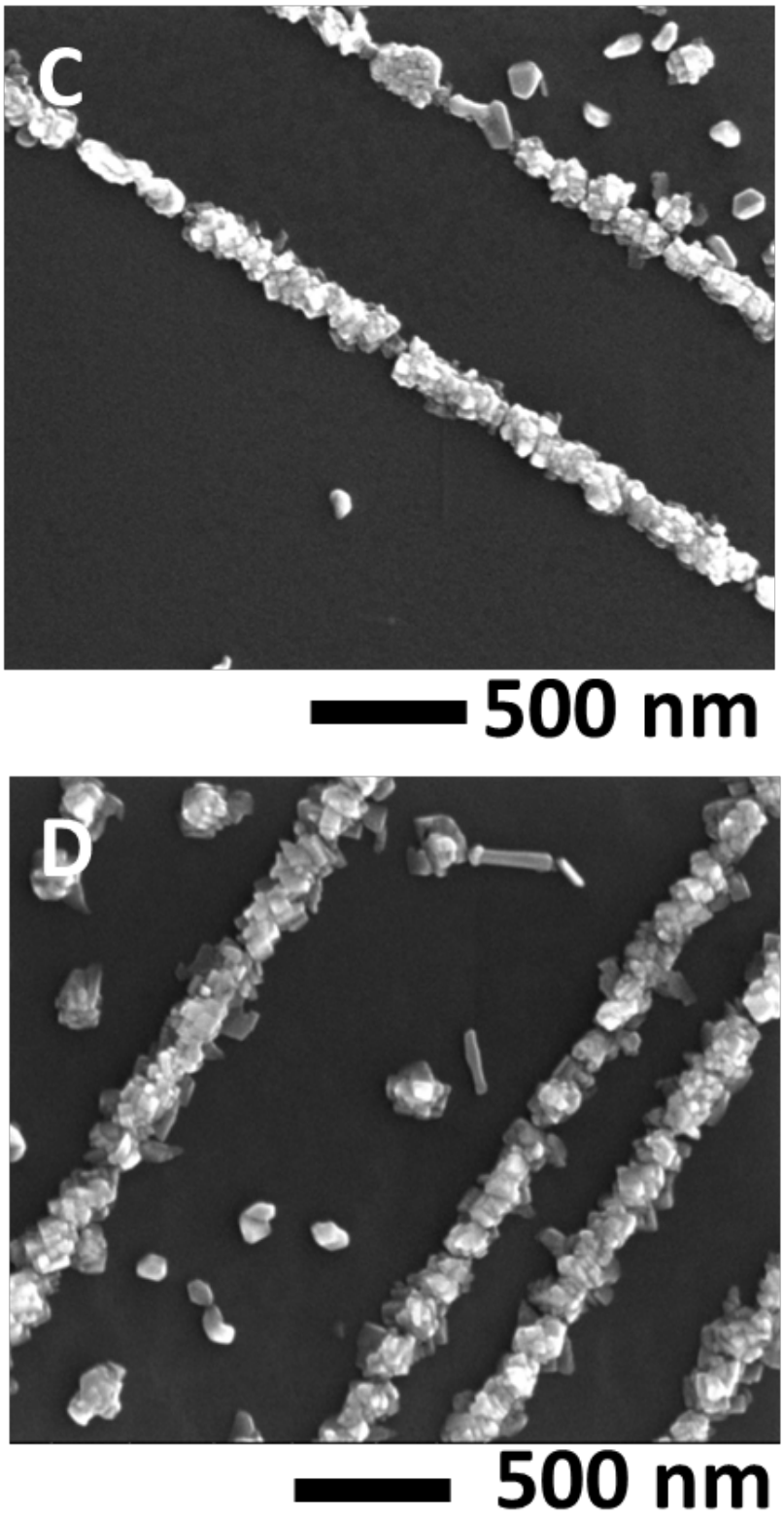

Figure 3.2. SEM images of after CVD in different time series on H_2S-annealed sample. (C) 15 minutes of CVD exposure. (D). 20 minutes of CVD exposure.

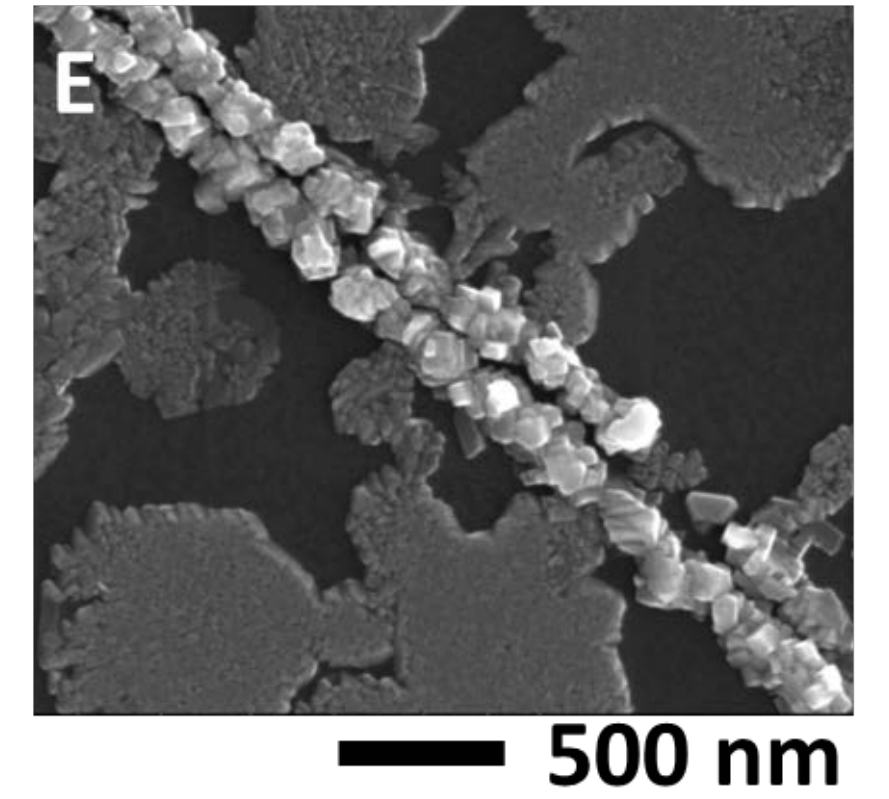

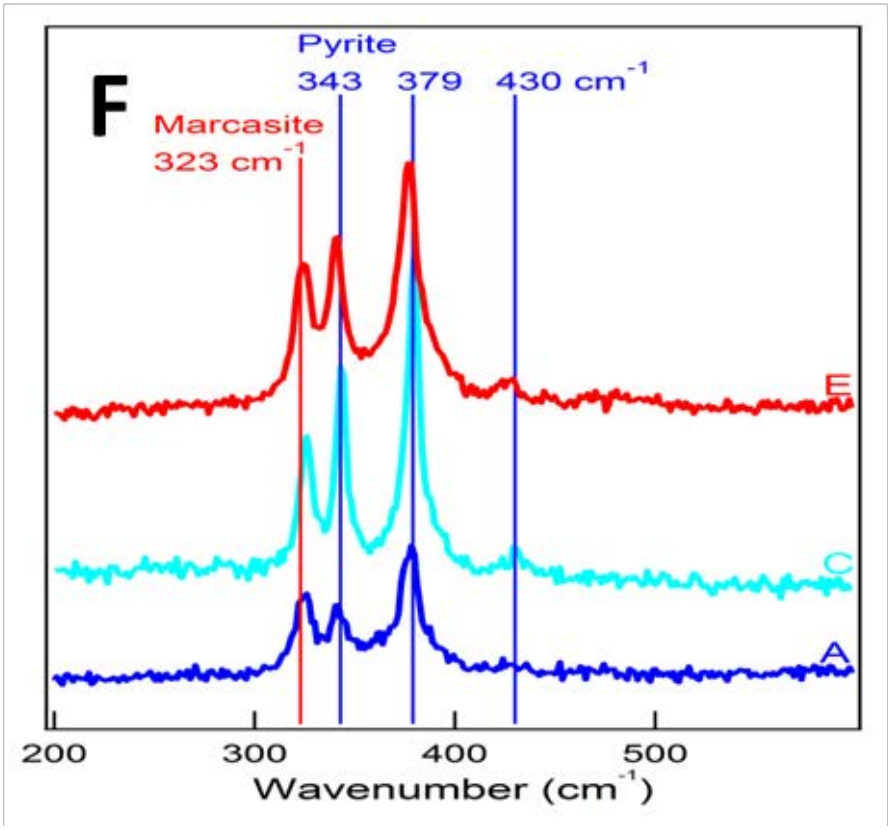

Figure 3.3. SEM image of after CVD and Raman spectra. (D) 30 minutes of CVD. (F) Raman spectra of (A), (C), and (E).

Samples annealed in sulfur showed quite different behavior during initial CVD growth of FeS_2. The SEM image of sulfur annealed samples showed the aforementioned loss of morphology uniformity yet pure pyrite phase (Figure 3.4A, 3.5C). Upon a short CVD exposure of 5 minutes (Figure 3.4B), we observed nucleation of FeS_2 on the entire substrate indicating no preferential growth. However, we still observed a similar crystalline behavior as the H_2S-annealed sample at the pre-existing linear NP arrays of pyrite. CVD exposure for 20 minutes resulted in an agglomeration of particles at the surface. Interestingly, due to the presence of only pyrite phase prior to CVD, pyrite-pure growth was observed with short-time CVD deposition when measured by Raman spectroscopy (Figure 3.6F). As the CVD deposition time increased, marcasite phase started to grow as well as the pyrite phase (data not shown).

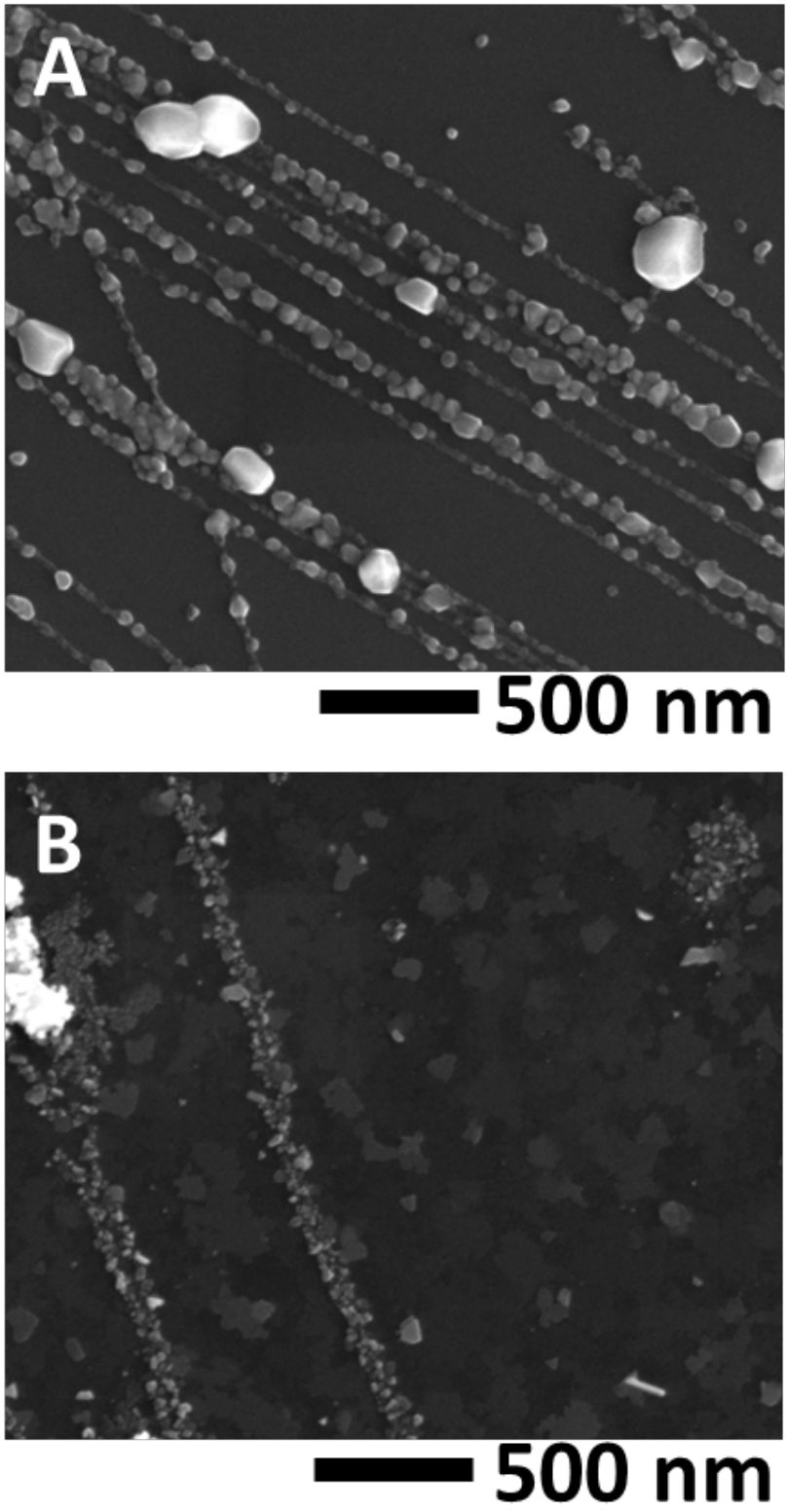

Figure 3.4. SEM images of before and after CVD in different time series on sulfur-annealed sample. (A) before CVD. (B) 5 minutes of CVD.

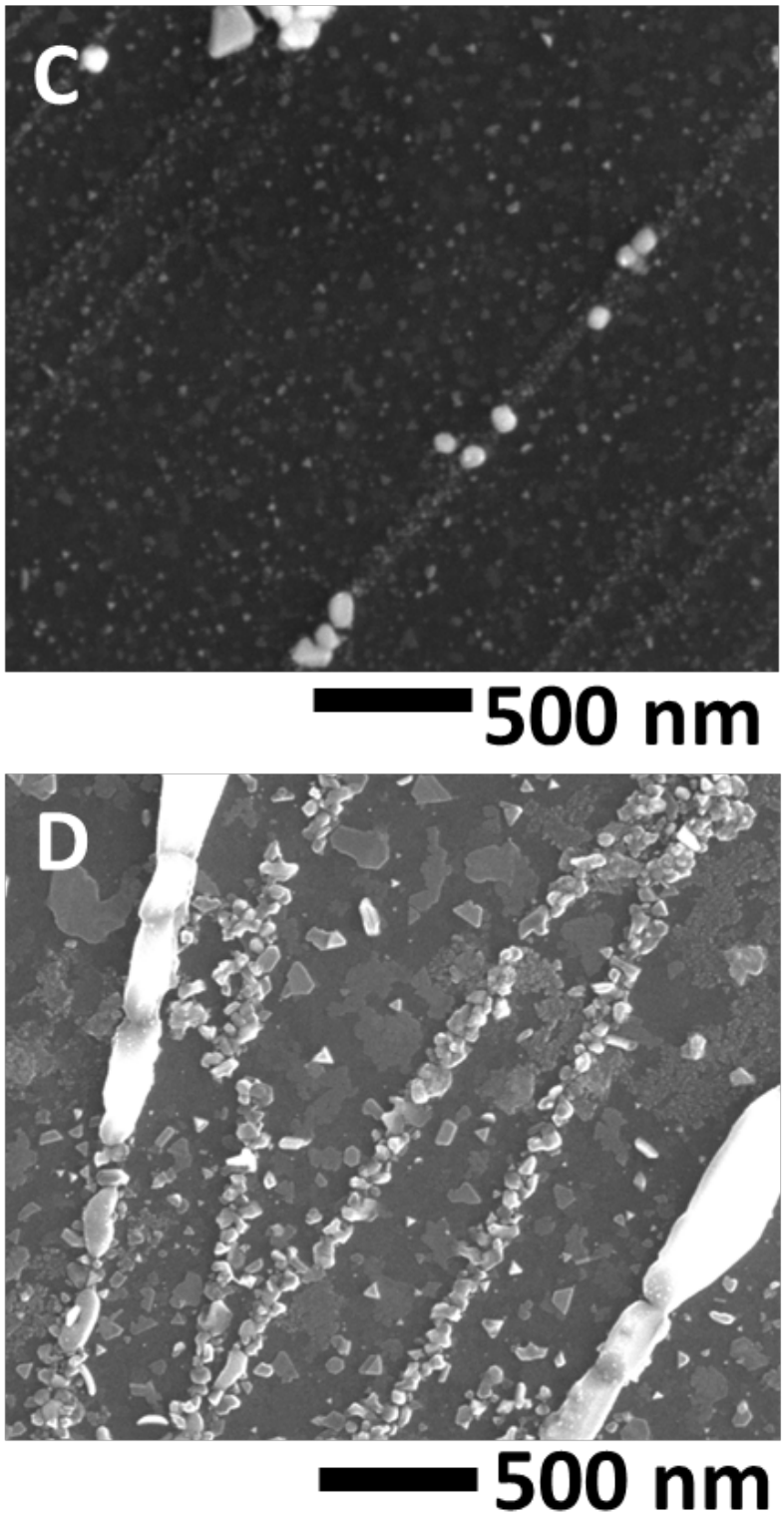

Figure 3.5. SEM image of after CVD in different time series on sulfur-annealed sample. (C). 10 minutes of CVD. (D) 15minutes of CVD.

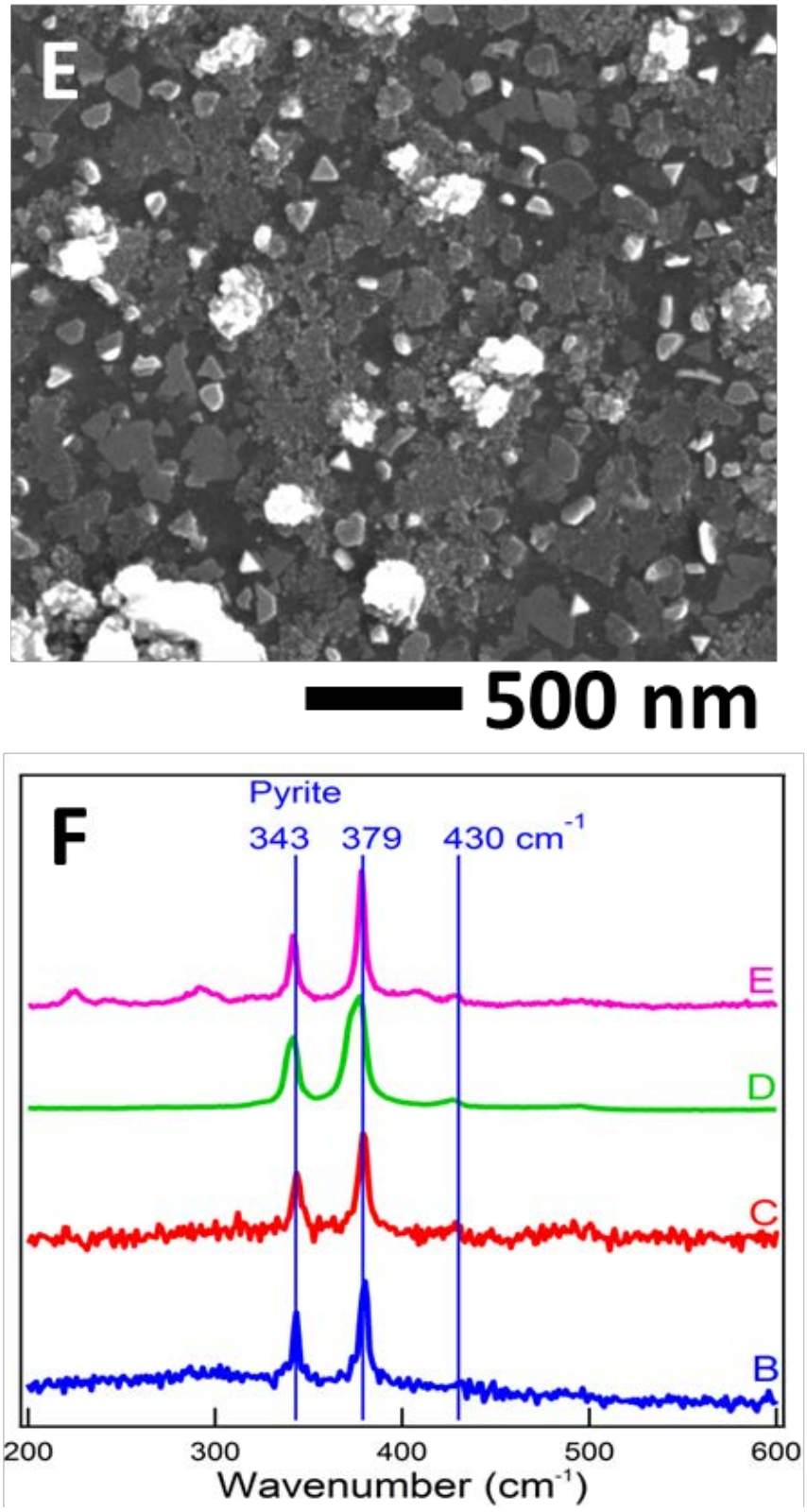

Figure 3.6. SEM image of after CVD and Raman spectra. (D) 20 minutes of CVD. (F) Raman spectra of (B)-(E).

A possible explanation of the nonspecific nucleation of CVD FeS_2 on sulfur-annealed samples is the creation of nucleation sites on HOPG by the reaction between sulfur and carbon during the annealing treatment. To test this hypothesis, we compared CVD growth of FeS_2 on sulfur-annealed or blank HOPG substrates. As expected, 15 minutes of CVD exposure on blank HOPG substrate resulted in a predominant deposition of particles on the step edges that were taller and bigger than those on the terraces (Figure 3.7A). On the contrary sulfur-annealed HOPG showed no preferential growth at the step edges (Figure 3.7B). We used XRD to investigate potential structural changes to the HOPG surface (Figure 3.8). Interestingly, sulfur-annealed HOPG exhibited structural changes. HOPG mainly is composed of two different crystalline phases: hexagonal (2H) crystalline phase where hexagonal carbon layers are arranged in ABAB manner and rhombohedra structure of ABCABC staking of carbon layers (3R).[17] Although it is difficult to state that a freshly cleaved HOPG prior to XRD measurement has a particular preferential crystalline phase, clear distinction could be made on post-elemental sulfur treated HOPG. Sulfur-annealed HOPG showed a strong peak for 2H phases that was not present on the blank HOPG substrate. It has been reported that 2H phases can interchange upon heating at high temperature and interchanges between oxygen and sulfur can be made by annealing the sample in a sulfur environment.[17,18] This result indicated that upon sulfur-annealing, sulfur not only reacts with seed-particles but also with carbons on the HOPG, possibly leaving new nucleation sites on the terraces. This may explain the random distribution of particles on the sulfur-annealed HOPG substrate during CVD.

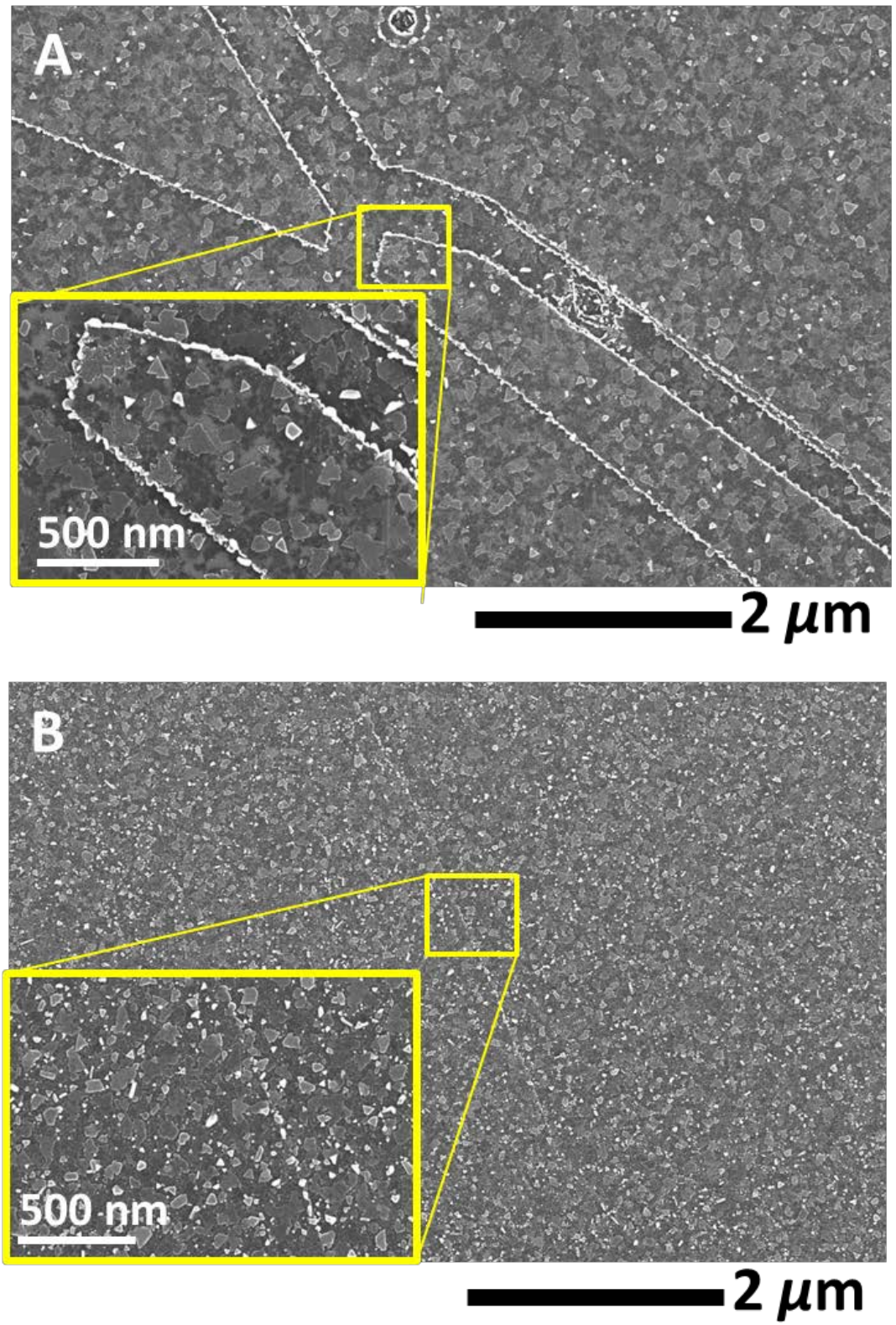

Figure 3.7. SEM images of CVD on (A) blank HOPG. (B) elemental sulfur annealed HOPG.

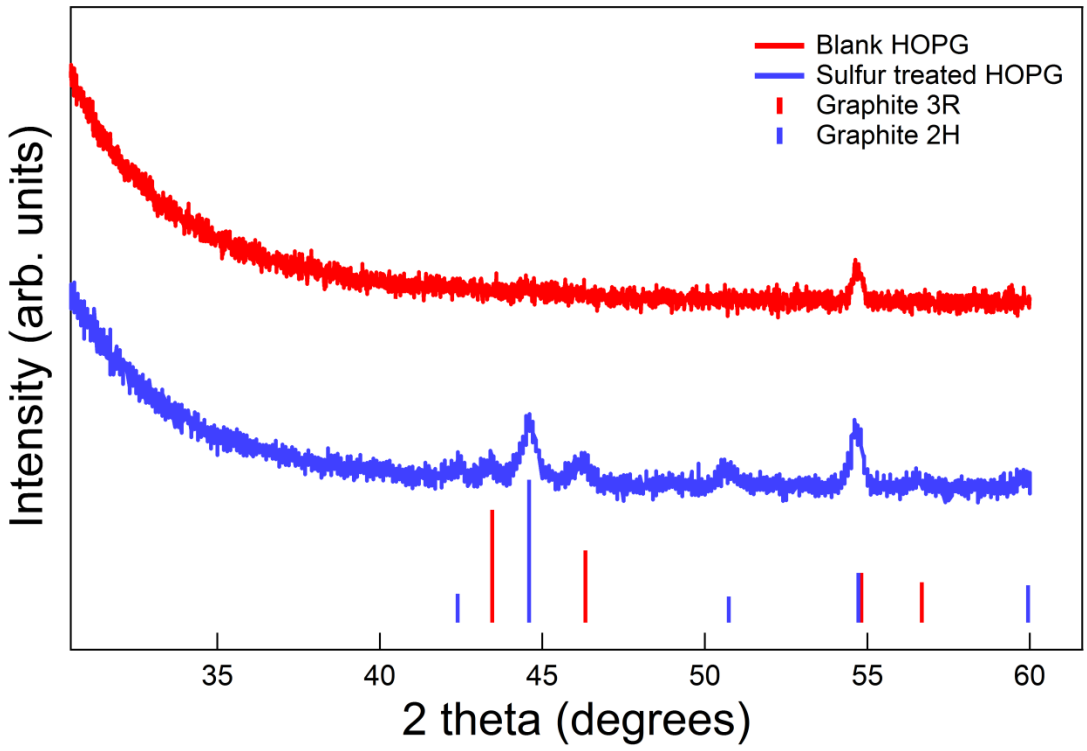

Figure 3.8. XRD of blank HOPG (red) and sulfur annealed HOPG (blue). Surface modification is observed with elemental sulfur annealed HOPG.

CONCLUSION

Here in this chapter, we show that preferential growth of pyrite on pre-existing seed particles was process dependent. Despite the presence of phase impurities, the H_2S annealing process suggested seed-mediated growth of FeS_2 nanowires. On the contrary, elemental sulfur annealing surprisingly resulted in the growth of pure pyrite phase with random distributions of new NPs. Future studies will be required to optimize the conditions to preferentially grow pure pyrite phase that can potentially be used to generate high quality pyrite films. In conclusion, our studies provided a novel platform to study seed-mediated growth of pyrite NPs independent from substrate effects. The preferential growth of NPs in a linearly ordered manner also provides an advantage for theoretical calculations.

REFERENCES

1. Ennaoui, A.; Tributsch, H., Energetic Characterization of the Photoactive Iron Disulfide (pyrite) Interface. *Sol. Energ. Mat.* **1986,** *14*, 461-474.
2. Smestad, G.; Ennaoui, A.; Fiechter, S.; Tributsch, H.; Hofmann, W. K.; Birkholz, M., Photoactive thin film semiconducting Iron pyrite prepared by sulfurization of Iron oxides. *Sol. ENerg. Mat.* **1990,** *20*, 149-165.
3. Altermatt, P. P.; Kiesewetter, T.; Ellmer, K.; Tributsch, H., Specifying Targets of Futer Research in Photovoltaic Devices Containing Pyrite (FeS_2) by Numerical Modelling. *Sol. Energ. Mat. Sol. Cells* **2002,** *71*, 181-195.
4. Wadia, C.; Alivisatos, A. P.; Kammen, D. M., Materials Availability Expands the Opportunity for Large-scale Photovoltaics Deployment. *Environ. Sci. Technol.* **2009,** *43*, 2072-2077.
5. Huang, L. Y.; Meng, L., Crystallographic Behavior of FeS_2 Films Formed on Different Substrates. *Mater. Chem. Phys.* **2010,** *124*, 413-416.
6. Berry, N.; Cheng, M.; Perkins, C. L.; Limpinsel, M.; Hemminger, J. C.; Law, M., Atmospheric-Pressure Chemical Vapor Deposition of Iron Pyrite Thin Films. *Adv. Energy. Mater.* **2012,** *2* (9), 1124-1135.
7. Ennaoui, A.; Fiechter, S.; Tributsch, H.; Giersig, M.; Vogel, R.; Weller, H., Photoelectrochemical Energy Conversion Obtained with Ultrathin Organo-metallic-chemical vapor deposition Layer of FeS_2 (pyrite) on Titanium Dioxide. *J. Electrochem. Soc.* **1992,** *139*, 2514-2518.
8. Antonucci, V.; Arico, A. S.; Giordano, N.; Antonucci, P. L.; Russo, U.; Cocke, D. L.; Crea, F., Photoactive Screen-Printed Pyrite Anodes for Electrochemical Photovoltaic Cells. *Sol. Cells* **1991,** *31*, 119-141.
9. Puthussery, J.; Seefeld, S.; Berry, N.; Gibbs, M.; Law, M., Colloidal Iron Pyrite (FeS_2) Nanocrystal Inks for Thin-Film PHotovoltaics. *J. Amer. Chem. Soc.* **2010,** *133*, 716-719.
10. Disale, S.; Garje, S., Growth of Nanocrystalline FeS and FeS_2 Using Iron(II) Cinnamaldehyde Thiosemicarbazone Complexes as Single-Source Precursors. *Adv. Sci. Lett* **2010,** *3*, 80.
11. Gong, M.; Kirkeminde, A.; Ren, S., Symmetry-Defying Iron Pyrite (FeS_2) Nanocrystals through Oriented Attachment. *Scientific Reports* **2013,** *3*, 2092.
12. Caban-Acevedo, M.; Faber, M. S.; Tan, Y.; Hamers, R. J.; Jin, S., Synthesis and Properties of Semiconducting Iron Pyrite (FeS_2) Nanowires. *Nano Lett.* **2012,** *12*, 1977-1982.
13. Kirkeminde, A.; Ruzicka, B. A.; Wang, R.; Puna, S.; Zhao, H.; Ren, S., Synthesis and Optoelectronic Properties of Two-Dimensinal FeS_2 Nanoplates. *ACS Appl. Mater. Interfaces* **2012,** *4*, 1174-1177.
14. Kirkeminde, A.; Scott, R.; Ren, S., All inorganic Iron Pyrite Nano-Heterojunction Solar Cells. *Nanoscale* **2012,** *4*, 7649-7654.
15. Macpherson, H. A.; Stoldt, C. R., Iron Pyrite Nanocubes: Size and Shape Considerations for Photovoltaic Application. *ACS Nano* **2012,** *6* (10), 8940-8949.
16. Berry, N.; Cheng, M.; Perkins, C. L.; Limpinsel, M.; Hemminger, J. C.; Law, M., Atmospheric-Pressure Chemical Vapor Deposition of Iron Pyrite Thin Films. *Adv. Energy. Mater.* **2012**.

17. Wu, K. Y.; Chen, W. Y.; Hwang, J.; Wei, H. K.; Kou, C. S.; Lee, C. Y.; Liu, Y. L.; Hwang, H. Y., Structure modification of highly ordered pyrolytic graphite by Ar plasma beam scanning at different incident angles. *Appl. Phys. A* **2009,** *95*, 707-712.
18. Poh, H. L.; Simek, P.; Sofer, Z.; Pumera, M., Sulfur-Doped Graphene via THermal Exfoliation of Graphite Oxide in H_2S, SO_2, or CS_2 Gas. *ACS Nano* **2013,** *7* (6), 5262-5272.

CHAPTER 4

Photocatalytic Properties of Photo-deposited Pt Nanoparticles on Iron oxide nanoparticle arrays

INTRODUCTION

There has been a wide range of studies on tunable nanoparticles (NPs) due to its wide applications in photovoltaics, biomedical imagings, photocatalysts, and electro-optical devices.[1,2,3,4] Especially, there has been extensive studies on heterostructures of NPs where two distinct metal components are synthesized to form a bimetallic system. These bimetallic catalysts have higher activity than single metallic NPs. Controlling the size and surface structure of these bimetallic systems has a key role in achieving high catalytic activity.[5] The most important factor for catalytic performance is the size of metal particles. It has been reported that sub-nanometer particles have both enhanced catalytic activity and selectivity than regular NPs.[6] Atoms that are in low-coordination sites function as active sites.[7] It is therefore, ideal to synthesize smaller NPs to single atoms. However, fabrication of single-atom catalysts is a challenge due to its stability under reaction conditions. Specifically, we are interested in metal-semiconductor hybrid systems have been of great interest due to their unique photocatalytic properties. In metal-semiconductor hybrid systems, semiconductors are used as light absorbing components. They absorb photons and create electron holes localized at the semiconductor, which are formed by excited electrons that move through the heterointerface.

Catalysts using Pt has been extensively studied due to their ideal catalytic properties, specifically in hydrogen oxidation and oxygen reduction in alternative fuel cell. However, due to its high cost and low abundance, developing Pt based catalysis has been limited. It is important

to use small amount of Pt and bring maximum catalytic properties of Pt. It is known that Fe_3O_4 nanoparticles conjuncted to Pt nanoparticles exhibit higher catalytic activity for oxygen reduction reaction (ORR), CO oxidation, and nitrite sensing. [3,5, 8,9,10,11]

Fe_2O_3 is a promising semiconductor photocatalyst due to its visible light absorption (E_g = 2.2 eV), abundance, non-toxicity, and stability against photo corrosion. However, Fe_2O_3 suffers from short hole diffusion length, low electrical conductivity and high rate of electron hole recombination. To overcome these barriers, different transition metals (e.g. Au, Si, Pt) have been deposited on Fe_2O_3. Particularly, Pt on Fe_2O_3 is an ideal heterogeneous catalyst that has a variety of uses such as photoelectrochemical water splitting and CO oxidation.[12] Importantly, Pt on Fe_2O_3 provides an improvement in photocatalytic properties on the degradation of dyes, such as methylene blue (MB). Although many studies deposit Pt on various forms of Fe_2O_3 (e.g. films, nanorods, and coreshells), Pt NPs on discrete Fe_2O_3 nanoparticles on highly oriented pyrolytic graphite (HOPG) has not been studied. The deposition of Pt on Fe_2O_3 has been studied using various methods such as electrodeposition and solution based synthesis. However, photodeposition of Pt on Fe_2O_3 has not yet been studied.

In this chapter, we demonstrate photodeposition of Pt NPs selectively on Fe_2O_3/Fe_3O_4 nanoparticle arrays formed by physical vapor deposition on HOPG. We find that Pt deposition on Fe_2O_3/Fe_3O_4 NP arrays enhances its photocatalytic properties as assessed by the degradation of methylene blue (MB).

EXPERIMENTAL

Physical Vapor Deposition of Fe_2O_3 onto the Steps of HOPG.

HOPG (Momentive Performance, ZYB Grade 12 × 12 mm) was freshly cleaved and immediately loaded onto tantalum sample holder in an evaporator (Edwards 306A coating system). The sample holder allowed electrical current to pass through and heat the graphite by resistive heating and a K-type thermocouple that was cemented on the back of the sample holder read the temperature of the sample holder as the heating process continues. The sample holder was at an angle of 57 ° from the ceramic crucible with Fe pieces (99.99 %, Alfa Aesar). The sample holder was gradually heated to 500 °C in 3 hours with a base pressure of $< 5 \times 10^{-7}$ torr. Fe was deposited onto HOPG held at around 500 °C with a uniform thickness of 2 nm measured from a quartz crystal microbalance (INFICON front load single crystal sensor) and annealed for 3 hours.

Photodeposition of Pt on Fe_2O_3 nanoparticles on HOPG.

A 0.1 mM of K_2PtCl_4 was prepared by dissolving K_2PtCl_4 (0.0256 g, Sigma Aldrich) in 300 mL of HPLC water (Fischer Price). The sample of Fe_2O_3 nanoparticles on HOPG was loaded onto a cap with an opening at the center. Through that opening ultraviolet (UV) light can penetrate and photodeposition occurs. The cap was loaded onto a cell facing a 200 W mercury arc lamp. A monochrometer was set at 365 nm and UV light passes through a UV mirror angled at 45 ° with 2 convex lenses that focuses the reflected light to the sample. The sample irradiated by UV light for various times to optimize Pt nanoparticle distribution. After photodeposition, the samples were rinsed with and soaked in HPLC water (Fischer Price), then dried with nitrogen.

Characterization.

Samples of photo-deposited of Pt on Fe_2O_3 nanoparticles were imaged by Scanning Electron Microscopy (SEM) of FEI Magellan 400 XHR at 10 kV. EDS analysis was done at an

accelerating voltage of 15 kV. X-ray Photoelectron Spectroscopy (XPS) measurements were performed with Molecular Environmental Sciences Beamline (Beamline 11.0.2) at the Advanced Light Source synchrotron facility at Lawrence Berkeley National Laboratory. X-rays were produced from the ALS storage ring by a bending magnet. The hemispherical analyzer uses a three stage differentially pumped electrostatic lens system to maintain the UHV environment. The sample was mounted on a sample holder that can be heated and measures accurate temperature by the thermocouple that is mounted on it. The spectra were obtained at a base pressure of 1×10^{-9} Torr. The pass energy of 100 eV and 20 eV were used for survey scans and narrow scans, respectively. Binding energy was calibrated by C1s of HOPG set at 284.6 eV as a reference. For Figure 4.7, photoelectron measurement was performed with ESCALAB MK II surface analysis instrument (VG scientific). This XPS was equipped with a 150 mm hemisphere electron energy analyzer and a twin anode x-ray source (Mg/Al) in a multi-chamber system under ultrahigh vacuum. XPS were performed at a base pressure between 5×10^{-10} and 1×10^{-9} torr using Al Kα with a constant energy of 1486.6 eV and pass every of 20 eV. XPSpeak4.1 and CasaXPS programs were used to deconvolute peaks. Background subtraction was made by subtraction of Shriley-type background from each spectrum.

Transmitted Electron Microscopy (TEM) images were obtained by TEM Philips/FEI CM-20. TEM samples were prepared by obtaining optically transparent areas by cleaving sample surface using an adhesive tape. Optically transparent areas were mounted in a copper TEM grid (Ted Pella, 50/100 double mesh folding copper grid).

Methylene blue Photo-degradation study.

Pt on Fe oxide linear arrays sample was placed in a fluorimeter cuvette cell (International Crystal Laboratories) with about 7 mL of 1 mM of methylene blue (MB) solution (HPLC-grade water).

The fluorimeter cell was covered with a Teflon stopper and para-film was sealed around the stopper and the cell. A monochrometer was set at 365 nm and UV light passes through a UV mirror angled at 45 ° with 2 convex lenses that focuses the reflected light to the sample. A fluorimeter cuvette cell with Pt-Fe oxide sample and MB solution was facing towards the UV light. Every 15 minutes, sample was transferred in an aluminum foiled glass jar for UV-vis spectrum (Cary 50 Photospectrometer). UV-vis spectra was analyzed by averaging highest peak absorption, 666 – 669 nm (λ_{max}) of each spectrum and subtracted from averaged baseline (453 – 455 nm). The peak difference was then converted in concentration. The concentration of MB was monitored over time of UV exposure.

RESULTS AND DISCUSSION

4.1. Photodeposition of Pt on Fe oxide nanoparticle arrays

Linearly ordered Fe oxide NPs deposited on HOPG was placed in a cell with 10 mL of 0.1 mM of Pt solution in HPLC water. UV exposure on these sample resulted in the photodeposition of Pt on Fe oxide NPs. Upon 30 minutes of UV irradiation, Pt NPs in sub-nanometer size were photo-deposited onto Fe oxide NPs. Longer irradiation did not have further effects on Pt particle size suggesting that Fe oxide sites are saturated with 30 minutes of UV exposure at the given concentration (data not shown). Figure 4.1 shows a typical secondary electron SEM image of photo-deposited Pt on Fe oxide NPs that allow us to understand the surface morphology of the sample. In Figure 4.1A and B, brighter spots in 1-2nm in diameter can be seen on Fe oxide NP arrays. The bright spots were confirmed to be Pt particles based on EDS analysis (Figure 4.1C). Aggregated features were observed on the terraces of HOPG yet neither Fe nor Pt was observed in the EDS spectrum. This surface roughness on terrace areas could be due to HOPG surface and water interaction or beam damage during the imaging process. Many attempts were made to obtain SEM images of blank HOPG surface after water exposure yet it was difficult to focus the image due to the lack of particles. It is clear however that Pt NPs were only photo-deposited on Fe oxide NPs upon UV-light exposure.

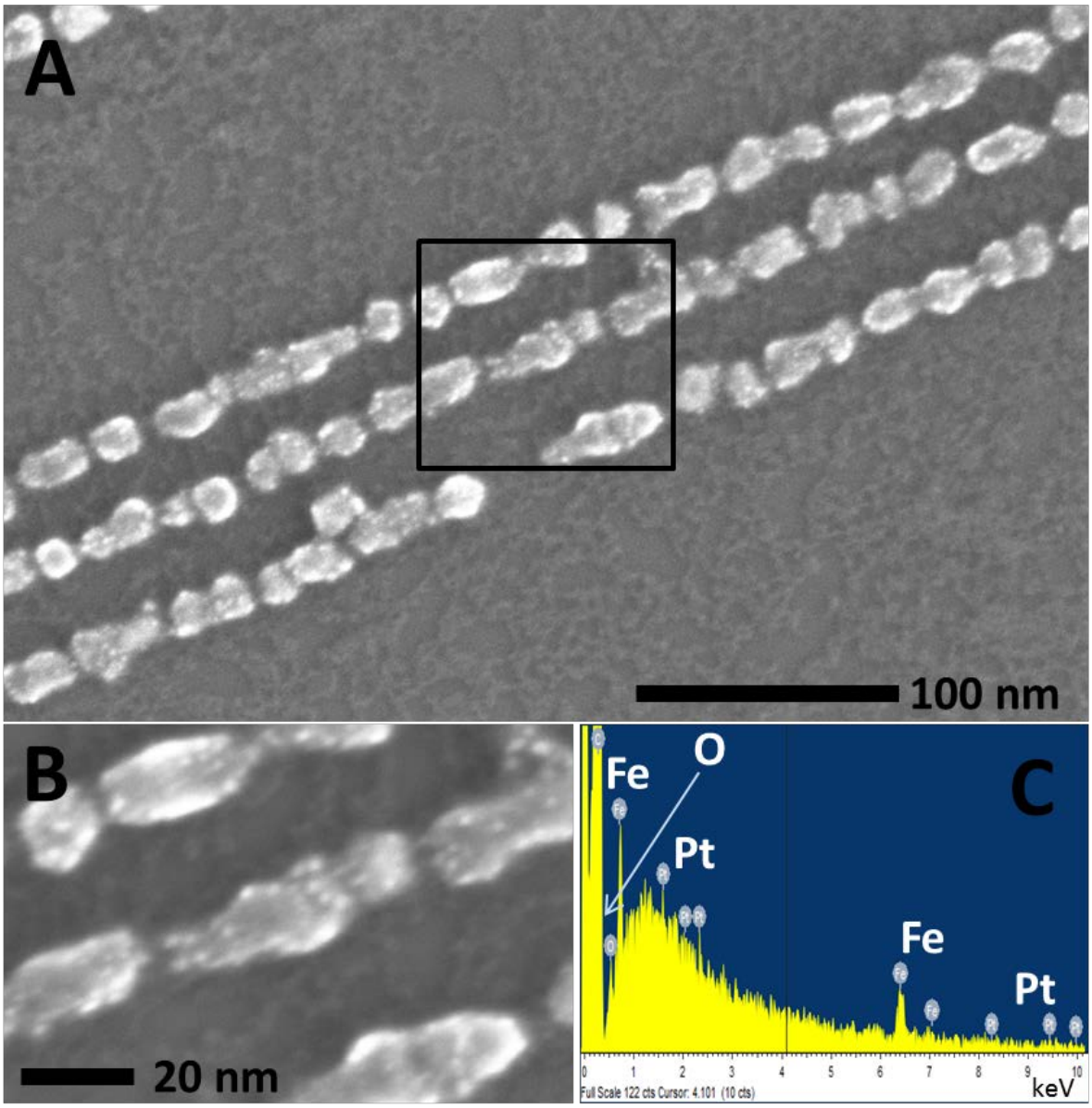

Figure 4.1. SEM images and EDS of Pt NPs on linear arrays of Fe_2O_3 NPs on HOPG. (a) Low-magnification SEM image. (b) High-magnification SEM image of boxed region in A. (c) Energy-dispersive spectra (EDS) of B. Presence of Fe, Pt and O observed.

4.2. Characterization

To characterize the Pt NPs in more detail, TEM analysis was performed. Even at low magnification, it is apparent that the Fe oxide NPs are covered up with smaller dark spots that represent Pt NPs (Figure 4.2A). A high magnification image (Figure 4.2B) shows more detailed information about the Pt NPs. The low resolution made it difficult to accurately measure the Pt NP sizes however, they were roughly in 1-3nm in diameter. With a higher-magnification image shown in Figure 4.2C, an even more detailed analysis was performed. A *d*-spacing of 2.26 Å was measured from the lattice fringes and fast Fourier transform (FFT) in the red and blue box region corresponds to (111) lattice planes of metallic Pt. A lattice resolved TEM image of another location within the same sample is shown in Figure 4.3. In some locations, we measured lattice fringe spacing of 2.26 Å, which index well to (111) planes of metallic Pt. And FFT of red boxed region also corresponds to metallic Pt. However, FFT of blue-boxed region indicates the presence of (100) planes of PtO, and (311) and (111) lattice planes of Fe_3O_4. This may be due to the oxidization of Pt NPs by air exposure and/or by the rinsing process after the photodeposition reaction.

Further insights into the oxidation state of Pt were obtained by synchrotron X-ray photoelectron spectroscopy (Figure 4.4). XPS survey scan showed the presence of Pt, Fe and O and the XPS spectra were fitted by CasaXPS software. The Pt 4f peak is composed of a doublet that is 3.35 eV apart and their intensity ratio is 3:4.[13] The Gaussian shaped $4f_{5/2}$ peak is equal to half-widths of $4f_{7/2}$ peak.[13] The Pt 4f electron spectra of as-prepared sample indicated two main oxidation state of Pt. There are two doublets; one at 72.8 eV/76.2 eV and the other at 74.1 eV/77.4 eV representing Pt (II) and Pt (IV), respectively. Pt (II) species can be such as PtO or $Pt(OH)_2$ and Pt (IV) species can be PtO_2 or $Pt(OH)_4$. It is difficult to identify exact oxygen

terminated groups on Pt NPs although theoretically, exact identification can be determined by comparing O1s spectra and Pt 4f spectra. However, HOPG being the substrate makes it difficult to draw a conclusion because we cannot neglect the presence of oxygen terminated carbon on the substrate where differentiation of oxygen on Pt or HOPG itself cannot be done. However, it is clear that as-prepared sample indicated the presence of Pt oxide and not metallic Pt.

As the sample was heated to 600 °C in ultra-high vacuum (UHV) and the XP spectra was obtained during this annealing process that can cause a change in Pt composition, the fitted Pt 4f spectra actually showed the growth of Pt (0) and a concomitant decrease in Pt (II) species compared to the as-prepared sample. A doublet representing Pt (0) is at 71.8 eV and 75.2 eV. The binding energy for metallic Pt is higher than that are known in literature, 71.2 eV for bulk platinum. This binding energy shift can be due to a decrease in electronic charge density on Pt that can be caused from metal-substrate interaction.[14]

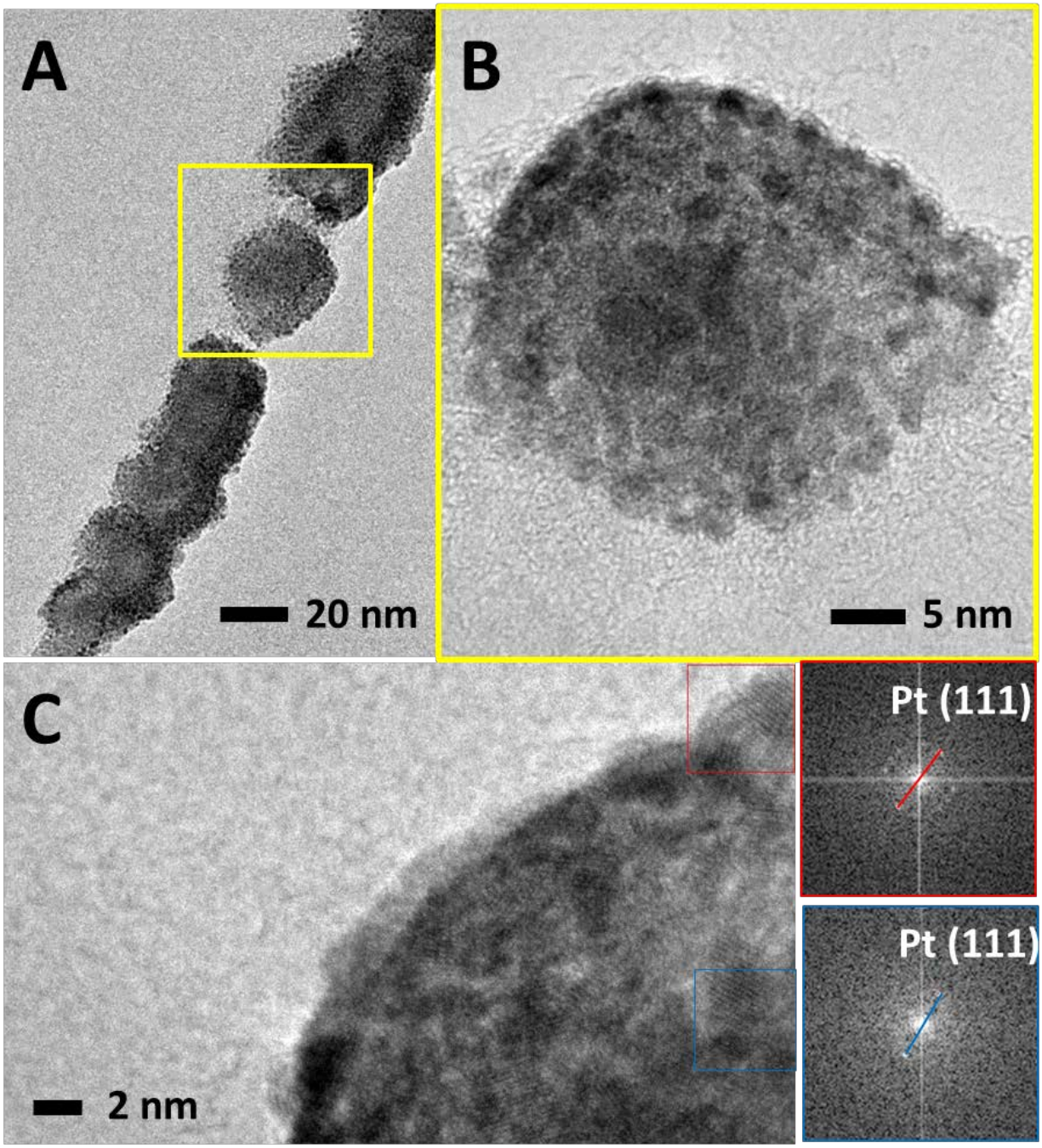

Figure 4.2. TEM image of a Pt on Fe oxide nano arrays. (a) Low-magnification TEM image of one nanocrystal chain. (b) High-magnification TEM image of yellow boxed region in A. (c) Higher-magnification TEM image of B. Fast Fourier Transform (FFT) of boxed region (red and blue) and the measured fringe spacing of 2.26 Å corresponds to Pt (111).

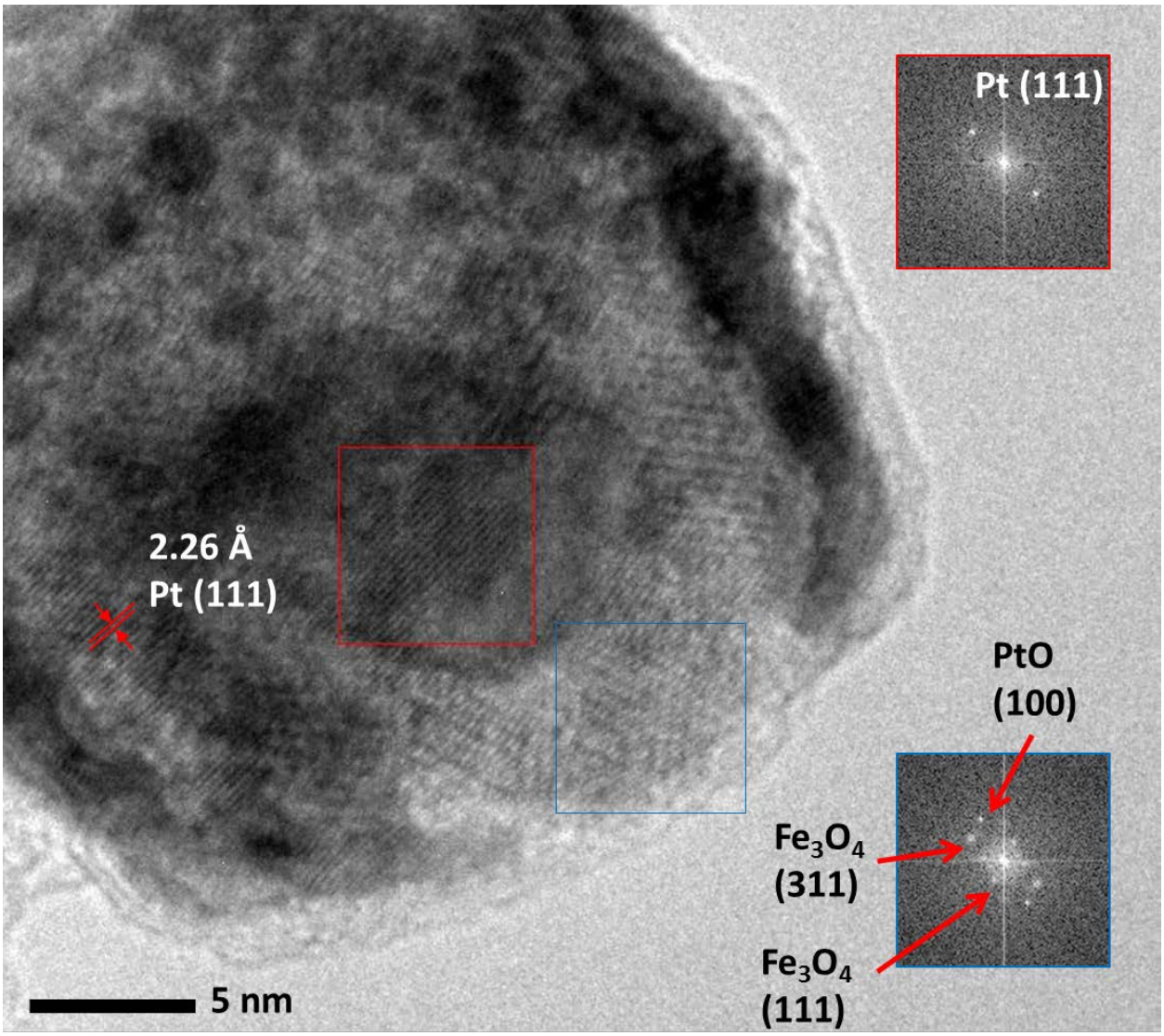

Figure 4.3. Another TEM image of Pt on Fe oxide nano arrays. FFT of blue box region indicates the presence of 2.1 Å, 2.53 Å, and 4.85 Å corresponds to PtO (100), Fe_3O_4 (311), and Fe_3O_4 (111), respectively. FFT of red box region indicates 2.26 Å corresponds to Pt (111). The measured fringe spacing of 2.26 Å corresponds to Pt (111).

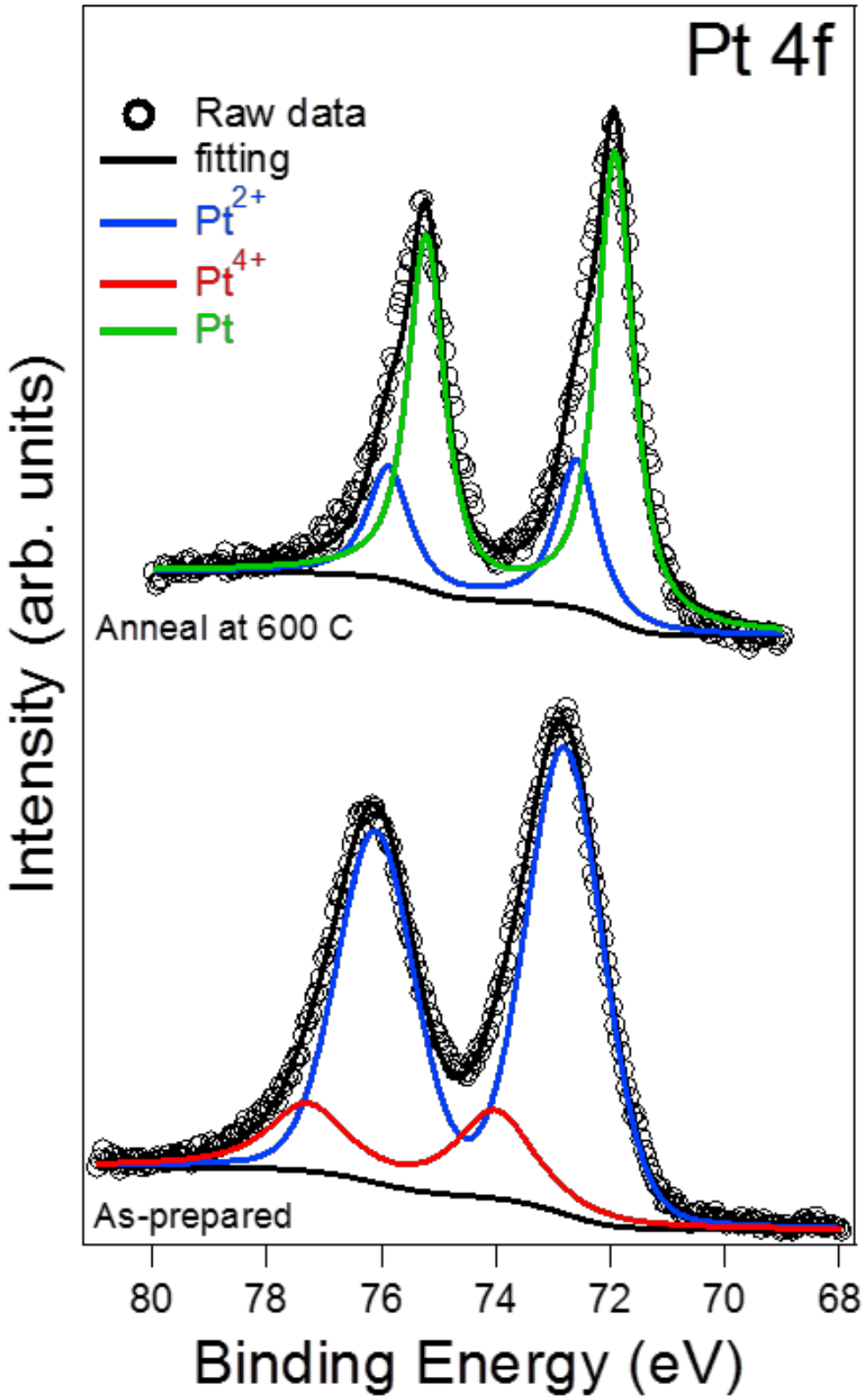

Figure 4.4. Pt 4f XP spectra. The top spectrum was obtained during annealing to 600 °C at UHV. The bottom spectrum was as-prepared sample obtained at room temperature.

4.3 Photocatalytic properties of Pt on Fe oxide by Methylene blue photodegradation studies

The photocatalytic property of Pt NPs can be assessed using Methylene Blue (MB) degradation studies. MB degradation was examined using our Pt NP deposited sample. There are two main peaks associated with MB in the UV spectrum: 609 m and 668 nm (Figure 4.5). UV-vis spectrum was taken with an interval of 15 minutes for the initial 2 hours and then with 30 minutes interval for up to 4 hours. We saw a decrease in MB absorption over reaction time with Pt NPs on Fe oxide NPs (Figure 4.5). For data analysis, the average around 668nm (black arrowed regions) was subtracted by the average regions at 455nm to obtain absolute peak intensity. The absolute peak intensities were then calculated in respect to MB concentration and plotted over reaction time (Figure 4.6 and 4.7)

Figure 4.6 shows the control experiment. MB solution exposed to UV light alone or no UV light had no change in MB concentration. The freshly cleaved HOPG resulted in a minor decrease (0.05mM MB concentration difference) after the 2 hours of UV light exposure. These results suggest that the HOPG alone does not result in non-specific MB degradation and validate the experimental setup. Fe oxide NP arrays on HOPG in MB solution also showed no concentration difference without UV exposure.

Upon UV light exposure to Fe oxide NP arrays, there was a significant MB concentration change (Figure 4.7). On the contrary to our expectation, the photodeposited Pt on Fe oxide NP array sample showed no evidence of enhanced photocatalytic efficiency. This could potentially be due to the oxidation state of Pt on Fe oxide NP arrays. As shown in Figure 4.4, most of the Pt NPs on Fe oxide NPs are in Pt^{2+} or Pt^{4+} state. The inertness of Pt oxide state exhibiting no photocatalytic properties have been shown.[15] Therefore, it was necessary to convert Pt oxide to metallic Pt without perturbing the Fe oxidation state.

Pt oxide can be converted to metallic Pt at above 600 °C under ultra-high vacuum as shown in Figure 4.4. However, annealing at about 600 °C under vacuum caused Fe oxide phase to convert to metallic Fe (Figure 4.8). At 450 °C annealing temperature however, the oxidation state of Fe did not change. It was known from our previous synchrotron XPS experiments on Pt on TiO_2 NPs that Pt oxide converts to metallic Pt at above 300 °C.[16] Based on this fact, we annealed photodeposited Pt on Fe oxide NPs to 380 °C for 10 minutes in the evaporator (base pressure of 5×10^{-7} Torr). Instantly after cooling it to room temperature under vacuum, the sample was transferred to the XPS chamber. Figure 4.9 is Pt 4f XP spectrum after annealing to 380 °C. Although the resolution was low, the deconvolution of peaks showed that there were two doublets; one at 71.6 eV/75.0 eV and the other at 72.8 eV/76.2 eV representing Pt (0) and Pt (II), respectively. Although the transfer time was readily quick, the sample was still exposed in ambient air, which could be sufficient time to oxidize some of the metallic Pt NPs. This could be the source of the observed Pt (II). Importantly, MB photo-degradation study on the metallic Pt converted annealed sample showed a mark decrease in MB concentration over UV exposure exceeding that of the Fe oxide NP array sample.

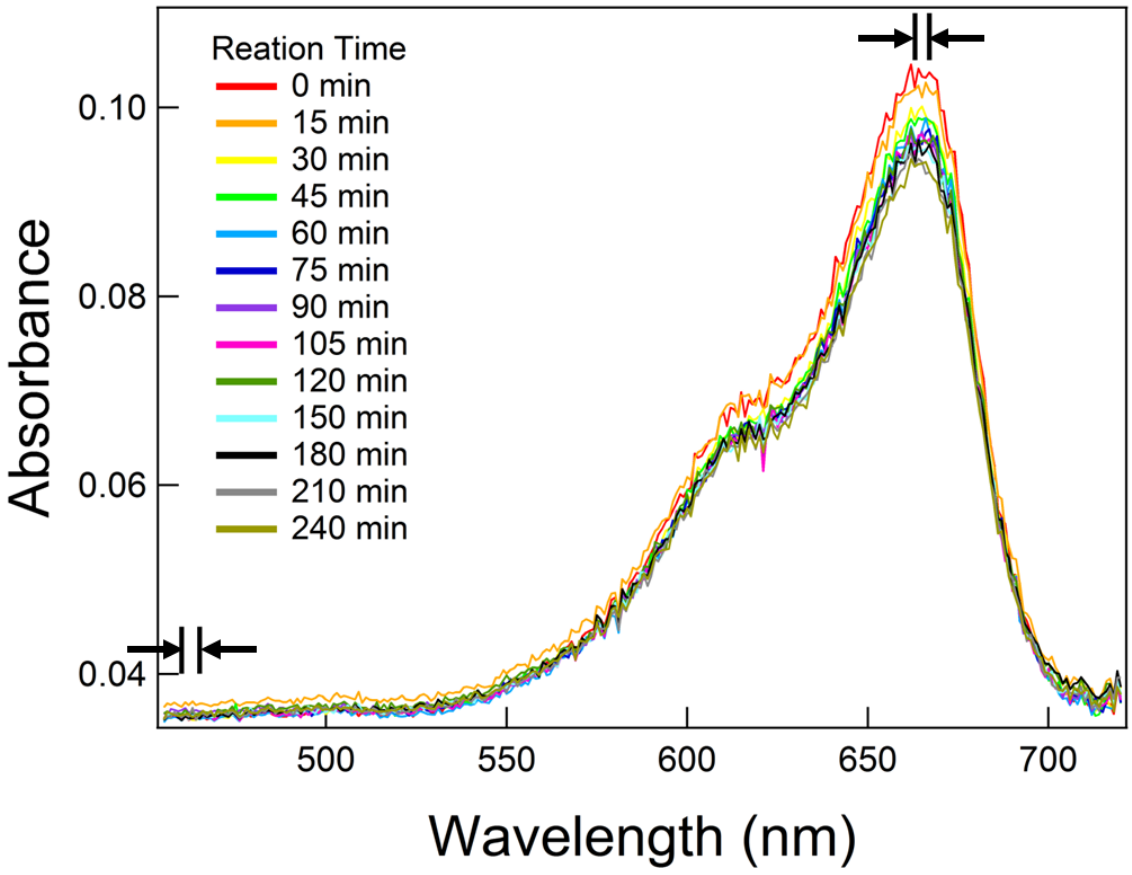

Figure 4.5. UV-vis spectral changes of Methylene blue degradation as a function of UV irradiation time on Pt NP on Fe oxide NP arrays of sample from Figure 5.1. Black arrows indicate the region where highest peak absorption and baseline was averaged to obtain the absolute peak intensity.

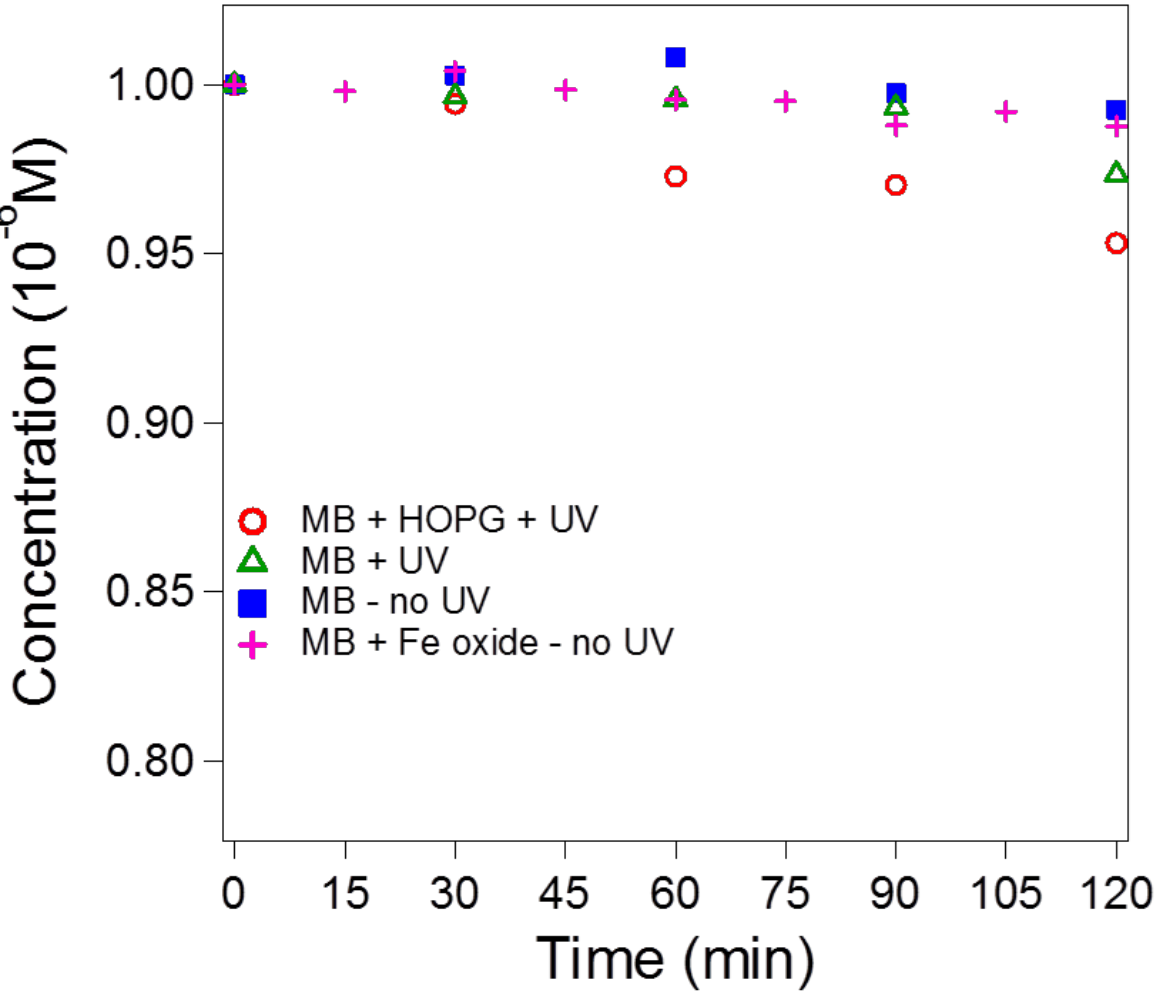

Figure 4.6. Plot of MB concentration changes over UV irradiation time. Control experiments of methylene blue solution (1 mM) degradation over UV exposure: on a blank HOPG (red circle), methylene blue by itself over UV (green triangle) and without UV exposure (blue square), linear arrays of Fe oxide nanoparticles on HOPG without UV exposure (pink cross).

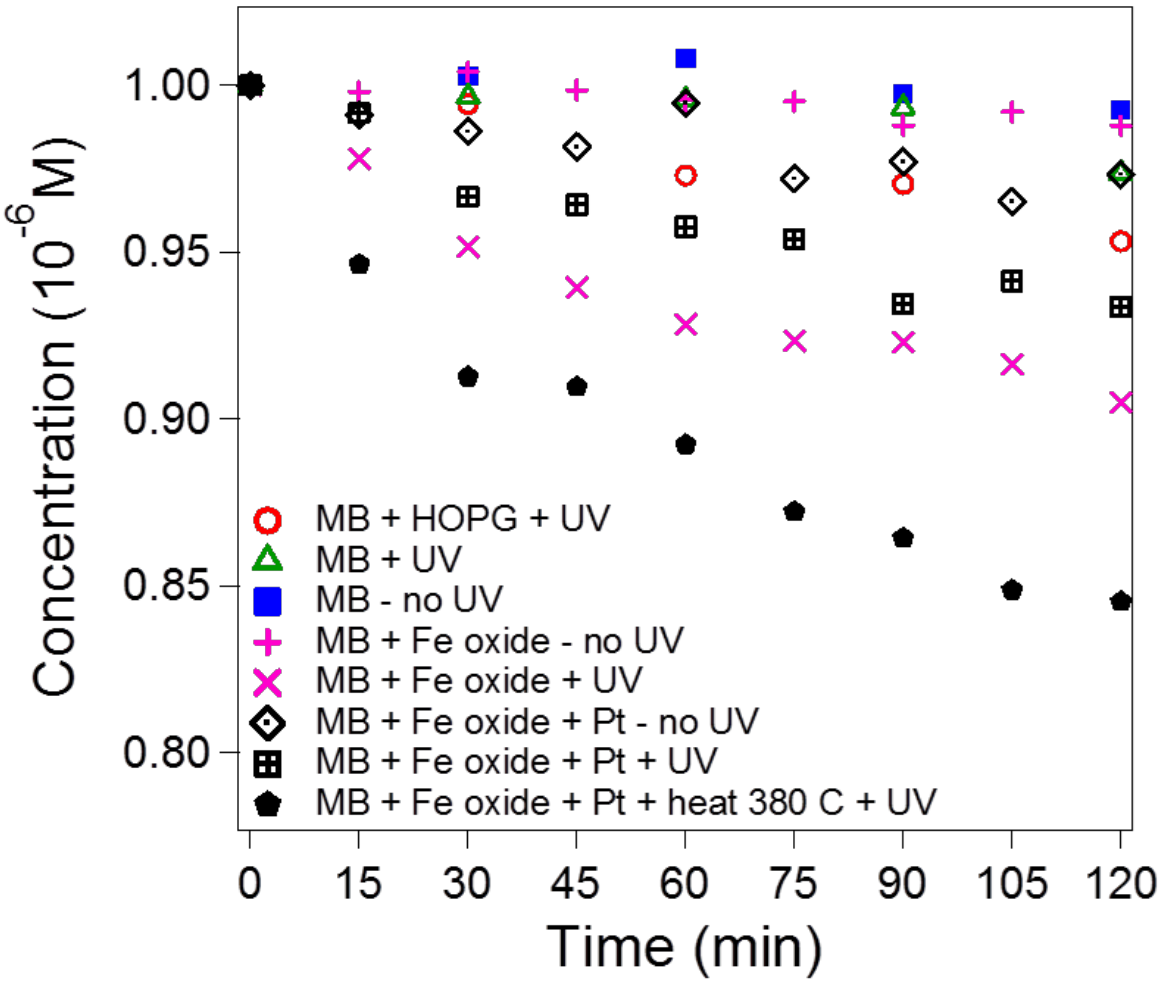

Figure 4.7. Plot of MB concentration changes over UV irradiation time. Methylene blue solution (1 mM) degradation over UV exposure on: a blank HOPG (red circle), methylene blue by itself over UV (green triangle) and without UV exposure (blue square), linear arrays of Fe oxide nanoparticles on HOPG without UV exposure (pink cross), linearly ordered Fe oxide nanoparticle arrays on HOPG with UV (pink X), Pt on Fe oxide nano-arrays without UV (black diamond) and with UV (black square with cross inside), Annealed Pt on Fe oxide nanoparticles with UV (black pentagon).

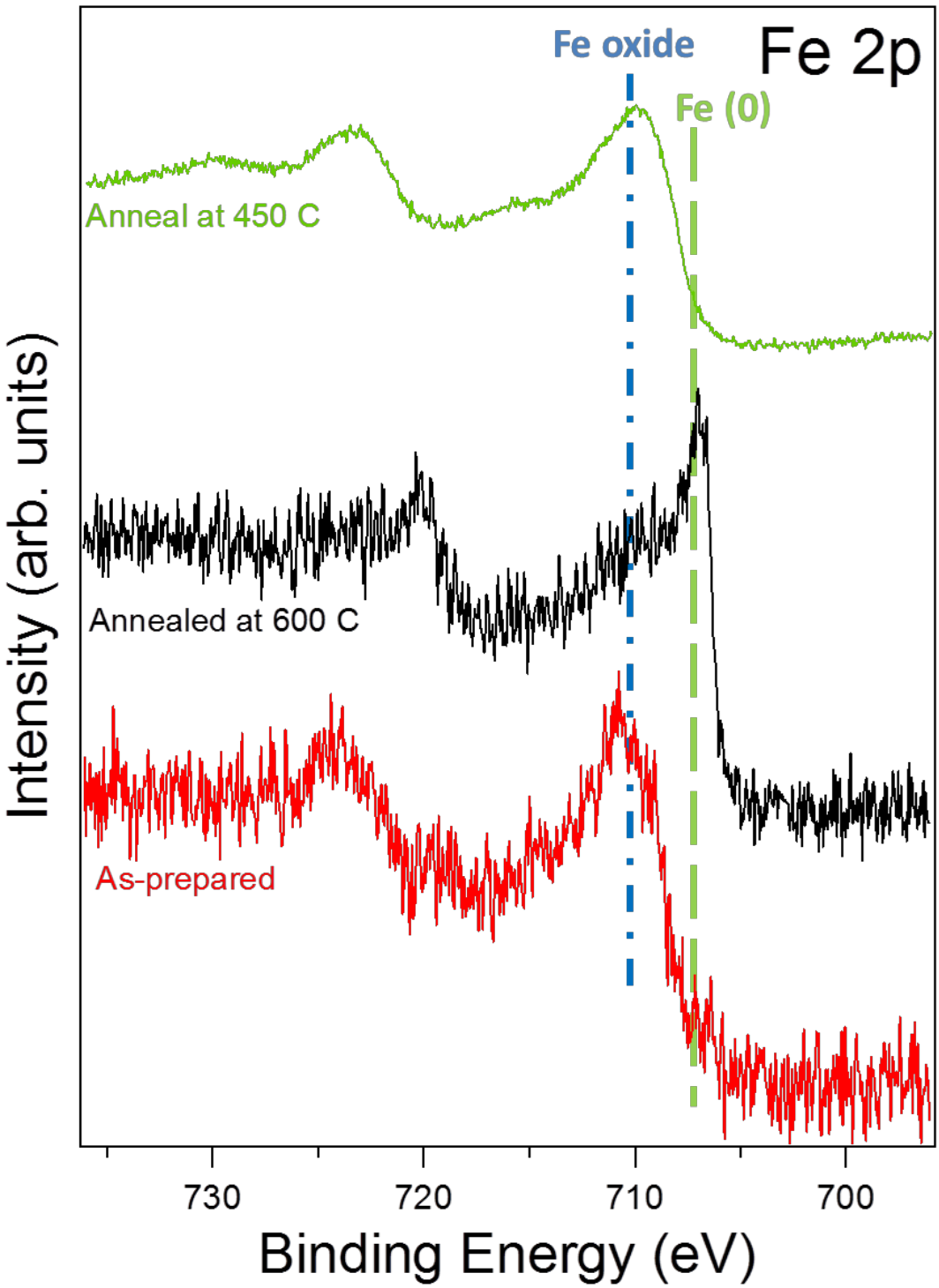

Figure 4.8. Fe 2p XP spectra obtained from synchrotron XPS (Beamline 11.0.2.) Red and black spectra were taken from the same sample. Red line represents as-prepared Pt on Fe oxide NP array sample. Black line was obtained when sample was annealed to 600 °C. Green line spectrum represents Fe oxide on plasma treated HOPG. Green line spectrum was collected at around 450 °C.

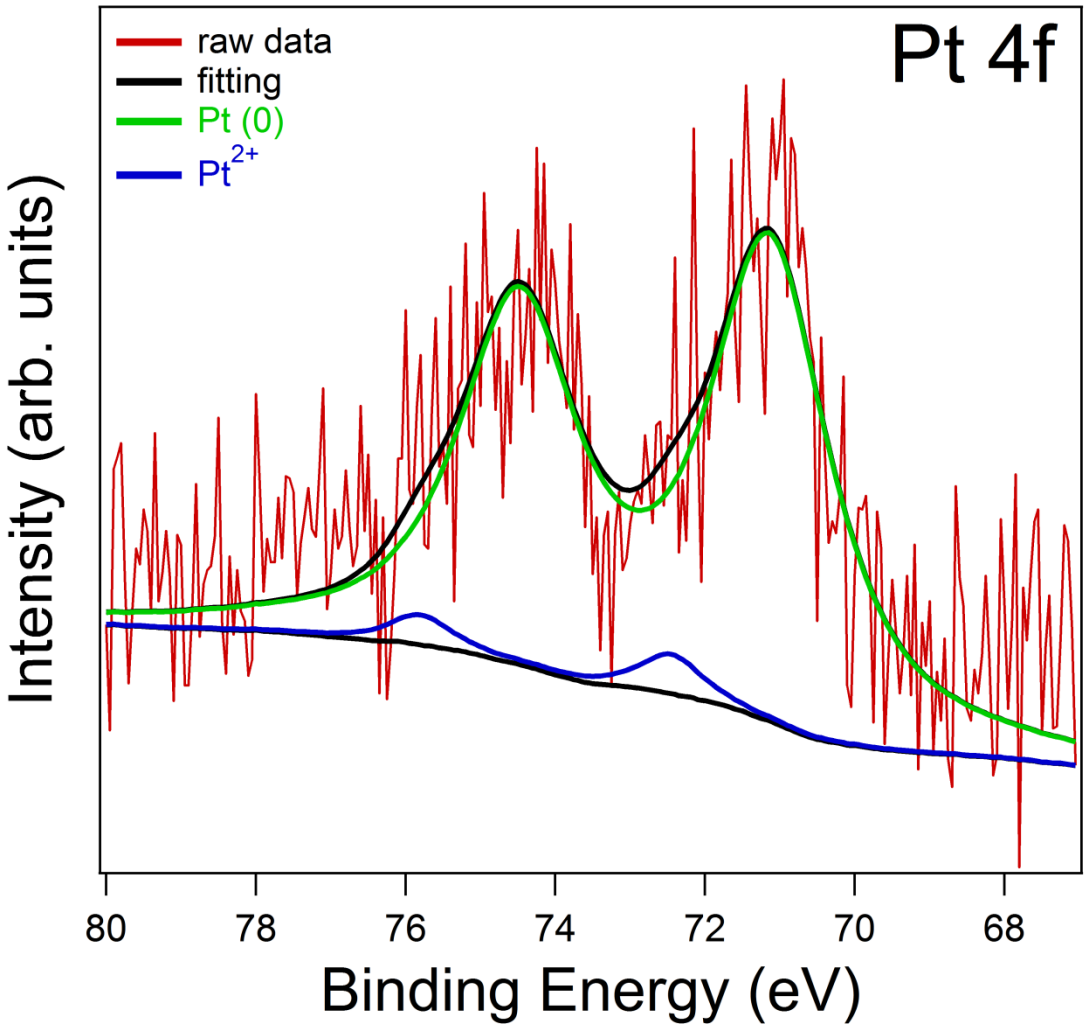

Figure 4.9. Pt 4f XP spectra obtained from ESCALAB MK II surface analysis instrument (VG scientific) after annealing at 380 °C for 10 minutes.

CONCLUSION

In this chapter, Pt NPs were successfully photodeposited on linearly ordered Fe oxide NP arrays. Its photocatalytic properties were examined by MB degradation studies under UV exposure. It was shown from this chapter that Fe oxide NPs exhibit photocatalytic properties to a certain degree. Importantly, Pt NPs on Fe oxide NP arrays exhibited enhancement in its photocatalytic ability when the nature of the deposited Pt oxide NPs were converted to metallic Pt. As-prepared sample showed no enhanced effect on the photo-degradation of MB compared to Fe oxide NPs alone. These results suggest that photodeposited Pt NPs on Fe oxide NP arrays can be a useful tool to study fundamental aspects of photocatalytic activity, a feature important for the aforementioned applications.

REFERENCES

1. Kamat, P. V., Meeting the clean energy demand: nanostructure architectures for solar energy conversion. *J. Phys. Chem. C* **2007,** *111* (7), 2834-2860.
2. Michalet, X.; Pinaud, F. F.; Bentolila, L. A., Quantum dots for live cells in vivo imging, and diagnostics. *Science* **2005,** *307* (5709), 538-544.
3. Wang, C.; Daimon, H.; Sun, S., Dumbbell-like Pt-Fe_3O_4 Nanoparticles and Their Enhanced Ctalysis for Oxygen Reduction Reaction. *Nano Lett.* **2009,** *9* (4), 1493-1496.
4. Chueh, Y. L.; Lai, M. W.; Liang, J. Q.; Chou, L. J.; Wang, Z. L., Systematic Study of Gowth of Aligned Arrays of a-Fe_2O_3 and Fe_3O_4 Nanowires by a Vapor-Solid Process. *Adv. Funct. Mater.* **2006,** *16*, 2243-2251.
5. Qiao, B.; Wang, A.; Yang, X.; Allard, L.; Jiang, Z.; Cui, Y.; Liu, J.; Li, J.; Zhang, T., Single-atom catalysis of CO oxidation using Pt_1/FeO_x. *Nat. Chem.* **2011,** *3*, 634-641.
6. Lei, Y.; Mehmood, F.; Lee, S.; Greeley, J.; Lee, B.; Seifert, S.; Winans, R. E.; Elam, J. W.; Meyer, R. J.; Redfern, P. C.; Teschner, D.; Schlogl, R.; Pellin, M. J.; Curtiss, L. A.; Vajda, S., Increased silver activity for direct propylene epoxidation via subnanometer size effects. *Science* **2010,** *328*, 224-228.
7. Remediakis, I. N.; Lopez, N.; Norskov, J. K., CO oxidation on rutile-supported Au nanoparticles. *Angew. Chem. Int. Ed.* **2005,** *44*, 1824-1826.
8. Duchesne, P. N.; GChen, G.; Zheng, N.; Zhang, P., Local Structure, Electronic Behavior, and Electrocatalytic Reactivity of CO-Reduced Platinum-Iron Oxide Nanoparticles. *J. Phys. Chem. C* **2013,** *117*, 26324-26333.
9. Liu, X.; Korotkikh, O.; Farrauto, R., Selective catlytic oxidation of CO in H_2: structural study of Fe oxide-promoted Pt/alumina catalyst. *Applied Catalysis A: General* **2002,** *226*, 293-303.
10. LIu, Y.; Zhou, J.; Gong, J.; Wu, W.; Boa, N.; Pan, Z.; Gu, H., The investigation of electrochemical properties for Fe_3O_4@Pt nanocomposites and an enhancement sensing for nitrite. *Electrochimica Acta* **2013,** *111*, 876-887.
11. Qin, Z.; Lewandowski, M.; Sun, Y.-N.; Shaikhutdinov, S.; Freund, H.-J., Encapsulation of Pt Nanoparticles as a Result of Strong Metal-Support Interaction with Fe_3O_4 (111). *J. Phys. Chem. C* **2008,** *112*, 10209-10213.
12. Hu, Y.; Kleiman-Shwarsctein, A.; Forman, A.; Hazen, D.; Park, J.; McFarland, E., Pt-Doped a-Fe_2O_3 Thin Films Active for PHotoelectrochemical Water Splitting. *Chem. Mater.* **2008,** *20*, 3803-3805.
13. Sen, F.; Gokagac, G., Different Sized Platinum Nanoparticles Supported on Carbon: An XPS Study on These Methanol Oxidation Catalysts. *J. Phys. Chem. C* **2007,** *111*, 5715-5720.
14. Gokagac, G.; Kennedy, B. J., Carbon Supported Pt+Os Catalysts for Methanol Oxidation. *Z. Naturforsch* **2002,** *57b*, 193-201.
15. Pedersen, T. M.; Li, W. X.; Hammer, B., Structure and activity of oxidized Pt(110) and a-PtO_2. *Phys. Chem. Chem. Phys.* **2006,** *8*, 1566-1574.
16. Liu, Y.; Taing, J.; Reyes, P.; Chen, C.-C.; Blulm, H.; Liu, Z.; van Veenendaal, M.; Devereaux, T. P.; Hemminger, J. C., Nanoscale Metal-Support Catalysis System by Functionalizing Isolated TiO_2 Nanoparticles with Pt Photodeposition. *in preparation*.

CHAPTER 5

Fe oxide Nanoparticle Growth on Oxygen Plasma Treated HOPG Surface

INTRODUCTION

As mentioned in chapter 1, HOPG has been used as a substrate due to its ordered structures with strong σ-bond along the basal lines (terraces) and relatively weak interlayer forces. Due to the stacking faults, there are naturally created defect sites known as step edges. In chapter 1, we successfully deposited Fe NPs specifically along the step edges. It is a great privilege to have ordered NP arrays for theoretical calculations; however, low metal density on the surface prevents detection limits for NP characterization. It is known that carbon on HOPG reacts with various gases such as O_2, NO, H_2O, and CO_2[1,2,3] where the reaction between carbon and oxygen is temperature dependent. Thermally heated HOPG at above 700 °C in oxygen results in an oxidation reaction mainly initiated at the defect sites, due to unoccupied sp^2 orbitals. Further reaction results in creating new vacancies in the basal plane of HOPG and these vacancies can expand to monolayer etch pits.[1] Plasma treatment, on the other hand, is known to create more or less circular shape vacancies over the terraces.[3] 10 minutes of plasma exposure at oxygen pressure of 1.0 mbar at a power of 100 W have been shown to create defects that are 20 to 80 nm in diameter and heights of 0.3 to 8.8 nm.[3]

In an attempt to improve the detection limits for NP characterization, here in this chapter we exposed HOPG with oxygen plasma to create more defect sites and study how the surface modification affects Fe NP growth. We varied 4 different parameters to obtain optimal NP morphological distribution. We have varied the substrate temperature upon deposition, oxygen

plasma power, deposition rate, and post-annealing condition. The results suggest that the substrate temperature, plasma power and deposition rate affect the size of Fe NPs. We also note that unlike Fe NP arrays on freshly cleaved HOPG, changes in post-annealing conditions can affect the Fe NP morphology on oxygen plasma treated HOPG.

EXPERIMENTAL

Highly Oriented Pyrolytic Graphite (HOPG). 12 mm × 12 mm × 2 mm pieces of HOPG with a mosaic spread of 0.8 ° ± 0.2 ° (Grade ZYB, Momentive Performance) were used. Surface of HOPG was cleaved using Scotch tape in air to expose fresh surface and immediately transferred to oxygen plasma cleaner (Diener Model ZEPTO). Once sample was loaded at the back of the glass tray, the chamber was quickly pumped down to 2×10^{-3} mbar. Once O_2 (99.993%,Airgas) pressure was set to 0.4 mbar, plasma is ignited via a 13.56 MHz (0 - 50 W) single electrode high frequency generator. And increase the setting O_2 pressure to 1 mbar. Plasma was ignited for 10 minutes. Then the sample is quickly transferred to the evaporator.

Physical Vapor Deposition. Physical Vapor Deposition (PVD) in an Edwards 306A thermal evaporation coating was used to deposit Fe on oxygen plasma treated HOPG. The sample was placed in a Molybdenum sample holder. A K-type thermocouple was placed on top of HOPG and a Macor piece was mounted in between Molybdenum sample holder and HOPG. This allowed us to directly measure HOPG temperature. Prior to Fe deposition, HOPG was slowly increased to 600 °C with base pressure below $5 \times 10^{-6-}$ torr for over 3 hours to desorb water and remove any organic residues on the surface. The ceramic crucible holding iron shots were resistively heated at ~12 amps. Deposition thickness was measured by a quartz crystal microbalance, INFICON front load single crystal sensor. The sample was quickly cooled down to room temperature after deposition.

Characterization. Scanning Electron Microscopy (SEM) of FEI Magellan 400 XHR at 10 kV were used to image each samples after iron oxide deposition. EDS (Oxford Instruments) analysis was done by using a silicon drift detector at an accelerating voltage of 15 kV. X-ray Photoelectron Spectroscopy (XPS) measurements were performed with Molecular

Environmental Sciences Beamline (Beamline 11.0.2) at the Advanced Light Source synchrotron facility at Lawrence Berkeley National Laboratory. X-rays were produced from the ALS storage ring by a bending magnet. The hemispherical analyzer uses a three stage differentially pumped electrostatic lens system to maintain the UHV environment. The sample was mounted on a sample holder that can be heated and measures accurate temperature by the thermocouple that is mounted on it. The spectra were obtained at a base pressure of 1×10^{-9} Torr. The pass energy of 100 eV and 20 eV were used for survey scans and narrow scans, respectively. Binding energy was calibrated by C1s of HOPG set at 284.6 eV as a reference. XPSPeak 4.1 and CasaXPS were used to deconvolute background. ImageJ was used to measure the iron oxide nanocrystal size and its spacing.

RESULTS AND DISCUSSION

5.1 Varying Substrate Temperature

Fe was deposited on HOPG that was previously treated by oxygen plasma. A freshly cleaved HOPG contains naturally occurring step edges. As mentioned in chapter 1, HOPG held at above 475 °C enhances the nucleation along the step edges. However, during the oxygen plasma cleaning process, a reaction between oxygen and the carbon on HOPG can happen that creates new defect sites on the surface. Presumably, these defect sites destroyed the step edges and no linearly ordered NPs could be observed (see Figures). These defect sites have been reported to be around 9 Å in heights.[3] Although pure Fe shots were evaporated onto the plasma cleaned HOPG, air exposure after deposition for further characterization suggests that the NPs are in Fe oxide phases.

We observed that varying the substrate temperature affected Fe NP morphology and size. Figure 5.1 shows SEM images of uniform thickness of 2 nm of Fe deposited on oxygen plasma treated HOPG that was held at 600 °C. A low-magnification SEM image (Figure 5.1 top), shows high density of Fe deposited on the surface. These particles were in a range of 5 to 100 nm in diameter. We also observed larger NPs with irregular shape (50-100 nm wide and 25-40 nm on the shorter side). The gaps between these particles could vary from as close as 3 nm to hundreds of nm apart. A high-magnification SEM image (Figure 5.1 bottom), shows additional morphological information about the Fe oxide NPs where most of the particles had facetted edges and were quite crystalline.

To quantitate the results, ImageJ was used to roughly estimate particle size. A histogram was generated from the low magnification image where it shows the particles were mainly in between 10-30 nm in length. It is interesting to note that gaps between particles correlated to the

size of the particles; the smaller the particle size, the shorter the gaps between the particles. This suggests that upon annealing after deposition, particles might agglomerate and form bigger particles.

Fe deposited at 700 °C shows different results to that of 600 °C (Figure 5.3). A low-magnification image on Figure 5.3 (top) shows two different NP sizes. The majority of NPs were approximately 10 nm in size. Large NPs were in the range of 50-70 nm. The gaps between each particles are smaller than that of Figure 5.1. This was due to an increase in the number of smaller NPs on the surface. Interestingly, trails were found around the larger NPs that may be results of Oswald ripening where smaller particles can diffuse to the large particle.

During annealing process, NPs were too close to each other that 700 °C was sufficiently enough temperature to agglomerate nanoparticles. This Osward ripening effect is shown in Figure 5.11, where there was no post-annealing involved.

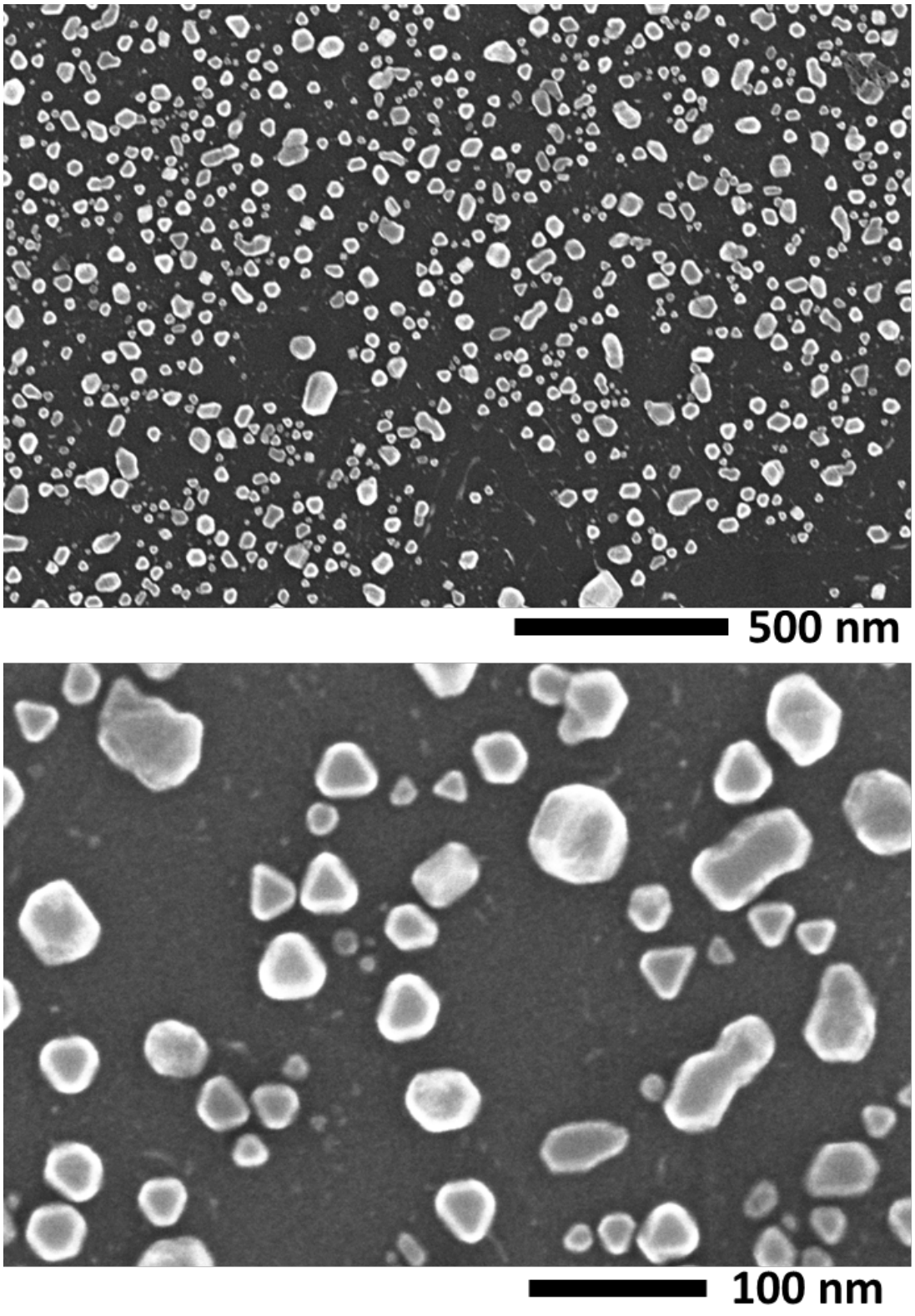

Figure 5.1. SEM images of 2 nm of Fe deposited on oxygen plasma treated (50 W, 1 mbar) HOPG at 600 °C followed by 3 hours of post-annealing at same temperature. (top) Low magnification SEM image. (bottom) high magnification SEM image.

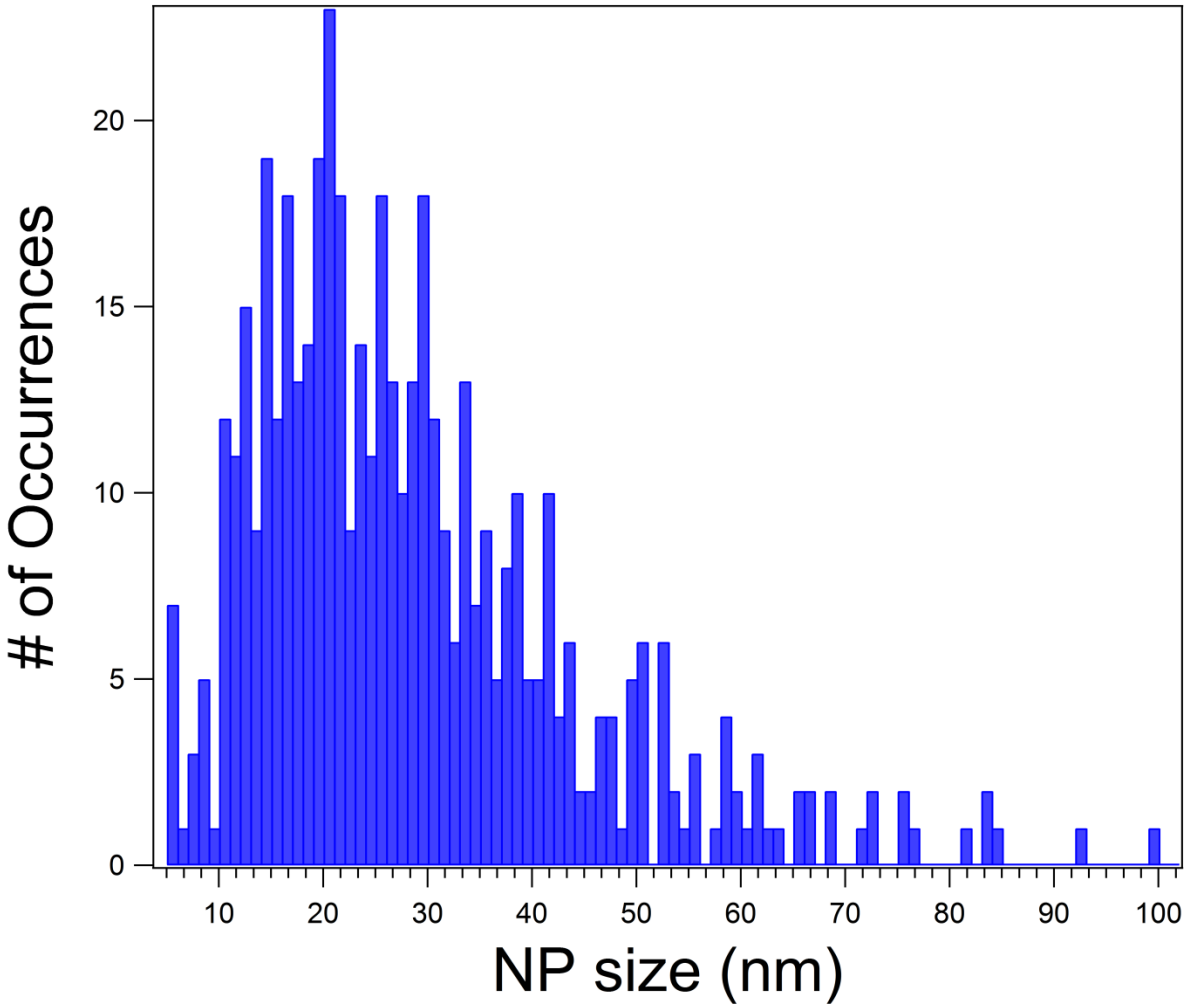

Figure 5.2. Histogram generated from SEM image in Figure 5.1 top. A high density of particles is in the range of 5-6 nm. And some particles are as big as 131 nm in length.

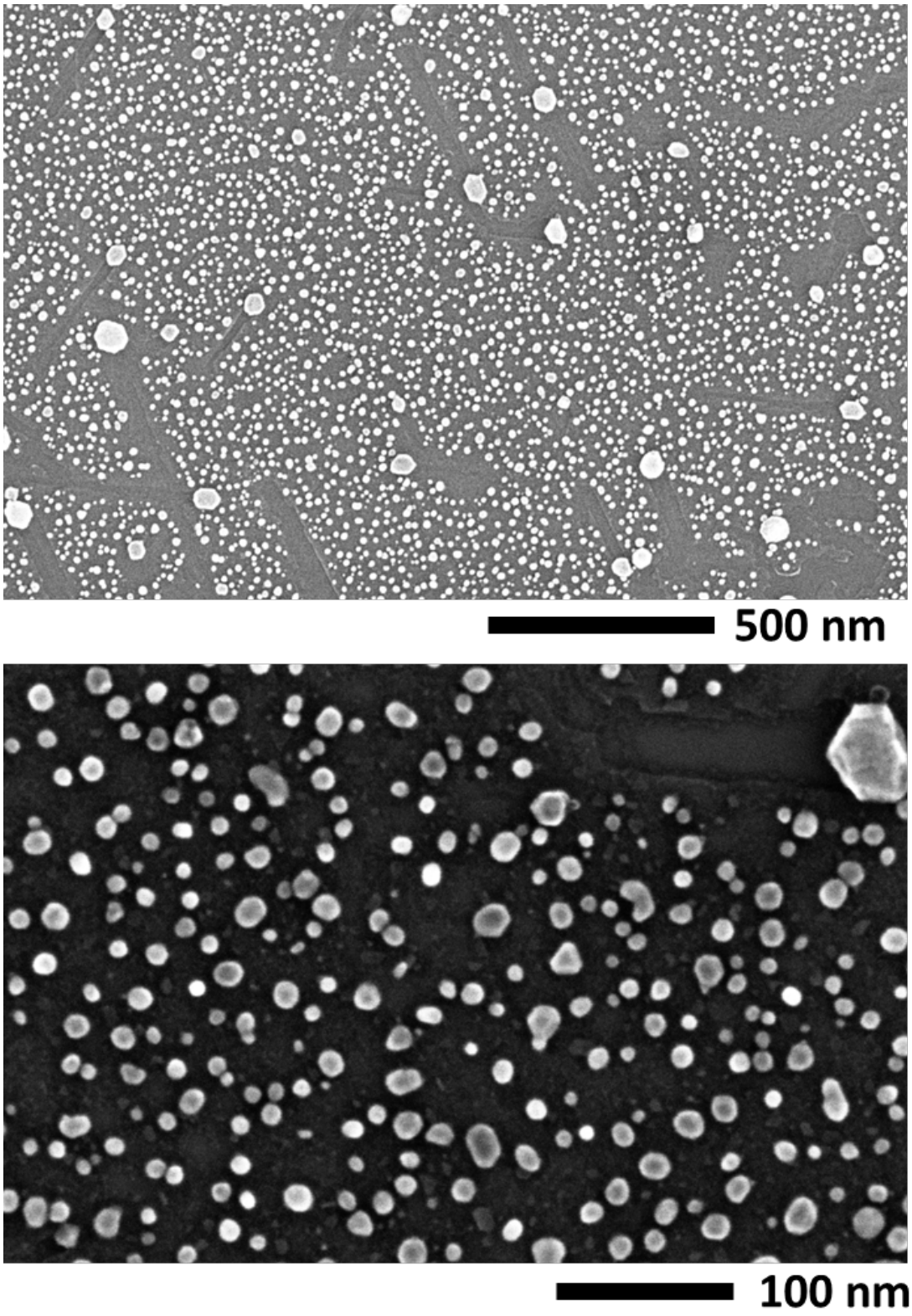

Figure 5.3. SEM images of 2 nm of Fe deposited on oxygen plasma treated (50 W, 1 mbar) HOPG at 700 °C followed by 3 hours of post-annealing at same temperature. (a) Low-magnification SEM image. (b) high-magnification SEM image.

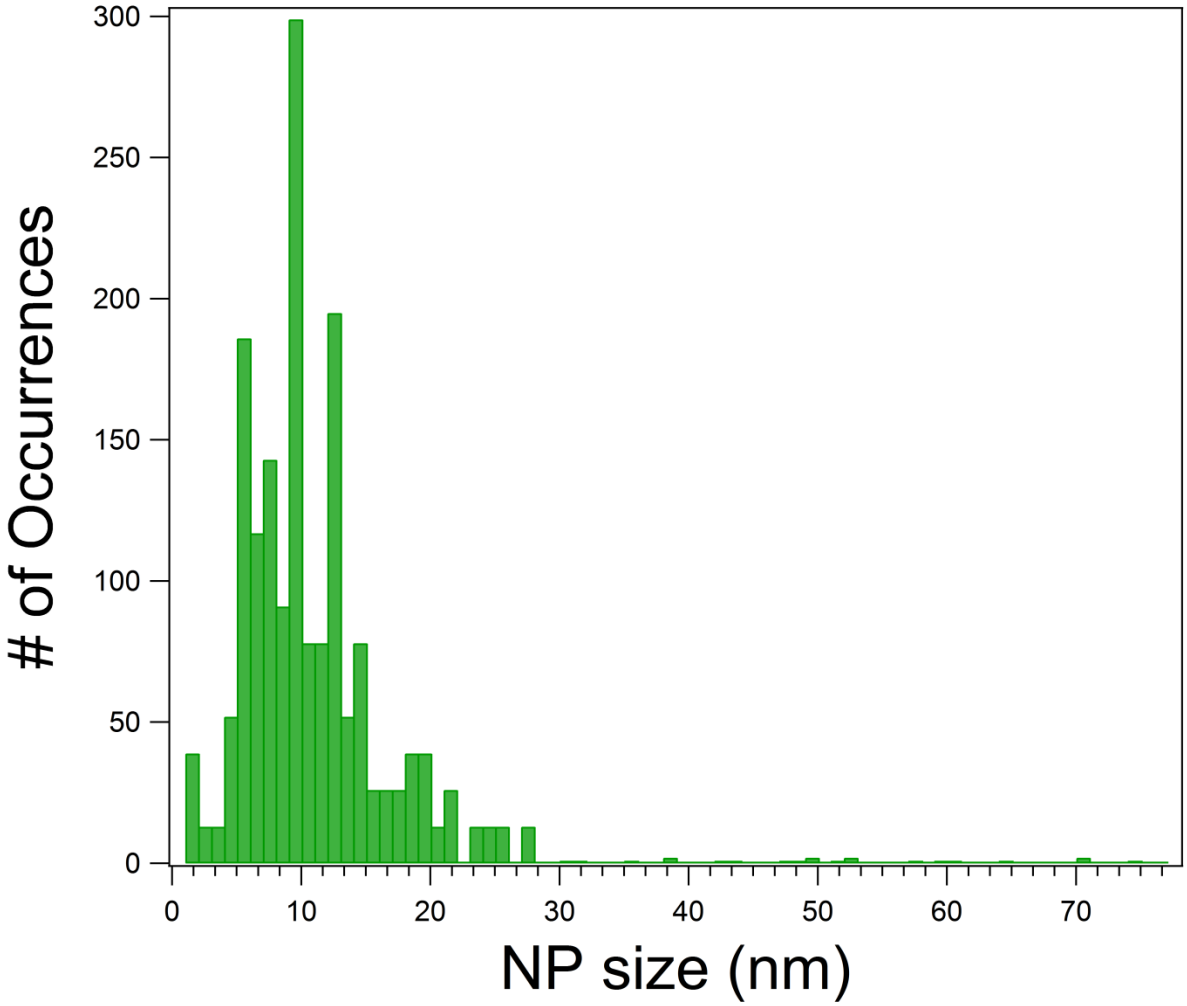

Figure 5.4. Histogram generated from SEM image in Figure 5.3A. A high density of particles is in the range of 10-20 nm. And some particles are as big as 94 nm in length.

5.2 Varying Plasma power

It is difficult to image defect sites created on the surface of HOPG after plasma treatment because the hydrocarbons are too mobile. However, it has been shown that defect sites that created from 100W, 200 mTorr of O_2 are in the range of 0.3 - 8.8 nm in depth.[3] We therefore varied plasma power and deposited Fe to observe differences in particle size. Figure 5.5 and 5.6 represent Fe deposition on HOPG that was oxygen plasma treated at 1mbar and 0.4mbar for 10 minutes, respectively. Same amount of Fe was deposited on both of samples at 600 °C. It is obvious from SEM images that lower oxygen pressure resulted in smaller particle distributions. The lower oxygen pressure results in the creation of smaller defects on the HOPG surface. The higher amount of oxygen molecules in the high oxygen pressure condition can presumably react more with the HOPG surface leaving either larger defect sites or increased amounts of small defect sites could become one larger defect site. As mentioned in section 5.1, not all the NPs are in the same size range. As seen in high-magnification SEM images from Figure 5.4, there are particles that are in tens of nm in size. These NPs are again due to the annealing process during fabrications which is mentioned in section 5.11.

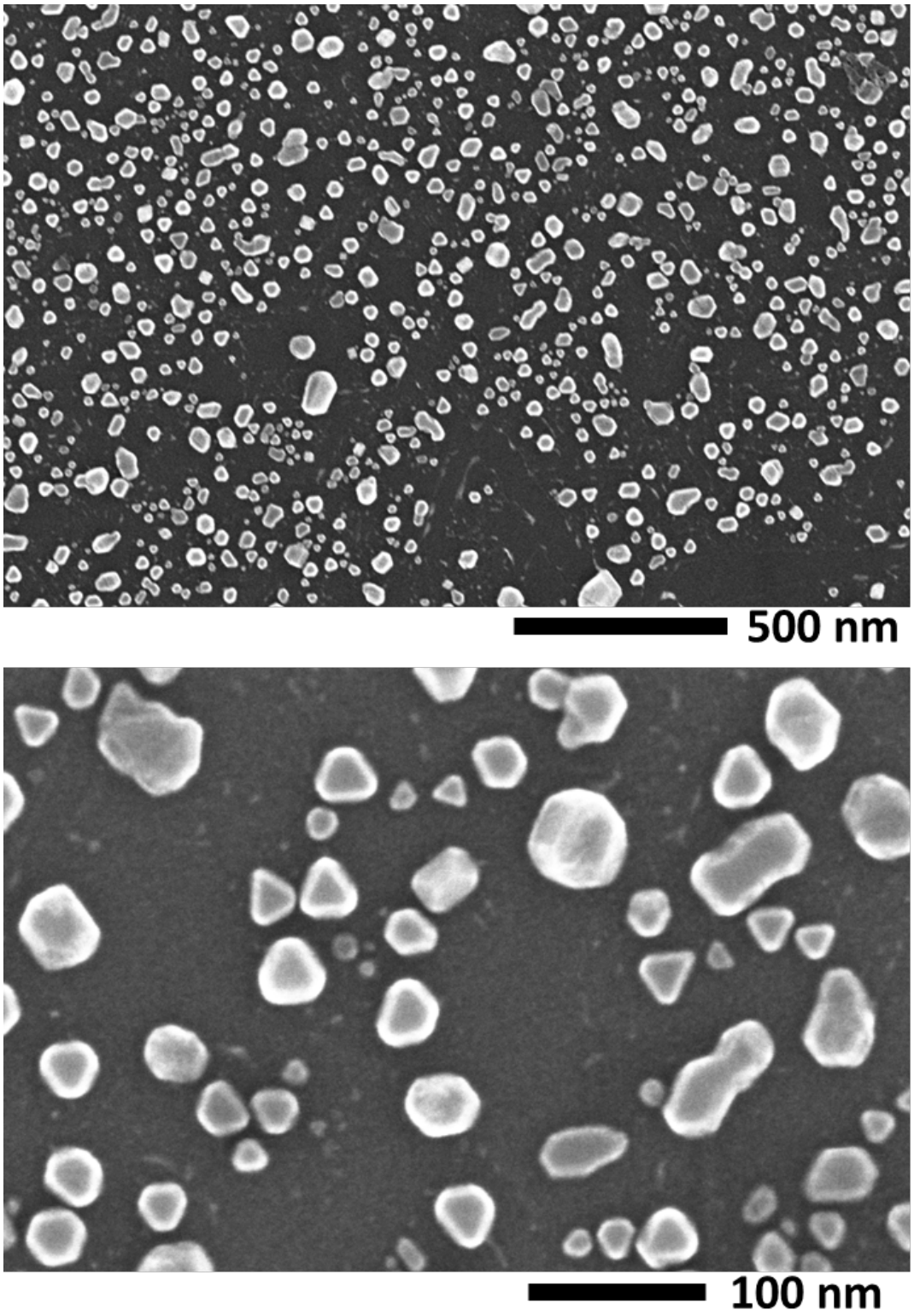

Figure 5.5. SEM images of 2 nm of Fe deposited at 600 °C on different O_2 pressure HOPG at different temperature. (top) Low-magnification SEM image of Fe deposited on HOPG that was treated with 1 mbar of O_2 pressure for 10 minutes. (bottom) High-magnification SEM image.

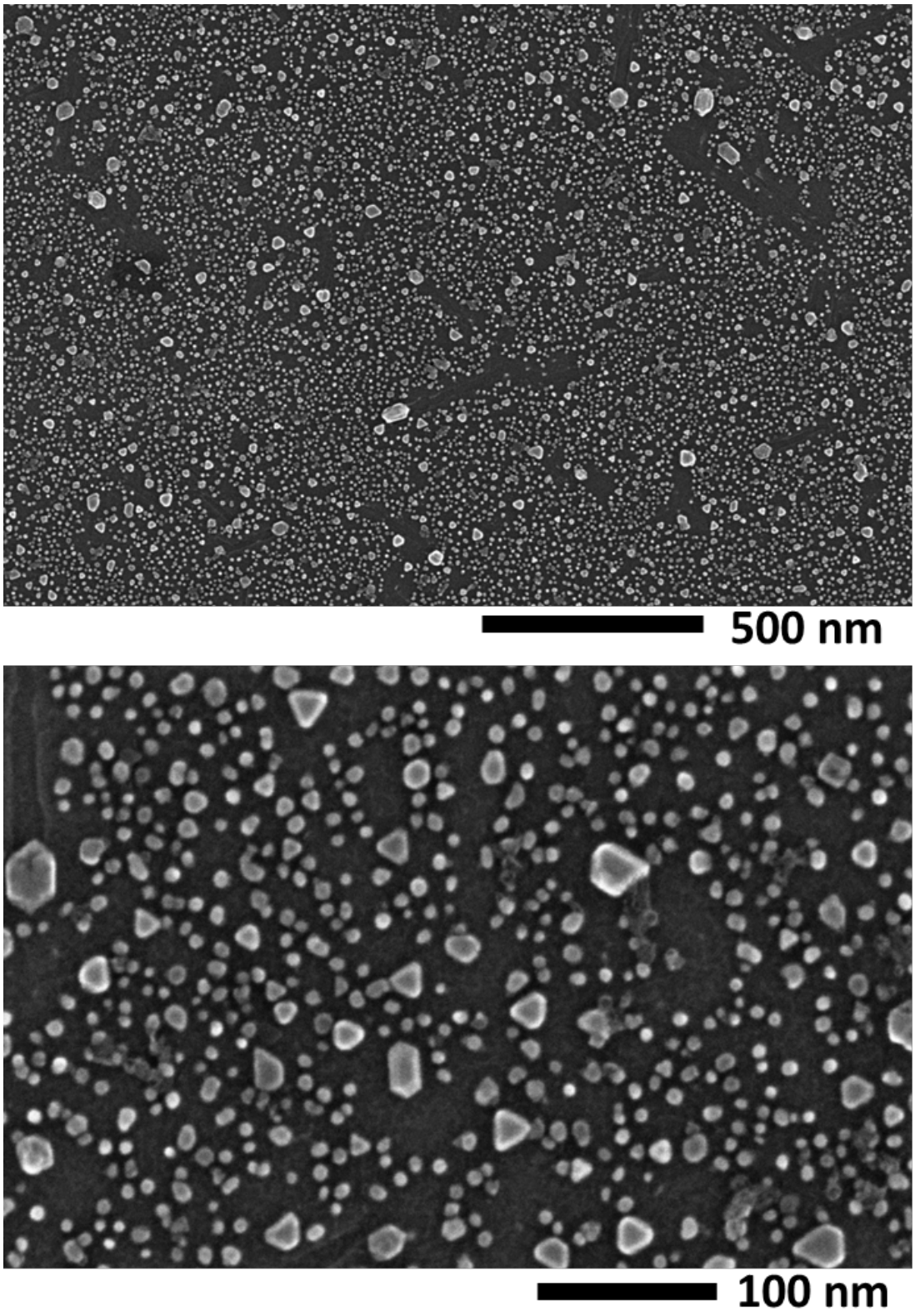

Figure 5.6. SEM images of 2 nm of Fe deposited at 600 °C on different O_2 pressure HOPG at different temperature. (top) Low-magnification SEM image of Fe deposited on HOPG that was treated with 0.4 mbar of O_2 pressure for 10 minutes.(bottom) High-magnification SEM image.

Plasma power did not affect much on a sample where Fe was deposited at 700 °C. Figure 5.7 and 5.8 represents HOPG that was plasma treated with 1 mbar and 0.4 mbar of oxygen for 10 minutes, respectively. Most of the HOPG surface was covered up with NPs that are in 10 – 20 nm in range. These NPs on both surfaces were not crystalline but in spherical shape. These results suggest that once the substrate reaches a certain temperature, the oxygen plasma power dependence on NP size is no longer affective. This is due to the fact that Fe adatoms diffuse faster at the surface that the size of the defect can no longer affect NP size. In this case, 700 °C was enough to overrule the size of defect sites.

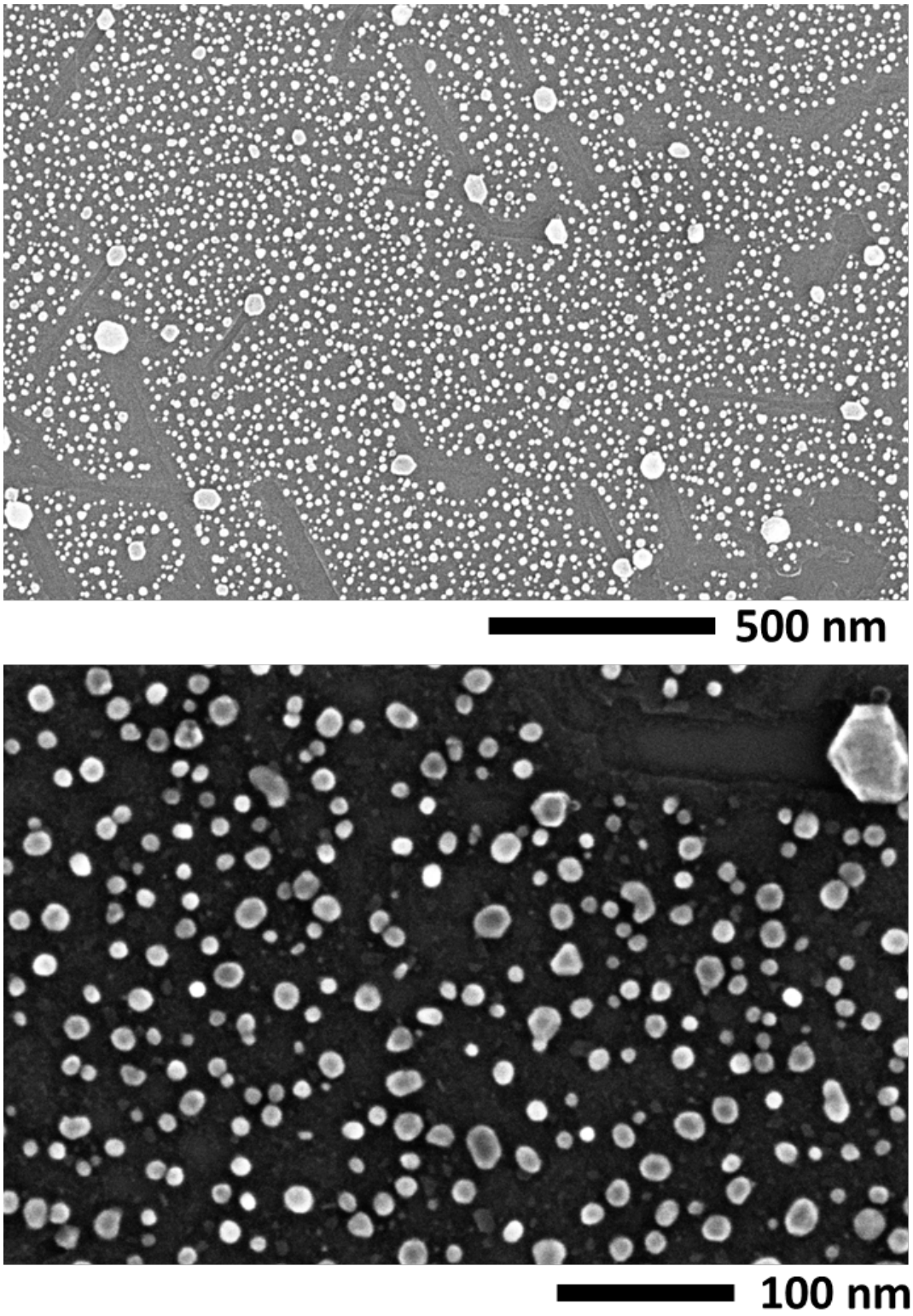

Figure 5.7. SEM images of 2 nm of Fe deposited at 700 °C on different O_2 pressure HOPG at different temperature. (top) Low-magnification SEM image of Fe deposited on HOPG that was treated with 1 mbar of O_2 pressure for 10 minutes. (bottom) High-magnification SEM image.

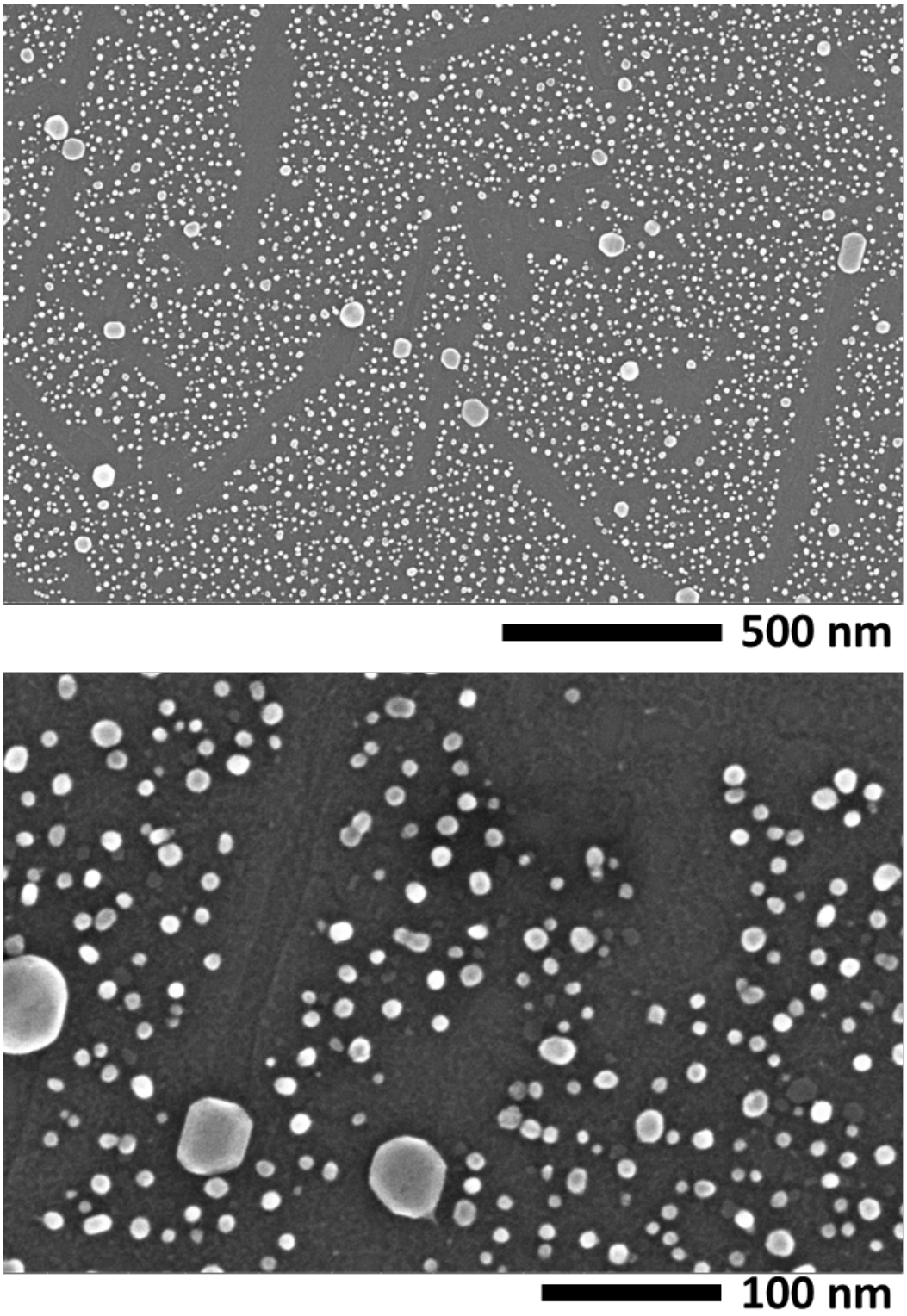

Figure 5.8. SEM images of 2 nm of Fe deposited at 700 °C on different O_2 pressure HOPG at different temperature. (top) Low-magnification SEM image of Fe deposited on HOPG that was treated with 0.4 mbar of O_2 pressure for 10 minutes. (bottom) High-magnification SEM.

5.3 Varying deposition rate

Fe NP growth on oxygen plasma treated HOPG varied with deposition rate. Figure 4.9 show SEM images of Fe deposited at 600 °C at different rates. Fe deposition at a rate of 0.266 nm/min results in particles with are more crystalline and discrete. There were two types of NPs, where the smal particles were dispersed all over the surface of HOPG whereas the large particles showed trails behind. At a relatively fast Fe deposition rate, 0.36 nm/min, a different morphology was observed. Instead of discrete NPs with similar morphology, there are at least 3 different types of morphology observed: spherical NPs, thin sheet, and needle-like long nanowires. There is no exact explanation for these effects; however, it can be assumed that at a faster rate, rate of diffusion of Fe adatoms might be slower than the rate of nucleation.

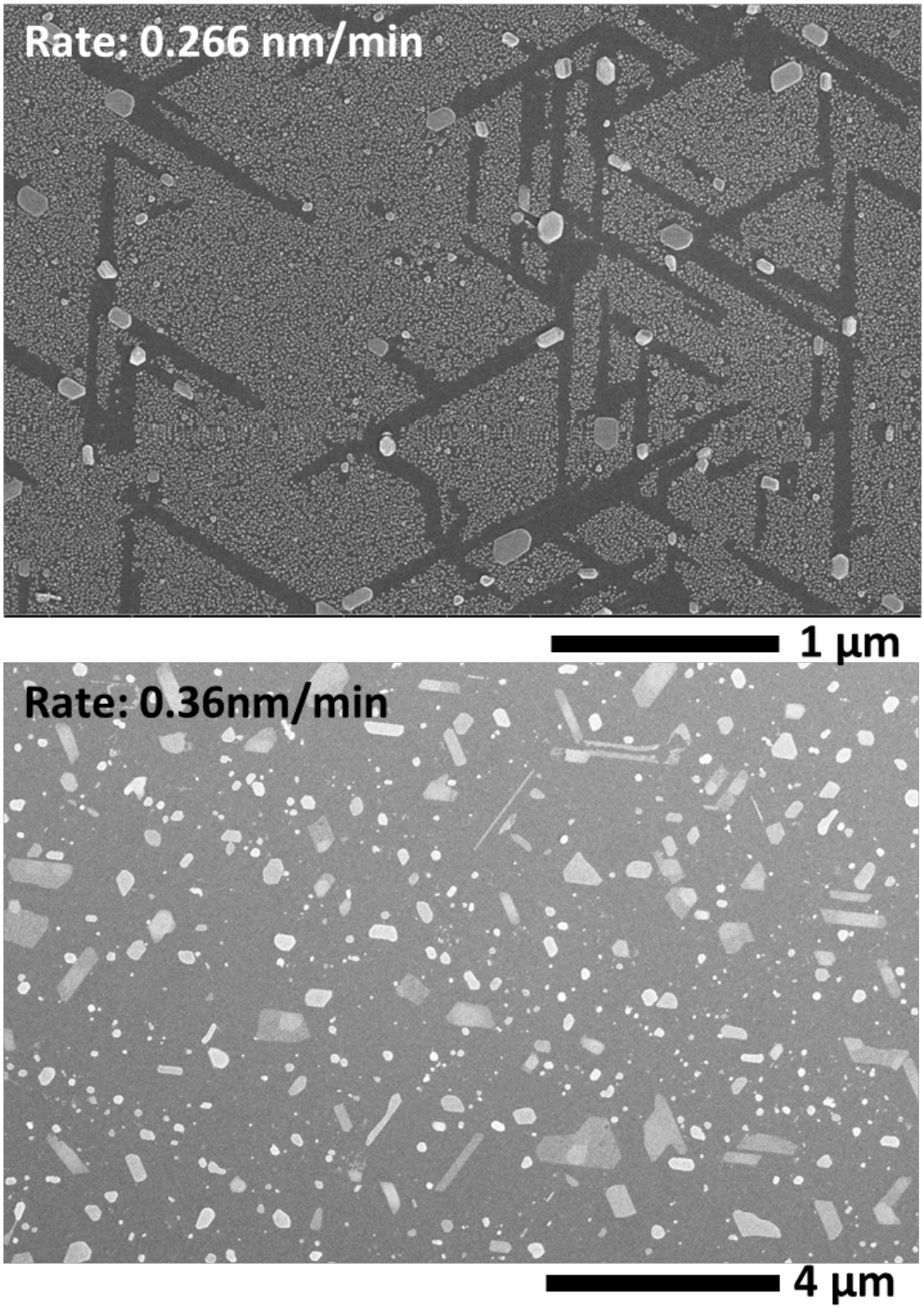

Figure 5.9. SEM images of 2nm of Fe deposited at 600 °C at different deposition rate. (top) Fe deposited at 0.226 nm/min. (bottom) Fe deposited at 0.36 nm/min.

5.4 Post-annealing effect

Post-annealing after deposition affected the morphology of Fe NPs dramatically. Figure 5.10 shows a SEM image of a sample that was post-annealed at deposition temperature for 3 hours and Figure 5.11 represents a sample where there was no post-annealing. During the annealing process, particles undergo the Oswald ripening effect. This is evidenced from the trail that is behind larger NPs. This effect was not observed on HOPG samples not treated with oxygen plasma (Chapter 1) as shown by the distance between the NPs. On an oxygen plasma treated HOPG, however, Fe NPs were very close to each other. At 600 °C annealing process, NPs that are within 1-2 nm away from each other can diffuse into each other creating larger NPs. It is evident that the 3 hours of annealing process generates the diffusion of NPs resulting in the formation of large NPs in the size range of hundreds of nm. The trails behind suggest that as the small NPs diffused into each other, it also slowly moved along the terraces (Figure 5.1-5.10). This Oswald ripening effect-dependent growth (by definition, 'big island grow at the expense of small island'[4]) is affected by post-annealing process and is different from the Volmer-Weber growth observed with linearly ordered Fe oxide arrays (shown in chapter 1).

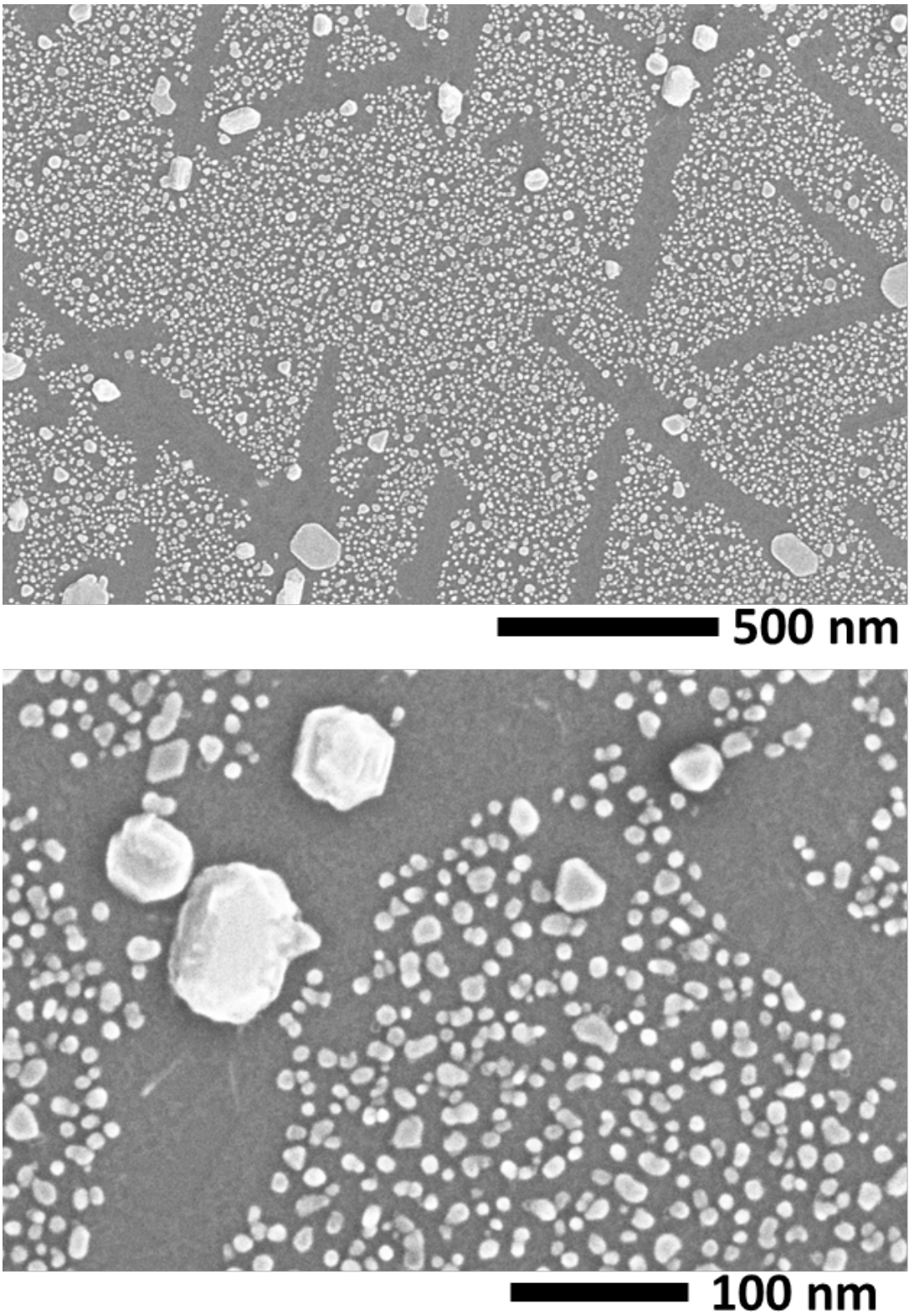

Figure 5.10. (top) Low-magnification SEM image of sample that was post-annealed at 600 °C for 3 hours. (b) High-magnification SEM image of top.

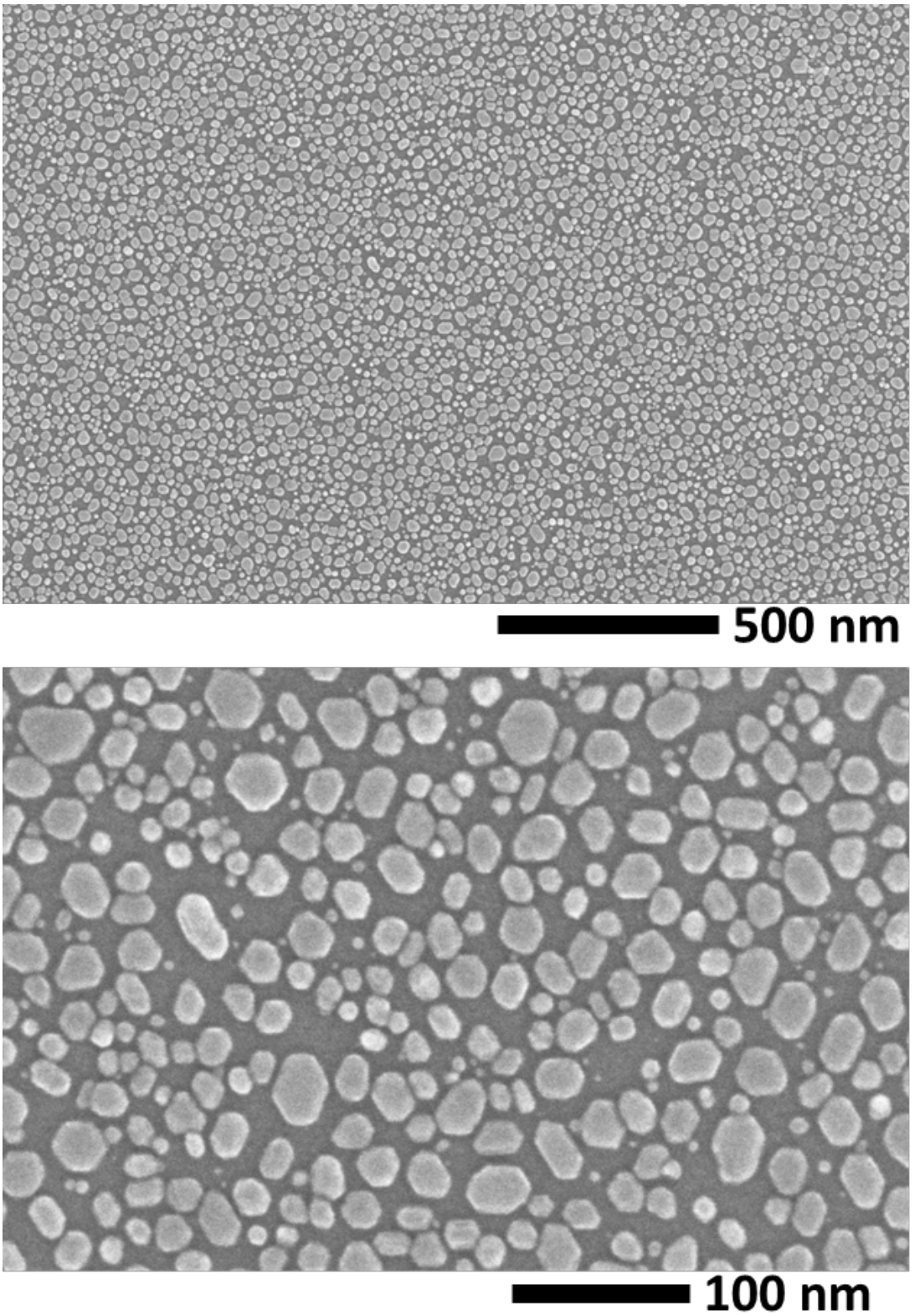

Figure 5.11. SEM images of no post-annealing processed sample. (top) Low-magnification SEM image of sample that was not annealed after Fe deposition. (bottom) High-magnification SEM image of top.

5.5 Characterization of high-density Fe nanoparticles and its comparison to linearly ordered Fe nanoparticles on step edges.

XP spectra were analyzed by using CasaXPS and XPSpeak 4.1 software. All XP spectra were calibrated by fixing C 1s peak to 284.6 eV, which represents graphite. Background subtraction was made by subtraction of Shirley-type background from each spectrum.[5] All the survey scans were collected to determine the presence of contaminates. Figure 5.12 is a Fe spectrum of Fe 2p of the high-density Fe NPs prepared on HOPG (black line). Due to spin-orbit coupling, Fe 2p peak is split into two peaks where lower and higher binding energy represents Fe $2p_{3/2}$ and Fe $2p_{1/2}$, respectively. Fe $2p_{3/2}$ peak represents four degeneracy states whereas Fe $2p_{1/2}$ represents two degeneracy states. Due to this fact, Fe $2p_{3/2}$ peak is bigger than Fe $2p_{1/2}$ peak. The peak splitting distance for Fe oxide in this case is 13.6 eV. In Figure 5.12, Fe $2p_{3/2}$ peak is located at 710.6 eV which represents Fe_2O_3.[6] There is a satellite peak located 8 eV higher than associated Fe $2p_{3/2}$ peak which is indicative of Fe_2O_3 phase. Importantly, when compared to the XP spectra of linearly ordered Fe NP arrays prepared in chapter 1, there was a significant enhancement in the detection signal. These results confirm that the oxygen plasma treatment of HOPG can enhance the detection limit due to the high particle density on the HOPG surface.

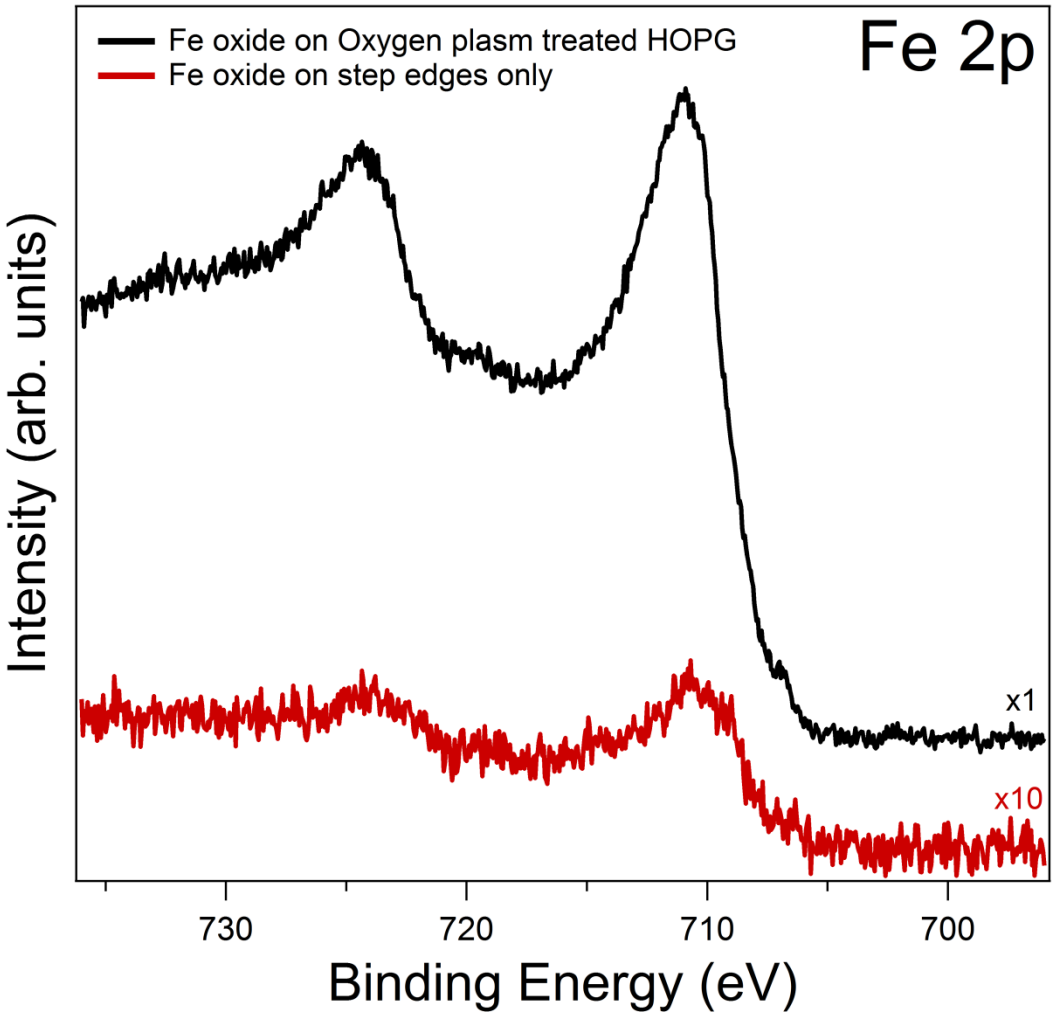

Figure 5.12. Comparison XP spectra of Fe2p. black line represents Fe oxide NPs on O_2 plasma treated HOPG and red line represents linearly ordered Fe NP arrays from chapter 1 (enlarged 10 times).

CONCLUSION

Here in this chapter, we investigated how creating defect sites by oxygen plasma treatment on HOPG affect Fe NP growth. This was an attempt to improve the detection limits for NP characterization (as shown in Figure 5.12 red line; linearly ordered Fe NP arrays without oxygen plasma treatment). By varying 4 different parameters, we find that substrate temperature upon deposition, oxygen plasma power, deposition rate, and post-annealing condition all can affect Fe NP growth on HOPG. Importantly, oxygen plasma treatment resulted in defect sites that caused high particle density growth of Fe NPs on HOPG. This resulted in an improvement of the detection intensity as shown by XPS (Figure 5.12 black line).

REFERENCES

1. Chang, H.; Bard, A. J., Scanning Tunneling Microscopy Studies of Carbon-Oxygen Reactions on Highly Oriente Pyrolytic Graphite. *J. Amer. Chem Soc.* **1991,** *113*, 5588-5596.
2. Chu, X.; Schmidt, L. D., Reaction of NO, O_2, H_2O, and CO_2 with the basal plane of graphite. *Surf. Sci.* **1992,** *268*, 325-332.
3. Paredes, J. I.; Martinez-Alonso, A.; Tascon, J. M. D., Comparative study of the air and oxygen plasma oxidation of highly oriented pyrolytic graphite: a scanning tunneling and atomic force microscopy investigation. *Carbon* **2000,** *38*, 1183-1197.
4. Pimpinelli, A.; Villain, J., *Physics of Crystal Growth*. Cambridge university press: 1998.
5. Norgren, B.; Somers, M.; de Wit, J., *Surf. Interface Anal.* **1994,** *21*, 378.
6. Yamashita, T.; Hayes, P., Analysis of XPS spectra of Fe^{2+} and Fe^{3+} ions in oxide materials. *Appl. Surf. Sci.* **2008,** *254*, 2441-2449.